Effect of local lattice strain and electron beam irradiation on electrical transport properties of graphene

Hikari Tomori

February 2014

Effect of local lattice strain and electron beam irradiation on electrical transport properties of graphene

Hikari Tomori
Doctoral Program in Physics

Submitted to the Graduate School of
Pure and Applied Sciences
in Partial Fulfillment of the Requirements
for the Degree of Doctor of Philosophy in Science

at the
University of Tsukuba

Contents

Introduction

Graphene is a two dimensional atomic layer of carbon atoms. It has a liner energy dispersion relation at low energies, which makes charge carriers of graphene behave as massless Dirac Fermions. While observation of Dirac Fermionic (relativistic) phenomena normally requires the cosmic space or a massive accelerator, graphene allows one to observe them in low-energy table-top experiments in a laboratory. Therefore, graphene has attracted much attention from the fundamental science side.

Besides, from the engineering side, due to high mobility, graphene is expected to be a promising candidate for the next generation electronic material. The biggest challenge in application of graphene to electronic devices such as high speed transistors is the formation of transport gap. Although several methods have been proposed for the transport gap formation in graphene, e.g., using graphene nanoribbons and bilayer graphene in perpendicular electric fields, these methods have lots of technological issues; In graphene nanoribbons, the edge control with atomic precision is indispensable, but technologically it is quite difficult. In bilayer graphene, suppression of the leakage current is challenging because the mobility of bilayer graphene is intrinsically smaller than that of single layer graphene.

Another method for the transport gap formation has been proposed, which avoids the issues described above. It is based on the strain effect in graphene. In this thesis, we focus on the electron transport in graphene under local strain.

According to theories of strain effect, for observation of transport gap induced by the strain effect, control of the spatial variation of strain is essential. So, we first develop a method for creating a designed local strain in graphene. Here we use resist nanostructures which are placed between a graphene film and the Si substrate. A graphene film is attached to a non-flat substrate with patterned resist nanostructures. We aim to experimentally clarify modulation of electron transport by lattice strain. Here, the amount of local lattice strain is confirmed by Raman spectroscopy, and transport properties is investigated by four-terminal measurement at room temperature.

Next, we investigate the effect of electron beam irradiation on the graphene transport properties. In the study of the strain effect, excess electron beam exposure is used for the fabrication of the resist nanostructures, which might have a great influence on the electron transport in graphene. Moreover, from the view point of the further improvement of graphene properties, quantitative evaluation of the defect density is indispensable. The Raman microscopy is commonly used for

the quantification of the defect density in graphene. In graphitic materials, the intensity ratio of D band to G band reflects the defect density. Here, we studied the relationship between the Raman $I_{\mathrm{D}}/I_{\mathrm{G}}$ ratio and the electron mean free path by combining the Raman spectroscopy with the transport measurement.

This thesis consists of five chapters. In Chapter 1, fundamental electronic and transport properties of graphene as well as the present status of researches related to ours are described. In Chapter 2, basic sample fabrication and measurement techniques are presented. Chapter 3 is devoted to experiments on the strain effect in graphene. We explain our original methods for introducing designed local strain to graphene, and describe experimental results on transport measurements and Raman spectroscopy. Chapter 4 describes the study on the effect of electron beam irradiation on graphene properties. Here we focus on the relationship between the Raman spectra and the electron mean free path. Finally, we summarize our study in Chapter 5.

Chapter 1

Theoretical and experimental background

1.1 Electronic and transport properties of graphene

Graphene consists of a single atomic layer, in which carbon atoms are arranged into a hexagonal lattice. A carbon atom has four valence electrons. By using three of them, carbon atoms are bound forming sp^2-hybrid orbitals in the plane. The fourth electron which occupies the p_z-orbital takes a role as a carrier in electron transport. In the following, the electronic structure of graphene is considered based on the nearest neighbor tight binding approximation.

1.1.1 Liner dispersion relation in graphene

A unit cell of graphene includes two carbon atoms, each of which belongs to A- or B- sublattice, as shown in Fig 1.1(a). The real space unit vectors are given by

$$\overrightarrow{\mathrm{a_1}} = \frac{a}{2}\left(\sqrt{3}, 1\right), \quad \overrightarrow{\mathrm{a_2}} = \frac{a}{2}\left(\sqrt{3}, -1\right),$$

where $a = 2.46$ Å is the lattice constant. The nearest-neighbor vectors are

$$\overrightarrow{\mathrm{R_1}} = a\left(\frac{1}{2\sqrt{3}}, \frac{1}{2}\right), \quad \overrightarrow{\mathrm{R_2}} = a\left(\frac{1}{2\sqrt{3}}, -\frac{1}{2}\right), \quad \overrightarrow{\mathrm{R_3}} = a\left(-\frac{1}{\sqrt{3}}, 0\right).$$

The corresponding reciprocal lattice vectors are given by

$$\overrightarrow{\mathrm{b_1}} = \frac{2\pi}{a}\left(\frac{1}{\sqrt{3}}, 1\right), \quad \overrightarrow{\mathrm{b_2}} = \frac{2\pi}{a}\left(\frac{1}{\sqrt{3}}, -1\right).$$

Figure 1.1(b) shows the Brillouin zone of single layer graphene (hexagon), in which Γ , K (K'), and M are the center, the corner and the center of the edge of the brillouin zone, respectively.

Two Bloch functions are generated for A- and B- sublattice and are given by

$$\Phi_{\mathrm{A}}(\boldsymbol{r}) = \frac{1}{\sqrt{M}} \sum_{\boldsymbol{R}_{\mathrm{A}}} e^{i\boldsymbol{k}\boldsymbol{R}_{\mathrm{A}}} \varphi(\boldsymbol{r} - \boldsymbol{R}_{\mathrm{A}}),$$

$$\Phi_{\mathrm{B}}(\boldsymbol{r}) = \frac{1}{\sqrt{M}} \sum_{\boldsymbol{R}_{\mathrm{B}}} e^{i\boldsymbol{k}\boldsymbol{R}_{\mathrm{B}}} \varphi(\boldsymbol{r} - \boldsymbol{R}_{\mathrm{B}}),$$

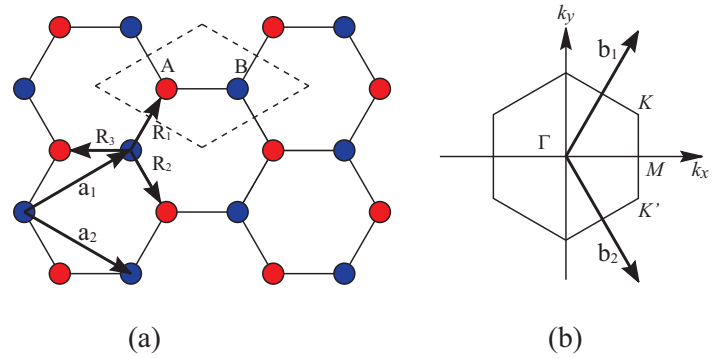

Figure 1.1: (a) Graphene's honeycomb lattice. It is made out of two triangular sub-lattices. A unit cell, indicated by broken lines, has two carbon atoms, each of which belongs to the A- or B-sublattice. a_1 and a_2 are unit vectores. R_i ($i = 1, 2, 3$) is a nearest neighbor vector. (b) Solid hexagon indicates the first Brillouin zone. b_1 and b_2 are reciprocal lattice vectors. Γ, K (K'), and M are the center, the corner and the center of the edge of the Brillouin zone, respectively.

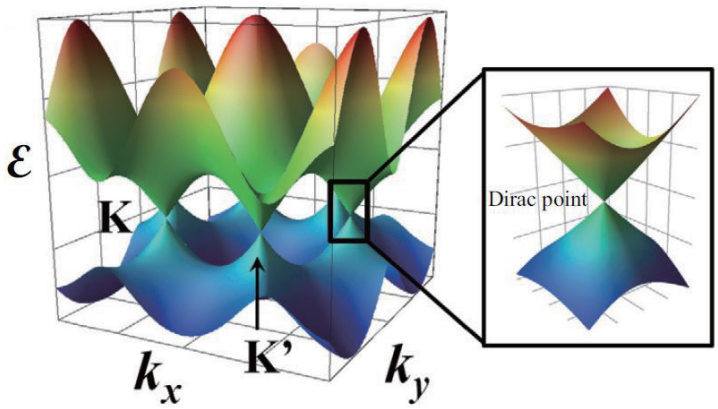

Figure 1.2: Energy dispersion relation of graphene. At the K and K' points, liner dispersion relation appears. After Ref. [1].

where φ is a wave function for an isolated carbon atom and M is the number of unit cells in the crystal. The wave function for the whole crystal is taken to be a linear combination of the above Bloch functions

$$\Psi(\boldsymbol{R}) = \lambda_1 \Phi_{\mathrm{A}}(\boldsymbol{r}) + \lambda_2 \Phi_{\mathrm{B}}(\boldsymbol{r}),$$

where λ_1 and λ_2 are constants of the liner combination. The eigenvalue of the Schrödinger equation

$$H\Psi = E\Psi,$$

is given by

$$E = \frac{< \Psi|H|\Psi >}{< \Psi|\Psi >}.$$

The minimum energy satisfies the following equations,

$$\frac{\partial E}{\partial \lambda_1^*} = \frac{\partial E}{\partial \lambda_2^*} = 0.$$

Thus, λ_1^* and λ_2^* satisfy the following equations,

$$\lambda_1(< \Phi_{\rm A}|H|\Phi_{\rm A} > -E < \Phi_{\rm A}|\Phi_{\rm A} >) + \lambda_2(< \Phi_{\rm A}|H|\Phi_{\rm B} > -E < \Phi_{\rm A}|\Phi_{\rm B} >) = 0, \tag{1.1}$$

$$\lambda_1(< \Phi_{\rm B}|H|\Phi_{\rm A} > -E < \Phi_{\rm B}|\Phi_{\rm A} >) + \lambda_2(< \Phi_{\rm B}|H|\Phi_{\rm B} > -E < \Phi_{\rm B}|\Phi_{\rm B} >) = 0, \tag{1.2}$$

Here we take the nearest neighbor approximations:

$$\begin{aligned}
< \Phi_{\rm A}|H|\Phi_{\rm A} >=< \Phi_{\rm B}|H|\Phi_{\rm B} > &\approx \frac{1}{M}\sum_{\boldsymbol{R}_{\rm A}=\boldsymbol{R}_{\rm A'}} e^{i\boldsymbol{k}(\boldsymbol{R}_{\rm A}-\boldsymbol{R}_{\rm A'})} < \varphi(\boldsymbol{r}-\boldsymbol{R}_{\rm A'})|H|\varphi(\boldsymbol{r}-\boldsymbol{R}_{\rm A}) > \\
&= \frac{1}{M}M\epsilon \\
&= \epsilon, \\
< \Phi_{\rm A}|\Phi_{\rm A} >=< \Phi_{\rm B}|\Phi_{\rm B} > &\approx \frac{1}{M}\sum_{\boldsymbol{R}_{\rm A},\boldsymbol{R}_{\rm A'}} e^{i\boldsymbol{k}(\boldsymbol{R}_{\rm A}-\boldsymbol{R}_{\rm A'})} < \varphi(\boldsymbol{r}-\boldsymbol{R}_{\rm A'})|\varphi(\boldsymbol{r}-\boldsymbol{R}_{\rm A}) > \\
&= \frac{1}{M}M = 1.
\end{aligned}$$

where $\epsilon =< \varphi(\boldsymbol{r}-\boldsymbol{R}_{\rm A'})|H|\varphi(\boldsymbol{r}-\boldsymbol{R}_{\rm A}) >$, and we focus on a term only for $\boldsymbol{R}_{\rm A} = \boldsymbol{R}_{\rm A'}$, because it makes the largest contribution to the sum. We approximate the overlap integrals and the transfer integrals by considering only the contributions of the nearest neighbor atoms:

$$\begin{aligned}
< \Phi_{\rm A}|H|\Phi_{\rm B} >=< \Phi_{\rm B}|H|\Phi_{\rm A} >^* &= \frac{1}{M}\sum_{\boldsymbol{R}_{\rm A},\boldsymbol{R}_{\rm B}} e^{i\boldsymbol{k}(\boldsymbol{R}_{\rm B}-\boldsymbol{R}_{\rm A})} < \varphi(\boldsymbol{r}-\boldsymbol{R}_{\rm A})|H|\varphi(\boldsymbol{r}-\boldsymbol{R}_{\rm B}) > \\
&\approx \frac{1}{M}M(e^{i\boldsymbol{k}\boldsymbol{R}_1}+e^{i\boldsymbol{k}\boldsymbol{R}_2}+e^{i\boldsymbol{k}\boldsymbol{R}_3}) < \varphi(\boldsymbol{r}-(\boldsymbol{R}_{\rm B}+\boldsymbol{R}_1))|H|\varphi(\boldsymbol{r}-\boldsymbol{R}_{\rm B}) > \\
&= f(k)t, \\
< \Phi_{\rm A}|\Phi_{\rm B} >=< \Phi_{\rm B}|\Phi_{\rm A} >^* &= \frac{1}{M}\sum_{\boldsymbol{R}_{\rm A},\boldsymbol{R}_{\rm B}} e^{i\boldsymbol{k}(\boldsymbol{R}_{\rm B}-\boldsymbol{R}_{\rm A})} < \varphi(\boldsymbol{r}-\boldsymbol{R}_{\rm A})|\varphi(\boldsymbol{r}-\boldsymbol{R}_{\rm B}) > \\
&\approx \frac{1}{M}M(e^{i\boldsymbol{k}\boldsymbol{R}_1}+e^{i\boldsymbol{k}\boldsymbol{R}_2}+e^{i\boldsymbol{k}\boldsymbol{R}_3}) < \varphi(\boldsymbol{r}-(\boldsymbol{R}_{\rm B}+\boldsymbol{R}_1))|\varphi(\boldsymbol{r}-\boldsymbol{R}_{\rm B}) > \\
&= f(\boldsymbol{k})s,
\end{aligned}$$

where

$$\begin{aligned}
f(k) &= e^{i\boldsymbol{k}\boldsymbol{R}_1}+e^{i\boldsymbol{k}\boldsymbol{R}_2}+e^{i\boldsymbol{k}\boldsymbol{R}_3}, \\
&= 2e^{ik_{\rm x}a/2\sqrt{3}}\cos\left(\frac{k_{\rm y}a}{2}\right)+e^{-ik_{\rm x}a/\sqrt{3}}, \\
t &= < \varphi(\boldsymbol{r}-(\boldsymbol{R}_{\rm B}+\boldsymbol{R}_1))|H|\varphi(\boldsymbol{r}-\boldsymbol{R}_{\rm B}) >= t^*, \\
s &= < \varphi(\boldsymbol{r}-(\boldsymbol{R}_{\rm B}+\boldsymbol{R}_1))|\varphi(\boldsymbol{r}-\boldsymbol{R}_{\rm B}) >= s^*.
\end{aligned}$$

Substituting these approximations in equations (1.1) and (1.2), we get

$$\begin{pmatrix} \epsilon - E & (t - Es)f(\boldsymbol{k}) \\ (t - Es)f(\boldsymbol{k})^* & \epsilon - E \end{pmatrix} \begin{pmatrix} \lambda_1 \\ \lambda_2 \end{pmatrix} = 0,$$

When λ_1^* and λ_2^* have non-trivial solutions without zero, the following equation is satisfied:

$$\begin{vmatrix} \epsilon - E & (t - Es)f(\boldsymbol{k}) \\ (t - Es)f(\boldsymbol{k})^* & \epsilon - E \end{vmatrix} = 0,$$

By solving for E, one obtains the following dispersion relation,

$$E = \frac{\epsilon \pm tw}{1 \pm sw},$$

where

$$w = \sqrt{|f(\boldsymbol{k})^2|} = \sqrt{1 + 4\cos^2(k_y \frac{a}{2}) + 4\cos(k_y \frac{a}{2})\cos(k_x \frac{\sqrt{3}a}{2})}.$$

For low energies, the dispersion relation around K and K' points becomes linear, as shown in Fig. 1.2. At the K and K' points, the top of the conical valence band is connected to the top of the conical conduction band. Thus, graphene is zero-gap semiconductor (zero-overlap semimetal). The connecting point is called the *Dirac point*, where the Fermi energy of non-doped graphene is situated. For this reason, the carriers (conduction electrons and holes) in single layer graphene behave as massless Dirac fermions, obeying the relativistic Dirac equation.

1.1.2 Gate voltage dependence of transport properties

Due to the conical linear dispersion relation near the Dirac point $\epsilon = \hbar v_F k$, the density of states of graphene is proportional to the energy ϵ: $D(\epsilon) = \frac{2\epsilon}{\pi(\hbar v_F)^2}$. Thus, graphene's transport properties are strongly affected by the change of the Fermi level. Besides, due to the massless feature of carriers, carrier mobility is much higher than that of Si. For these reasons, graphene is a promising candidate for a next-generation electronic material.

For controlling the Fermi level, the field-effect-transistor (FET) structure with back gate (Fig. 1.3(a)) is commonly used, in which a graphene film is placed on a highly-doped Si substrate covered with an insulating layer SiO_2 and is connected with electrodes. The highly-doped Si substrate is used as the back gate, which allows one to control the carrier density and the position of the Fermi level, as shown in Fig. 1.3(b).

Figure 1.4 shows an example of the gate voltage dependence of transport properties in a graphene FET device placed on an SiO_2/Si substrate. The conductivity (σ) curve exhibits a V-shaped characteristic with a minimum corresponding to the Fermi energy situated at the Dirac point (Fig. 1.4(a)). This is the common feature of graphene FET devices placed on a SiO_2/Si substrate.

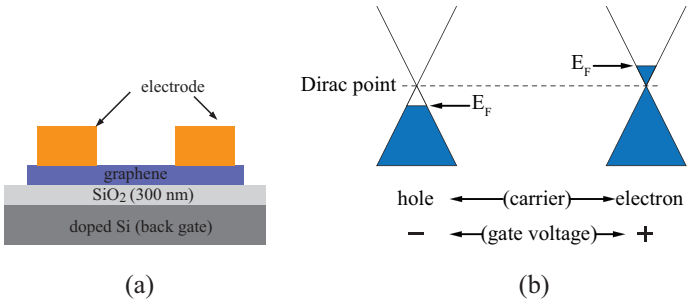

Figure 1.3: (a) Side view of a typical graphene FET device. Graphene film is placed on a highly doped Si substrate covered with an SiO_2 layer. Doped Si is used as a back gate. (b) Fermi level in graphene is controlled by the gate voltage.

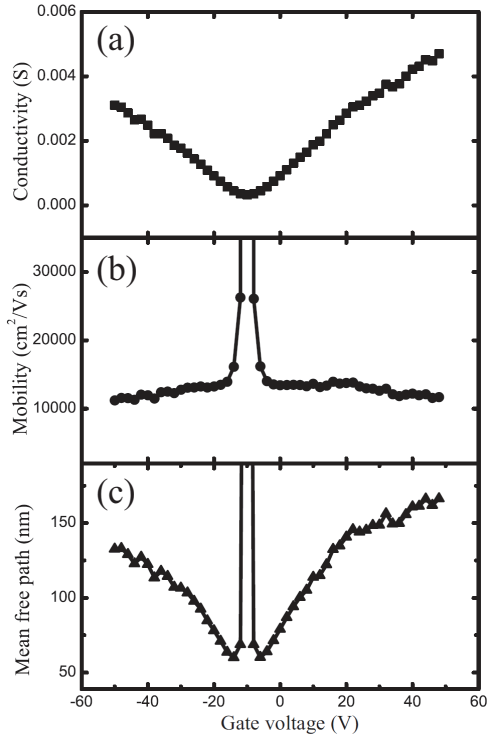

Figure 1.4: (a) Gate voltage dependence of conductivity of a graphene FET device placed on a SiO_2/Si substrate. Conductivity curve shows a V-shaped characteristic with a minimum corresponding to the Dirac point. The carrier mobility (b) and the mean free path (c) are also shown as a function of the gate voltage. After Ref. [1].

From the gate voltage dependence of conductivity, one can obtain the carrier field-effect mobility $\mu_{\rm FE}$ and the carrier mean free path l by using these formulas[1]

$$\mu_{\rm FE} = \frac{1}{e}\frac{d\sigma}{dn} = \frac{1}{c_{\rm g}}\frac{d\sigma}{dV_{\rm g}},$$

$$l = \frac{h}{2e^2}\frac{\sigma}{\sqrt{n\pi}}.$$

Here, n is the carrier density and $c_{\rm g} = \epsilon\epsilon_0/d$ is the gate capacitance per unit area. ϵ_0 and $\epsilon \approx 4$ are the dielectric constant of the free space and the relative dielectric constant of SiO_2, respectively, and d is the thickness of the SiO_2 layer. For a gate voltage ($V_{\rm g}$) which is far from the gate voltage corresponding to the Dirac point, $V_{\rm D}$[1], the carrier density is given by

$$n = \frac{c_{\rm g}|V_{\rm g} - V_{\rm D}|}{e} = \alpha|V_{\rm g} - V_{\rm D}|.$$

For an SiO_2 layer with $d = 300$ nm, α is $7.2 \times 10^{14}/{\rm m^2V}$.

The mobility and mean free path calculated from the above expressions are shown in Figs. 1.4(b) and (c), respectively. The mobility sometimes reaches $10,000$ ${\rm cm^2/Vs}$ even in a device without special treatment, which is larger than the typical mobility of silicon ($\sim 10^3$ ${\rm cm^2/Vs}$). It is noted that near the Dirac point, due to the charged impurities attached to the graphene surface, the value of the carrier density deviates from the above expression, so that the values of the mobility and mean free path near the Dirac point in Fig. 1.4 (inclusive of the diverging behavior) are not accurate.

1.1.3 Discrepancies between theories and experiments on transport properties

At the early stage of the graphene research, several discrepancies were pointed out between theoretical predictions and experimental observations of electron transport. One of them is the conductivity at the Dirac point. As shown in Fig. 1.4, even when the gate voltage is at the Dirac point which corresponds to zero carrier density, the conductivity does not vanish. A. K. Geim's group at the University of Manchester [2] reported that their samples exhibited the same minimum conductivity $\sigma_{\rm min} \sim 4e^2/h \approx 1.6 \times 10^{-4}$ S ($\approx (6.4\ {\rm k\Omega})^{-1}$), while P. Kim's group at Columbia University reported the minimum conductivity $2 - 12e^2/h$.[3] On the other hand, many theories predicted that the minimum conductivity takes a universal value $4e^2/\pi h$.[4, 5, 6] Most of this kind of discrepancies between theories and experiments have been attributed to an influence of potential fluctuations due to charged impurities.

Martin *et al.* pointed out the existence of nonuniform charge distribution (electron and hole puddles) in single layer graphene placed on SiO_2.[7] Figure 1.5 shows a color map of the spatial

[1]The gate voltage corresponding to the Dirac point, $V_{\rm D}$, is often called simply the Dirac point or the charge neutrality point.

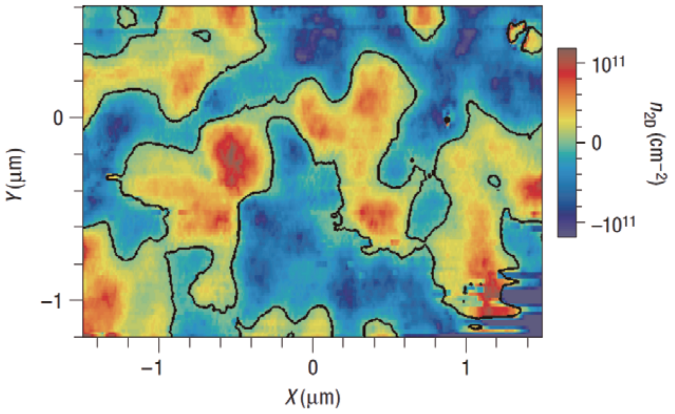

Figure 1.5: Color map of the spatial density variations in a graphene film. After Ref. [7].

variation of the carrier density in graphene on SiO_2 at the charge neutrality point, obtained by scanning single electron transistor (SET) spectroscopy. Although the average carrier density is tuned to zero, electron and hole puddles (blue and red regions, respectively) are clearly seen, indicating that one cannot reach the Dirac point with zero carrier density in experiments. Later, a scanning tunneling microscopy (STM) study revealed that the spatial charge inhomogeneity (and the resulting formation of electron and hole puddles around the charge neutrality point) is caused by charged impurities on the graphene film, indicating that in experiments, charged impurities exert great influence on electronic and transport properties of graphene near the charge neutrality point.

Adam *et al.*[8] examined theoretically the influence of a long-range scattering from charged impurities on transport properties of graphene. Their theory successfully explained the V-shaped $\sigma - V_g$ curve and the value of the minimum conductivity in graphene placed on a SiO_2/Si substrate. In their theory, the conductivity of graphene dominated by long-range scattering due to charged impurities is given by

$$\sigma(n-\bar{n}) = \begin{cases} C\dfrac{e^2}{h}\dfrac{n*}{n_{\rm imp}} & \text{for} \quad |n-\bar{n}| < n^* \\ C\dfrac{e^2}{h}\dfrac{n-\bar{n}}{n_{\rm imp}} & \text{for} \quad |n-\bar{n}| > n^* \end{cases}, \tag{1.3}$$

where n^* is the residual carrier density, which can be determined experimentally from the width of the residual conductivity plateau, as shown in Fig. 1.6 (a), $\bar{n} = \alpha V_{\rm D}$ is an offset carrier density, and $n_{\rm imp}$ is the density of charged impurities. The constant C depends on the substrate material and is given by

$$C = \frac{2}{G[2r_s]},$$

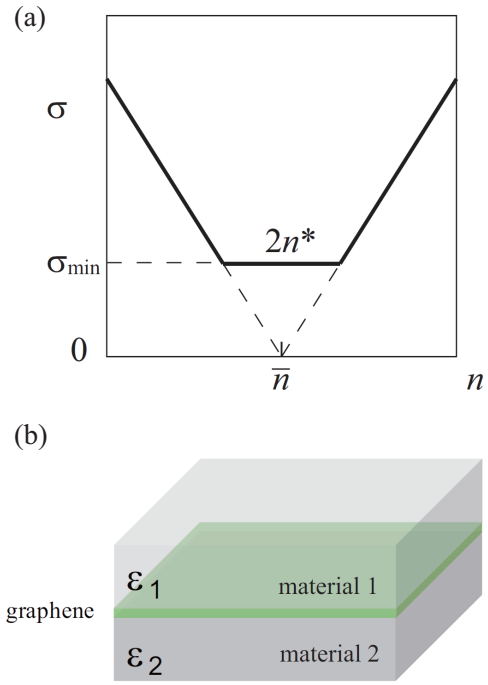

Figure 1.6: (a) Gate voltage dependence of conductivity taking into account the influence of long-range scattering from charged impurities. (b) A graphene film is sandwiched between two dielectric slabs (materials 1 and 2) with dielectric constant ϵ_1 and ϵ_2. After Ref. [1].

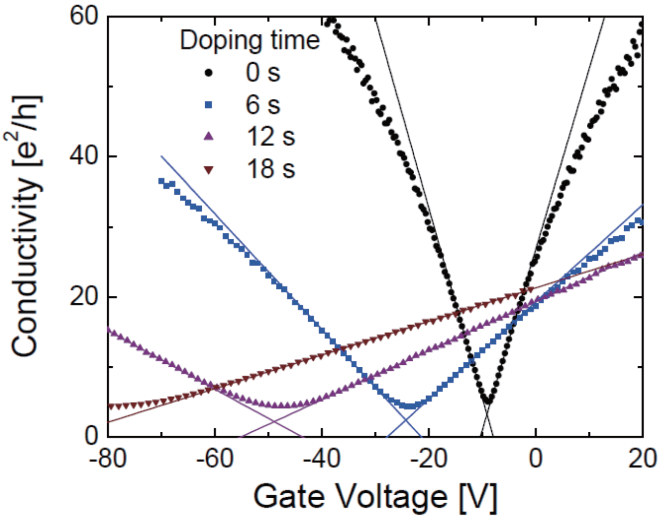

Figure 1.7: The conductivity as a function of gate voltage for the pristine sample and three different doping concentrations, taken at 20 K in ultra high vacuum. The addition of charged impurities by potassium doping produces a more liner $\sigma(V_{\rm g})$, and reduces the mobility. After Ref. [9].

where

$$G[x] = x^2\left(\frac{\pi}{4} + 3x - \frac{3\pi x^2}{2} + \frac{x(3x^2-2)\arccos[1/x]}{\sqrt{x^2-1}}\right),$$

and $r_{\rm s}$ is the dimensionless coupling constant of graphene sandwiched between two dielectric slabs (Fig. 1.6(b)). By using the dielectric constant ϵ_1 and ϵ_2, $r_{\rm s}$ can be written as

$$r_s = \frac{1}{4\pi\epsilon_0}\frac{e^2}{\hbar v_F}\frac{2}{\epsilon_1+\epsilon_2},$$

where $v_F = 1.1\times10^6$ m/s it the Fermi velocity. For graphene placed on an SiO_2 substrate, $\epsilon_1 = 1$ and $\epsilon_2 \approx 4$, giving $C \approx 20$.

From Eq.(1.3), the minimum conductivity is given by

$$\sigma_{\rm min} = C\frac{e^2}{h}\frac{n^*}{n_{\rm imp}},$$

and the mobility has the form

$$\mu = C\frac{e}{h}\frac{1}{n_{\rm imp}}. \tag{1.4}$$

The effect of charged impurities on transport properties of graphene was clearly demonstrated by Chen *et al.*[9] They deposited potassium atoms on a single graphene sample placed in a vacuum chamber, and measured the transport properties in situ with different potassium concentrations. The potassium atoms donate negative charge to graphene and work as positively charged impurities. Figure 1.7 shows the experimental result obtained by Chen *et al.*, in which the conductivity is

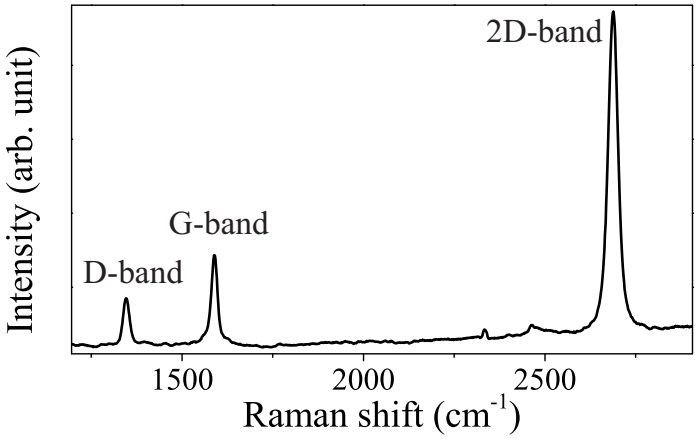

Figure 1.8: Raman spectrum of single layer graphene. Raman D band, G band and 2D band are placed at ~ 1350 cm^{-1}, ~ 1580 cm^{-1} and ~ 2680 cm^{-1}, respectively.

plotted as a function of the gate voltage for four different doping concentrations, taken at 20 K in ultra high vacuum. The doping concentration increased with doping time. The addition of charged impurities produces a more liner $\sigma(V_{\rm g})$, and reduces the mobility, with the constant $\mu n_{\rm imp} = 5\times10^{15}$ /Vs, in excellent agreement with Eq. (1.2).

1.2 Raman spectroscopy of graphene

Raman spectroscopy is a widely used method for investigating physical and chemical properties of materials, including graphene. In graphene researches, Raman spectroscopy is an important tool because it gives information about the number of graphene layers, defects, lattice strain and so on in a nondestructive way.

Typical Raman spectrum of single layer graphene is shown in Fig. 1.8. The horizontal axis is the difference of wavenumber between the incident and scattered lights, called the Raman shift. Three characteristic peaks are seen in graphitic materials, called D band (~ 1350 cm^{-1}), G band (~ 1580 cm^{-1}) and 2D band (~ 2680 cm^{-1}).

- Raman D band is situated at ~ 1350 cm^{-1}. This is a double resonance process as depicted in Fig. 1.9(a), which involves one phonon scattering and an elastic scattering by a defect. The latter arises from various symmetry-breaking defects, such as vacancies, substitutional impurities, interstitial impurities, chemical impurities, grain boundaries.

- Raman G band is situated at ~ 1580 cm^{-1}, which is present for all sp^2 carbon systems. It is due to the LO and TO modes of graphite honeycomb vibration, which degenerate at the center of the Brillouin zone (Fig. 1.9(b)).

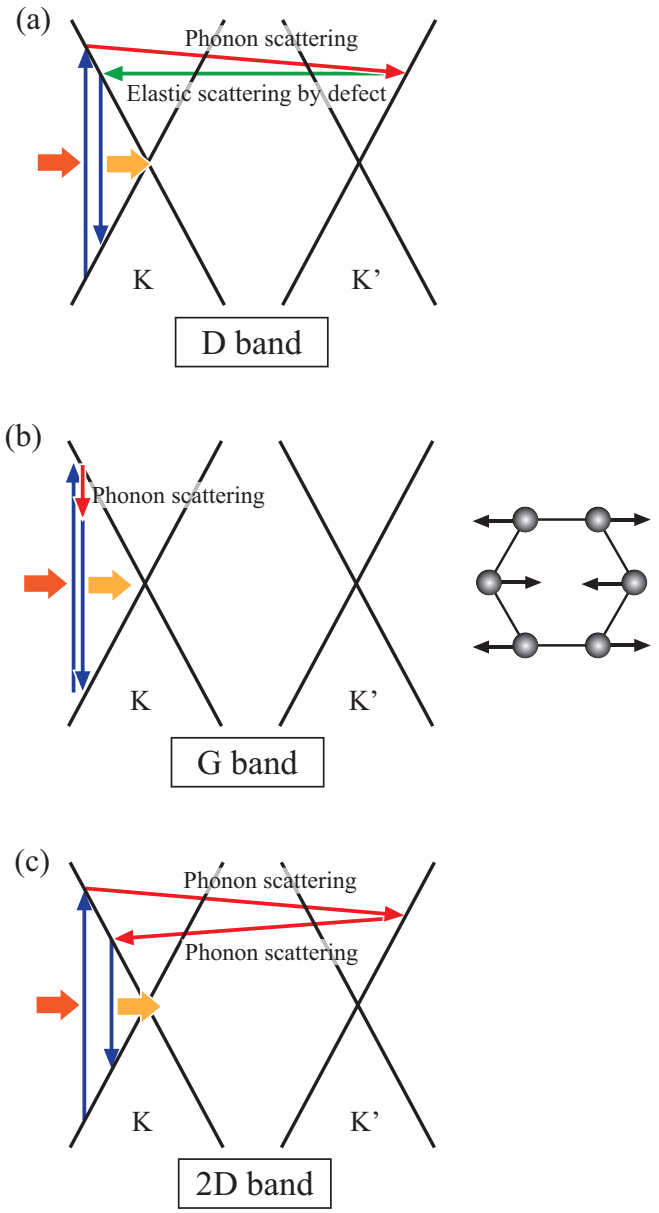

Figure 1.9: (a) Raman D band process involves one phonon scattering and an elastic scattering by a defect. (b) The G band corresponds to an in-plane vibration mode. (c) The 2D band originates from a double resonance process with two phonon scattering.

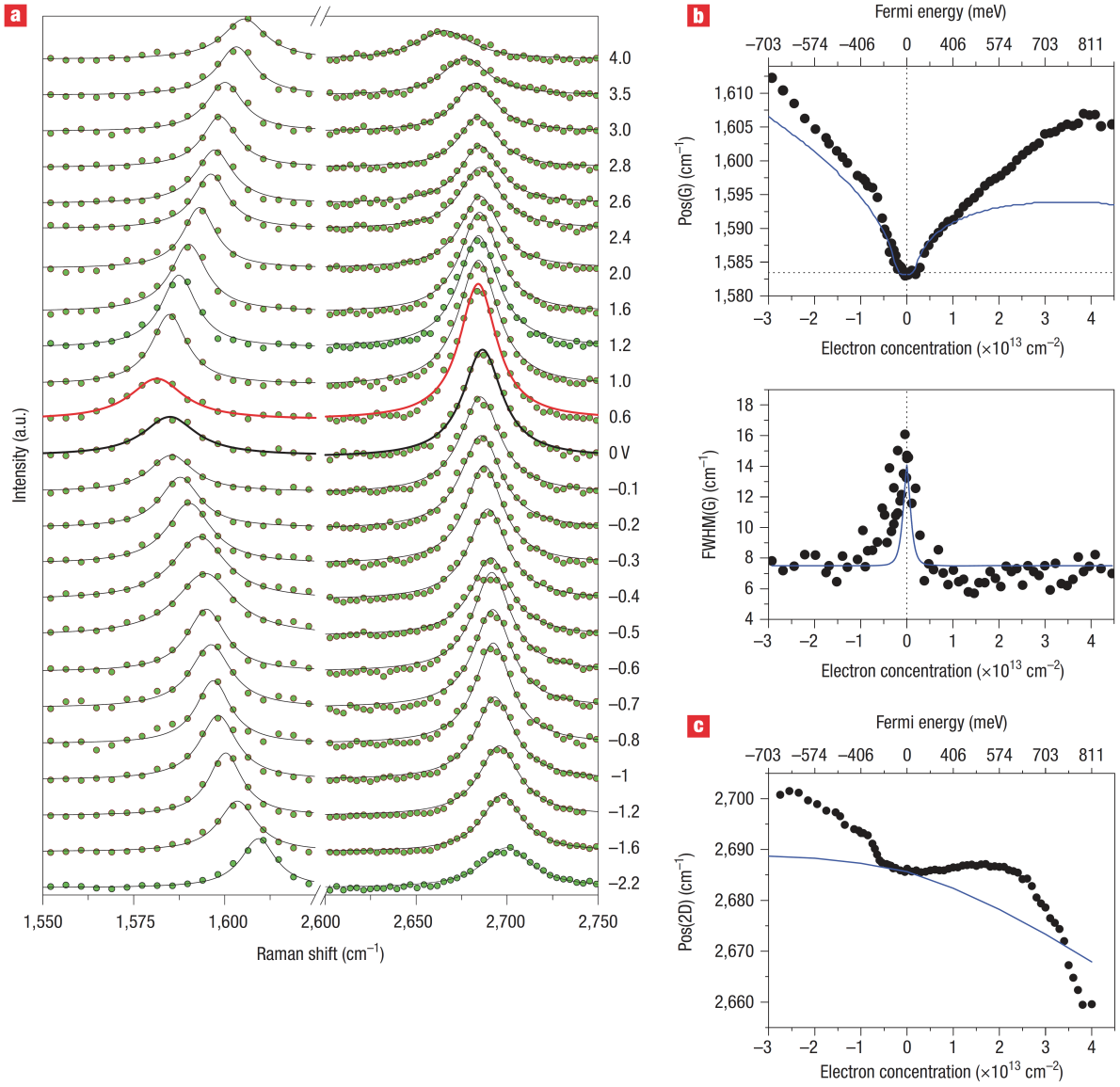

Figure 1.10: (a) Raman spectra of a graphene FET device for top gate voltages ranging between −2.2 V and 4.4 V (b) Position of the G peak (top panel) and its full width at half maximum (FWHM) (bottom panel) as a function of electron concentration. (c) 2D band position as a function of the electron concentration. After Ref. [10].

- Raman 2D band is situated at ~ 2680 cm^{-1}. It originates from a double resonance process with two phonon scattering (Fig. 1.9(c)).

1.2.1 Gate voltage dependence of Raman peak positions

Since the Raman scattering involves excitation of an electron-hole pair by the incident light, the Raman shift depends on the density of states and the Fermi level of the material. Das *et al.* observed

the modulation of Raman peaks by the carrier concentration.[10] Figure 1.10 shows Raman spectra of graphene as a function of top-gate voltage. For low concentration of carriers ($|n| < 10^{13}$ cm^{-2}), the position of Raman G band strongly depends on the carrier density (Fig. 1.10(b)), while that of Raman 2D band exhibits smaller change (Fig. 1.10(c)). We note that the carrier density of $|n| < 10^{13}$ cm^{-2} corresponds to $|V_g| < 100$ V for back-gated graphene with conventional 300 nm-SiO_2 gate insulator .

1.2.2 Strain dependence of Raman peak positions

Raman G and 2D bands are sensitive to strain in graphene lattice. For tension, both the G and 2D bands downshift. Besides, Raman G band splits into two components G+ and G− with increasing tension.

For example, Mohiuddin *et al.* applied uniaxial strain to graphene by placing a graphene film on a flexible substrate (Fig. 1.11(a)).[5] The downshift of the G and 2D peak positions as well as the splitting of the G band were clearly observed, as shown in Fig. 1.11(b). The ratios of peak downshift for Raman G+, G−, and 2D bands are ~ -10.8 cm^{-1}/%, ~ -31.7cm^{-1}/%, ~ -64cm^{-1}/%, respectively, as shown in Fig. 1.11(c). It is noted that ratios obtained by different authors can differ by a factor of 2 or more.[12] Since the 2D band position is relatively insensitive to the gate voltage for low carrier concentrations as described in the previous section, we use the 2D band for the estimation of the amount of strain.

1.2.3 Dependence of Raman spectra on the number of graphene layers

Raman spectroscopy is a widely-used and reliable method for the determination of the number of graphene layers, m. The followings are convenient ways to identify single layer graphene:

(1) The 2D peak is higher than the G peak for $m = 1$, while this is not the case for $m \geq 2$.

(2) The 2D peak of single layer graphene is fitted to a single Lorentzian, whereas thicker graphene with $m \geq 2$ has a much broader 2D band because of the splitting of electronic bands (Fig. 1.12). Thus, at high resolutions, the 2D band of $m \geq 2$ graphene splits into different subpeaks. The typical full-width at half maximum of the 2D band for single-layer graphene is ~ 30 cm^{-1}, while that for $m \geq 2$ graphene is ~ 60 cm^{-1}.

1.2.4 Effect of disorder on Raman spectra

Due to high mobility and atomic thickness, graphene is a promising candidate for the next-generation electronics material. Considerable effort has been devoted to industrial production of graphene with higher mobility, i.e., with less defect density. The defect density is commonly evaluated by Raman spectroscopy. It is known that the the intensity ratio of Raman D band

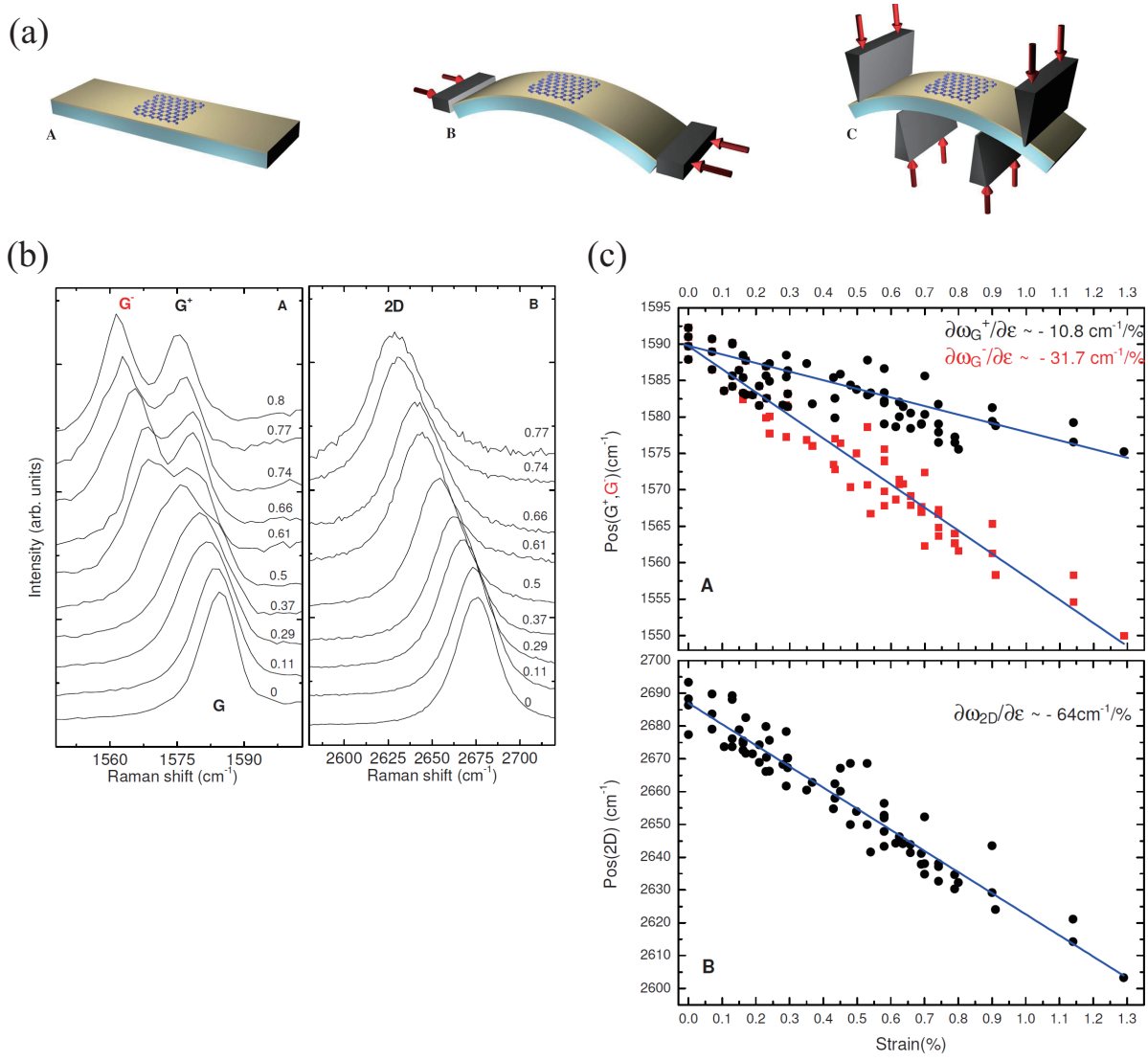

Figure 1.11: (a) Experimental setup for application of strain to graphene. A graphene film is placed on a flexible substrate and uniaxial strain is applied with two- or four-point bending apparatus. (b) Raman spectra near the G and 2D peaks as a function of the uniaxial strain. The G peak splits in two subbands G+ and G−, while the 2D peak does not split. (c) Position of G and 2D peaks as a function of the uniaxial strain. After Ref. [5].

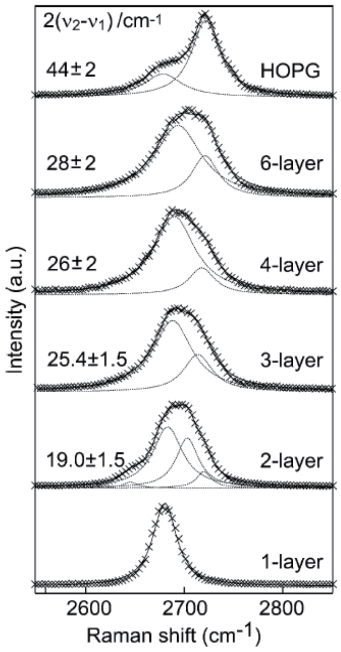

Figure 1.12: Raman 2D peaks for an increasing number of graphene layers along with HOPG as a bulk reference. The dashed lines show the Lorentzian peaks used to fit the data; the solid lines are the fitted results. On the left, the value for the splitting from bilayer graphene up to HOPG is presented. After Ref. [13].

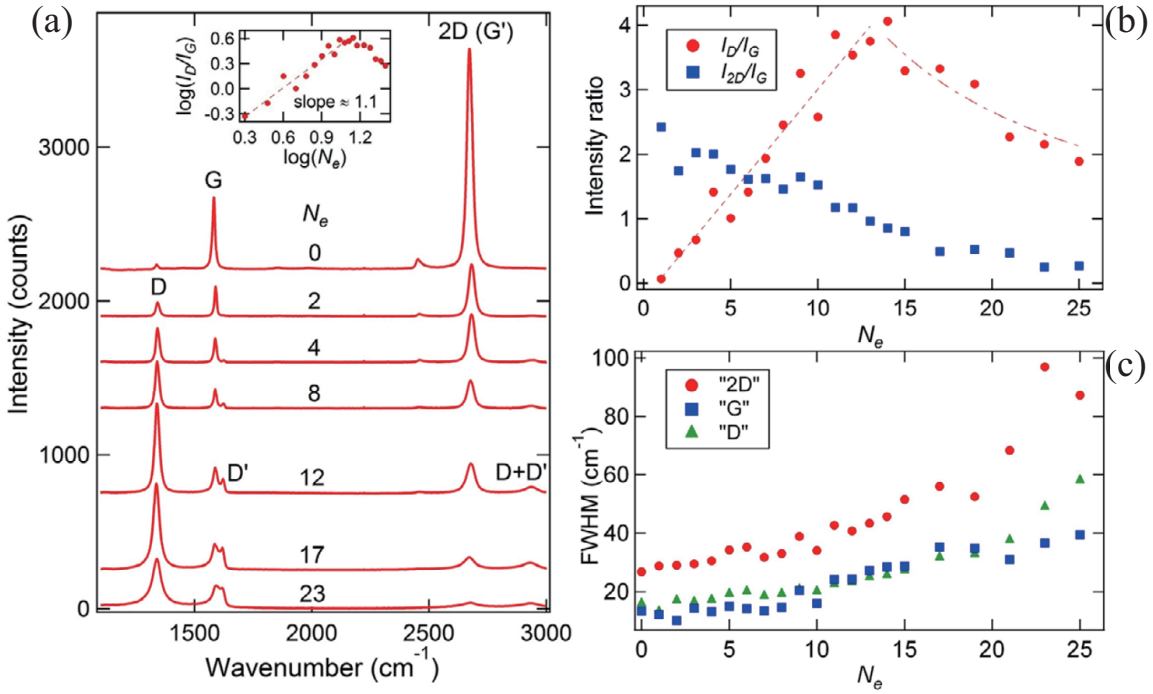

Figure 1.13: (a)Raman spectra of single layer graphene after various numbers of applied oxygen plasma pulses, N_e. The spectra are offset vertically for clarity. (b) $I_{\rm D}/I_{\rm G}$ and $I_{\rm 2D}/I_{\rm G}$ as a function of $N_{\rm e}$. The low-defect-density regime (stage 1, $N_{\rm e} \leq 13$) and the high-defect-density regime (stage 2) are seen. After Ref. [19].

($\sim$ 1350 cm^{-1}) to G band ($\sim$ 1580 cm^{-1}), $I_{\rm D}/I_{\rm G}$, reflects the amount of disorder in graphitic materials.

According to the three-stage classification of disorder, known as amorphization trajectory [14, 15], for crystalline graphite evolving into nanocrystalline graphene (stage 1), $I_{\rm D}/I_{\rm G}$ increases with the increase of disorder. Then, when nanocystalline graphite becomes mainly sp^2 amorphous carbon (stage 2), $I_{\rm D}/I_{\rm G}$ decreases. Stage 3 in the original amorphization trajectory for bulk graphite is characterized by further decrease in $I_{\rm D}/I_{\rm G}$. For graphene, stages 1 and 2 are relevant.

The evolution of the $I_{\rm D}/I_{\rm G}$ ratio by disorder has been reported by several authors.[16, 17, 18, 19] An example is shown in Fig. 1.13, in which the disorder is introduced by accumulated oxygen plasma pulses.[19]

For the quantitative evaluation of the amount of disorder, one needs to know the relationship between the Raman $I_{\rm D}/I_{\rm G}$ ratio and a physical quantity that characterizes the disorder density. So far, two cases are reported for the low-defect-density regime (stage 1), in which a crystalline size and an average distance between defects are used as relevant physical quantities.

Evaluation of defect density

(1) Crystalline size (3D nanographene)

In 1970, Tuinstra and Koenig [16] performed systematic Raman and X-ray diffraction studies of many graphitic samples with different in-plane crystallite sizes L_{a}. They found that the $I_{\mathrm{D}}/I_{\mathrm{G}}$ ratio was inversely proportional to the crystallite sizes L_{a}:

$$\frac{I_{\mathrm{D}}}{I_{\mathrm{G}}} = \frac{C(\lambda)}{L_a},$$

where the constant C for laser wavelength $\lambda = 514$ nm is ~ 4.4 nm. L_{a} was estimated from the width of the X-ray diffraction peaks. This relationship can be roughly understood with the fact that the number of carbon atoms in the crystalline, which contributes to I_{G}, is proportional to L_{a}^2, while the number of carbon atoms at the interface, which contributes to I_{D}, is proportional to L_{a}.

(2) Average distance between structural defects

In 2010, Lucchese *et al.* studied the relationship between the Raman $I_{\mathrm{D}}/I_{\mathrm{G}}$ ratio and the distance, L_{D}, between the structural defects which were induced by low energy (90 eV) Ar+ ion bombardment.[18] They obtained the following relationship for low defect densities:

$$\frac{I_{\mathrm{D}}}{I_{\mathrm{G}}} = \frac{C'(\lambda)}{L_{\mathrm{D}}^2}.$$

Here, L_{D} was estimated from the scanning tunneling microscope (STM) observation, and C' was 102 (nm^2) for laser wavelength $\lambda = 514$ nm.

This relationship is phenomenologically understood with the following model.[18] Here, one assumes that each defect produced by the ion bombardment involves M carbon atoms, which contribute to the Raman D band. When the defect density, D_{D}, is so small that the overlap between defect-affected areas can be ignored, $I_{\mathrm{D}}/I_{\mathrm{G}}$ is proportional to $M \times D_{\mathrm{D}}$. Since M is constant, $I_{\mathrm{D}}/I_{\mathrm{G}} \propto D_{\mathrm{D}} \propto 1/{L_{\mathrm{D}}}^2$.

For obtaining information on transport properties from Raman spectroscopy, one needs to know relationship between Raman spectra and a physical quantity that characterizes the transport. In this thesis, a relationship between the Raman $I_{\mathrm{D}}/I_{\mathrm{G}}$ ratio and the carrier mean free path will be derived. The reason we focus on the electron mean free path is the following. The mean free path reflects the density of all kinds of defects, so that this would be the most suitable quantity for characterizing the defect density. Furthermore, it can be easily estimated from the transport measurement.

1.3 Band gap formation in graphene

To take advantage of remarkable properties of graphene such as high mobility and large field effect for next generation electronic devices such as FETs, opening a band gap is indispensable. Several

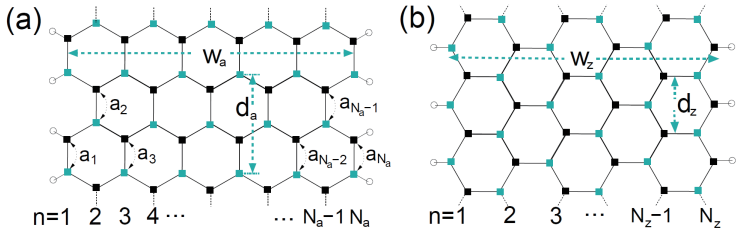

Figure 1.14: Schematics of (a) armchair and (b) zigzag graphene nanoribbons. The empty circles denote hydrogen atoms passivating the graphene edges. $N_{\rm a}$ and $N_{\rm z}$ denote the number of carbon atoms in the ribbon width in armchair and zigzag nanoribbons, respectively. After Ref. [20].

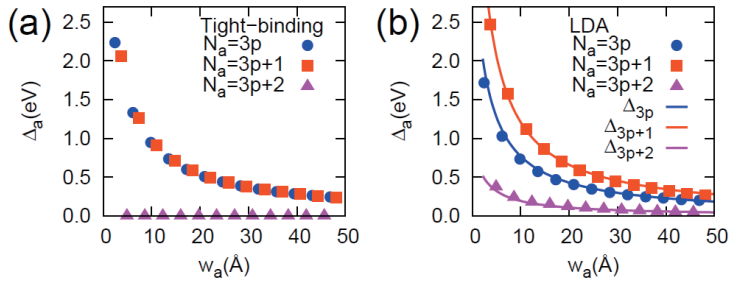

Figure 1.15: Ribbon width dependence of band gap in graphene nanoribbons within the tight binding approximation (a) and within the the first-principles calculation (b). After Ref. [20].

methods have been proposed for the band gap formation, including graphene nanoribbons and bilayer graphene under perpendicular electric fields. In this thesis, we deal with a relatively new and unexploited method in which graphene lattice strain plays a crucial role. In the following, the present status of two well-known methods for the band gap formation is reviewed, and theoretical predictions for gap formation using lattice strain are described.

1.3.1 Graphene nanoribbons

In narrow graphene strips, called graphene nanoribbons, confinement of carriers leads to band gap opening around the Dirac point. Two structures, armchair nanoribbons (Fig. 1.14(a)) and zigzag nanoribbons (Fig. 1.14(b)) have been intensively studied theoretically.

The magnitude of the band gap depends on the edge structure and ribbon width. The calculated band gaps of armchair nanoribbons within the tight-binding approximation are shown in Fig. 1.15(a).[20] When the number of carbon atoms in the ribbon width, $N_{\rm a}$, satisfies the relation, $N_{\rm a} = 3p + 2$ (p is a positive integer), the graphene nanoribbon behaves as a metal. If $N_{\rm a}$ takes other values, the graphene nanoribbon shows semiconducting properties. The energy gap $\Delta_{N_{\rm a}}$ is inversely proportional to the width in each group, $N_{\rm a} = 3p$ or $N_{\rm a} = 3p + 1$. For a particular value

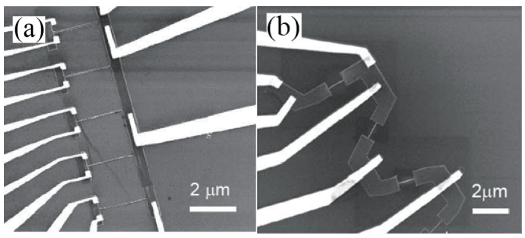

Figure 1.16: SEM images of graphene nanoribbons. (a) Parallel graphene nanoribbons with varying width. (b) Ribbons of uniform width and varying relative orientation. After Ref. [21].

of p, Δ_{N_a} yields a relationship,

$$\Delta_{3p} \geq \Delta_{3p+1} > \Delta_{3p+2} = 0.$$

On the other hand, zigzag nanoribbons in the tight-binding approximation are metallic and have a flat band at $\epsilon = 0$. The flat band appears due to the localization of the wave function near zigzag edges, and its amplitude decays into the center of the nanoribbon.

In first-principles calculation using the local (spin) density approximation (LSDA), energy gap depending on the ribbon width appears both in zigzag and armchair nanoribbons.[20] In the case of the armchair edge (Fig. 1.15(b)), the magnitude of the gap has a relationship:

$$\Delta_{3p} \geq \Delta_{3p+1} > \Delta_{3p+2} (\neq 0).$$

The difference from the tight-binding results is caused by deformation of the graphene lattice at the edges due to the hydrogen passivation. On the other hand, the results for the armchair nanoribbons show an energy gap which is well fitted by

$$\Delta_{3p} = \frac{0.933}{w[\mathrm{nm}] + 1.5},$$

for ribbon width $w > 1$ nm.

Experimental transport properties of graphene nanoribbon were first reported by Han *et al.* in 2007.[21] In this experiment, two different types of the graphene nanoribbon devices were fabricated by electron beam lithography followed by oxygen plasma etching using a negative tone electron beam resist (hydrogen silsesquioxane, HSQ). One kind of devices contained many ribbons with varying width running parallel (Fig. 1.16(a)). The other had ribbons of uniform width and varying relative orientation (Fig. 1.16(b)). The nanoribbon widths ranged from 10 to 100 nm and the lengths were $1 - 2$ μm. Transport measurements showed suppression of the conductance near the charge neutrality point, which enhanced at lower temperatures and in narrower ribbons (Fig. 1.17), but the dependence of the orientation was not observed. The authors attributed the suppression of conductance to the existence of the energy gap, which was well fitted by

$$E_g = \frac{a}{w + w^*},$$

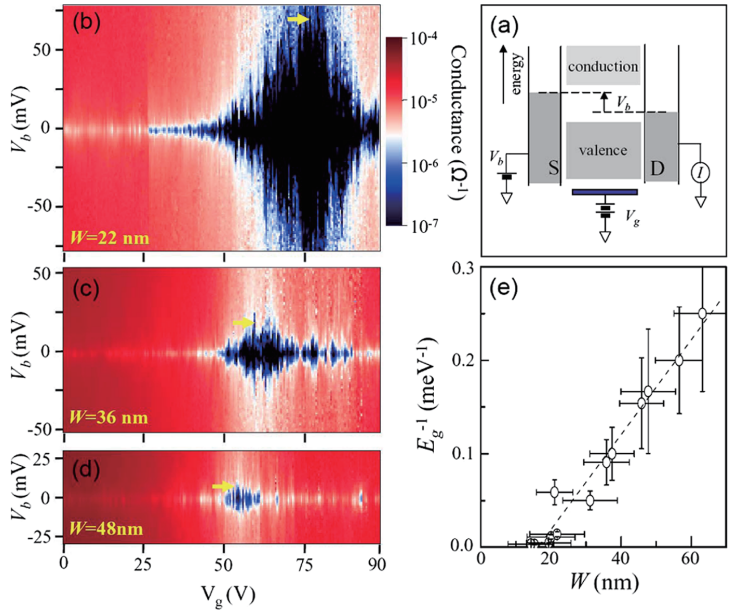

Figure 1.17: (a) Schematic energy band diagram of a graphene nanoribbon with applied bias voltage $V_{\rm b}$. The current I was controlled by both source-drain bias $V_{\rm b}$ and gate voltage $V_{\rm g}$. (b-d) The differential conductance (dI/dV) of three representative graphene nanoribbons of width of 22, 36, and 48 nm as a function of $V_{\rm b}$ and $V_{\rm g}$ measured at $T = 1.6$ K. The dark color corresponds to low conductance, indicating the suppression of the conductance near the charge neutrality point. (e) Inverse of energy gap $E_{\rm g}$ vs the ribbon width W with a liner fit of the data. After Ref. [21].

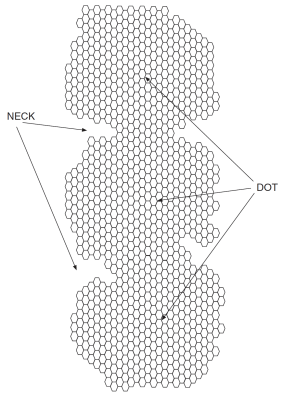

Figure 1.18: Schematic illustration of graphene nanoribbon with edge roughness. The edge roughness forms necks and dots. After Ref. [22].

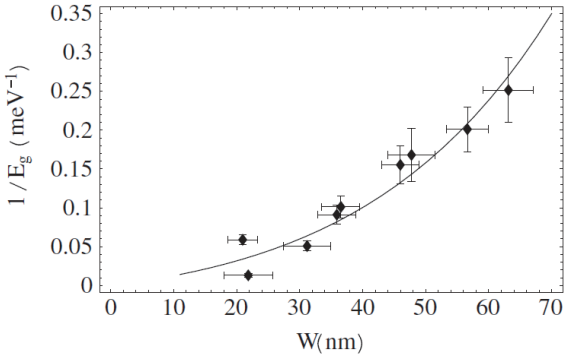

Figure 1.19: Comparison between experimental data of Ref. [21] (dots) and the theoretical result (solid curve). After Ref. [22].

where w is the ribbon width, $a = 0.2$ eVnm and $w^* = 16$ nm. Here w^* is the inactive width attributed to localized states near ribbon edges caused by structural disorder from sample fabrication processes. Later, Sols *et al.* [22] showed theoretically that the data obtained by Han *et al.* can be quantitatively explained by the Coulomb blockade effect caused by the edge roughness. They considered that the structure shown in Fig. 1.18, in which the edge roughness forms the necks and dots, caused the Coulomb blockade effect. Figure 1.19 compares the experimental data of Han *et al.* with the theoretical result taking into account the Coulomb blockade effect.[22]

The existence of Coulomb blockade effect in graphene nanoribbons has been experimentally confirmed by several groups. Figure 1.20 is an example [23], which shows the irregular Coulomb diamond structure with gate voltage modulation of the current voltage characteristics around the origin. This result indicates the existence of several quantum dots in the ribbon. A similar behavior in a graphene nanoribbon was reported by Miyazaki *et al.*[24]

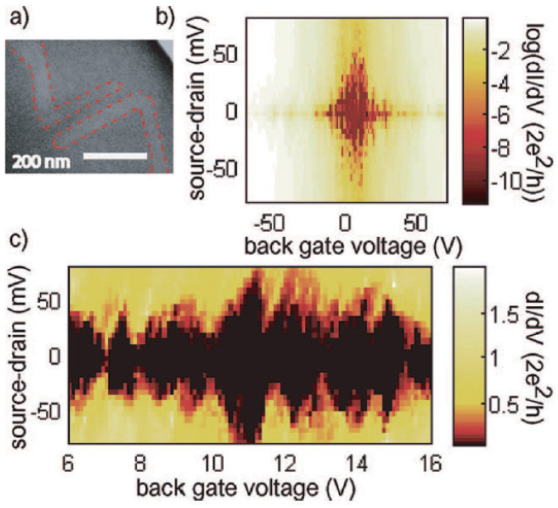

Figure 1.20: (a) SEM image of graphene nanoribbon 250 nm in length and 40 nm in width. Dashed red lines are guides to the eye indicating the boundary of the etched area. (b) Logarithmic map of the differential conductance (dI/dV) vs back gate voltage and source-drain bias, showing conduction gap. (c) dI/dV over a smaller range, showing the irregular Coulomb diamond structure. After Ref. [23].

Besides, Han *et al.* investigated the temperature dependence of conductance minimum in lithographically defined graphene nanoribbons with different geometrical capacitances. They observed that thermal activation energy heavily depended upon the capacitance at high temperatures (Fig. 1.21), indicating that the Coulomb blockade effect provided a substantial portion of the observed energy gap.

A similar results has been observed in chemically derived nano ribbons. These results show that the Coulomb blockade effect dominates over the effect of confinement, indicating that the mobility of nanoribbons is significantly suppressed in experiments. This is not favorable for the electronics applications.

1.3.2 Bilayer graphene in perpendicular electric fields

In bilayer graphene under perpendicular electric fields, a band gap opens between the conduction and valence bands, even without any structural confinement.[26] This is due to breaking of the inversion symmetry between two layers by applying an electric field perpendicular to bilayer graphene plane. The theory assumed that the bilayer graphene has AB (Bernal) stacking structure, as shown in Fig. 1.22, in which the B-sublattice of the top layer sits on top of the A-sublattice in the bottom layer. Theoretical prediction shows that the band gap depends on the electric field and reaches ~ 300 meV (Fig. 1.23).[26]

Experimentally, an electric field is applied by chemical doping on graphene [27, 28] and/or

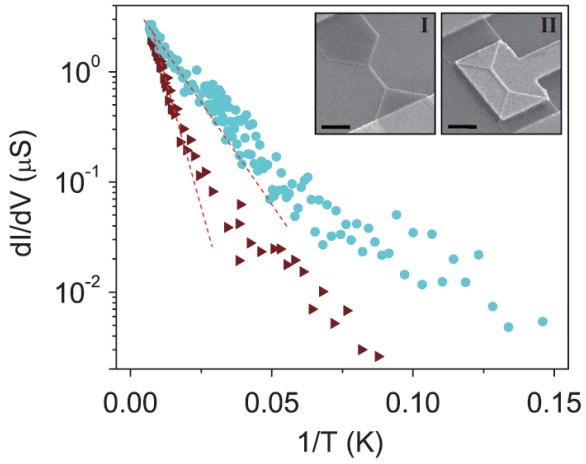

Figure 1.21: Temperature dependence of the conductance minimum for dual gated (circles) and back gated (triangles) graphene nanoribbons with the similar width and length. The dashed lines are Arrhenius fits in the high temperature regime. (Inset) SEM images of back gated (left) and dual gated (right) devices. Scale bar represents 500 nm. After Ref. [25].

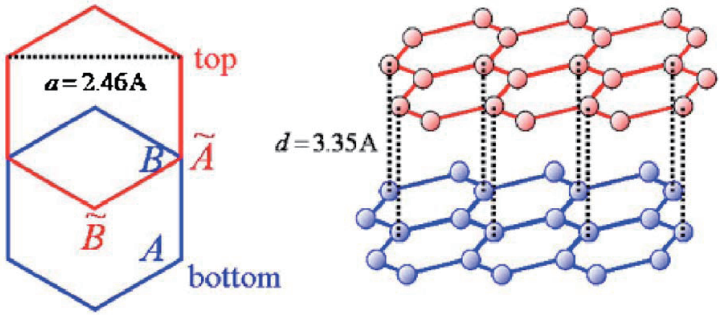

Figure 1.22: Structure of AB (Bernal) stacking bilayer graphene. After Ref. [26].

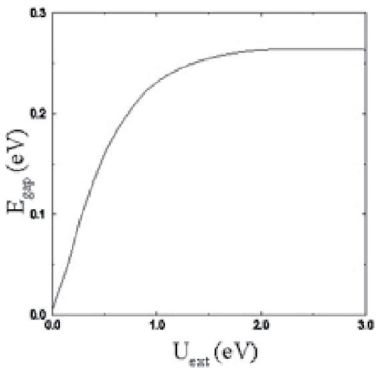

Figure 1.23: Energy gap as a function of the potential difference U_{ext} between the two layers. After Ref. [26].

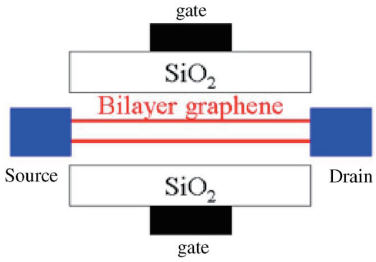

Figure 1.24: Schematic illustration of dual-gated bilayer graphene FET. Bilayer graphene is sandwiched between top and bottom gates. After Ref. [26].

by gate electric fields.[29, 30, 31, 32, 33] In the former case, ammonia and potassium have been used as the dopants adsorbed on graphene, while in the latter, a dual-gate structure (Fig. 1.24) is employed.

So far, band gap formation has been confirmed in optical spectroscopic measurements such as angle-resolved photoemission spectroscopy (ARPES) [28] and infrared spectroscopy.[30, 31] The observed band gap depended on the gate electric field and reached ~ 200 meV which agreed well with the theoretical prediction.

On the other hand, in the first paper on transport measurement [29], although an insulating behavior was observed with the increase of resistance in lowering temperature, the temperature dependence of resistance at low temperatures (below 50 K) was not the thermal activation type,

$$G \propto \exp(-\epsilon_{\rm a}/k_{\rm B}T),$$

which is regarded as a direct evidence of the band gap opening with the gap magnitude of $\epsilon_{\rm g} = 2\epsilon_{\rm a}$, but of the variable range hopping type,

$$G \propto \exp(-(T_{\rm h}/T)^{\frac{1}{3}}),$$

which is typically observed in strongly disordered two-dimensional systems. ($k_{\rm B}$ is Boltzmann constant, T is temperature, and $T_{\rm h}$ is a constant.) It was claimed that the experimentally obtained band gap was below 10 meV, despite that the device structure was similar to those used in Ref. [30], which reported a band gap over 200 meV in optical spectroscopy.

Later, Miyazaki *et al.* [33] showed that the temperature dependence of the conductance between 77 K and 200 K was explained as the sum of the thermally activated conduction and the two-dimensional variable range hopping conduction,

$$G = C_1 \exp(-(\epsilon_{\rm a}/k_{\rm B}T)) + C_2 \exp(-(T_{\rm h}/T)^{\frac{1}{3}})$$

where, C_1 and C_2 are constants. They found that the energy gap, $\epsilon_{\rm g} = 2\epsilon_{\rm a}$, agreed with the theoretical value for electric field values ranging $0 - 1.3$ V/nm, and was unrelated to the mobility of bilayer graphene. However, the variable range hopping caused current leakage, leading to

degradation of the FET operation. They demonstrated that the contribution of variable range hopping becomes smaller in bilayer graphene with higher mobility. These results indicate that increasing mobility and/or applying higher electric fields is crucial for improving the performance of the bilayer graphene FETs. Here, we note that single layer graphene exhibits higher mobility than bilayer graphene does, due to the massless feature of carriers.

1.3.3 Energy gap formation using lattice strain

Although above two methods are major candidates for the method of band gap formation, there are serious problems as already described: In graphene nanoribbons, the band gap is strongly influenced by the geometry of graphene nanoribbon, such as a ribbon width, edge orientation, edge structure, and chemical termination of edges. Thus, edge formation with atomic precision is required, while real graphene nanoribbons have edge roughness which exerts serious influence on electron transport. As for bilayer graphene under perpendicular electrical fields, a significant amount of the leakage current has been observed due to the intrinsic low mobility. For the successful application of bilayer graphene to FETs, improvement of mobility is required.

In this section, another method of transport gap formation which uses lattice strain is introduced.

Strain effect in graphene

Due to Dirac fermionic properties of charge carriers in graphene, mechanical strain in graphene lattice produces a vector potential: Here, we assume that due to lattice strain, the nearest neighbor transfer integrals (hopping parameters) take different values, t_1, t_2, and t_3 for the nearest neighbor vectors $(a/2\sqrt{3}, a/2)$, $(a/2\sqrt{3}, -a/2)$ and $(-a/\sqrt{3}, 0)$, respectively. The tight binding approximation leads to the following effective Hamiltonian for electrons around K point:

$$H = \vec{\sigma}(-i\hbar v_{\mathrm{F}}\vec{\nabla} - \vec{A}),$$

where $\vec{\sigma}$ is the Pauli matrices:

$$\sigma_x = \begin{pmatrix} 0 & 1 \\ 1 & 0 \end{pmatrix}, \quad \sigma_y = \begin{pmatrix} 0 & -i \\ i & 0 \end{pmatrix},$$

and the resultant *vector potential* is given by

$$\begin{aligned} A_x &= \frac{\sqrt{3}}{2}(t_3 - t_2), \\ A_y &= \frac{1}{2}(t_2 + t_3 - 2t_1). \end{aligned}$$

Thus, strain leads to a gauge field similar to that in electrodynamics.[34]

In a weakly deformed lattice in which the interatomic distance is close to that of unstrained graphene, the strain-induced vector potential is given by

$$\vec{A} = \frac{\beta}{a} \begin{pmatrix} u_{xx} - u_{yy} \\ -2u_{xy} \end{pmatrix},$$

using the two-dimensional strain field:

$$u_{xx} = \frac{\partial u_x}{\partial x}, \quad u_{yy} = \frac{\partial u_y}{\partial y},$$
$$u_{xy} = \frac{1}{2}\left(\frac{\partial u_x}{\partial y} + \frac{\partial u_y}{\partial x}\right).$$

Here, a is the lattice constant, $\beta = \delta \ln t / \delta \ln a \approx 2$, (u_x, u_y) is the atom displacement, and the x-axis is chosen along the zigzag direction of graphene lattice.[35] Such vector potential horizontally shifts the Dirac cones, as a usual vector potential does. Here we note that the Dirac cones located at K and K' points are shifted in the opposite directions, which confirms that the time-reversal symmetry is not violated by strain-induced vector potentials.

Additionally, one can expect that strain-induced vector potential generates a pseudomagnetic field B_s,

$$B_\mathrm{s} = \frac{\partial A_y}{\partial x} - \frac{\partial A_x}{\partial y}. \tag{1.5}$$

In contrast to the (real) magnetic field, the pseudomagnetic field has opposite signs for graphene's two valleys K and K'. From this formula, we can see that B_s can be created only by non-uniform shear strain. Indeed, an isotropic strain leads to $A = 0$ and a uniform strain leads to $A = \mathrm{const}$, both of which yield zero B_s.

Experimentally, the existence of the pseudomagnetic field was demonstrated by Levy *et al.* in 2010.[36] They performed scanning tunneling spectroscopy (STS) of graphene nanobubbles, which were formed in CVD-grown graphene on a platinum (111) surface (Fig. 1.25(a)). On the top of a graphene nanobubble, Landau levels corresponding to a pseudomagnetic field of more than 300 T was observed (Fig. 1.25(b)).

Theories tell that nonuniform lattice strain can be used for the transport gap formation in graphene.[35, 6] So far, two methods have been proposed. The first uses triangular periodic strain fields [35] and the second uses one-dimensional local strain.[6] These strains for gap formation are expected to be realized not by cutting graphene but by patterning the substrate. Therefore, electron transport will not be limited by the existence of rough edges, and, in principle, high mobility is expected. In the following, these two methods are briefly explained.

Theoretical prediction 1 : Strain superlattice with triangular symmetry

Guinea *et al.* [35] suggested a concept for band gap formation by strained graphene superlattice. When a graphene film is placed on top of a corrugated substrate which has a triangular landscape,

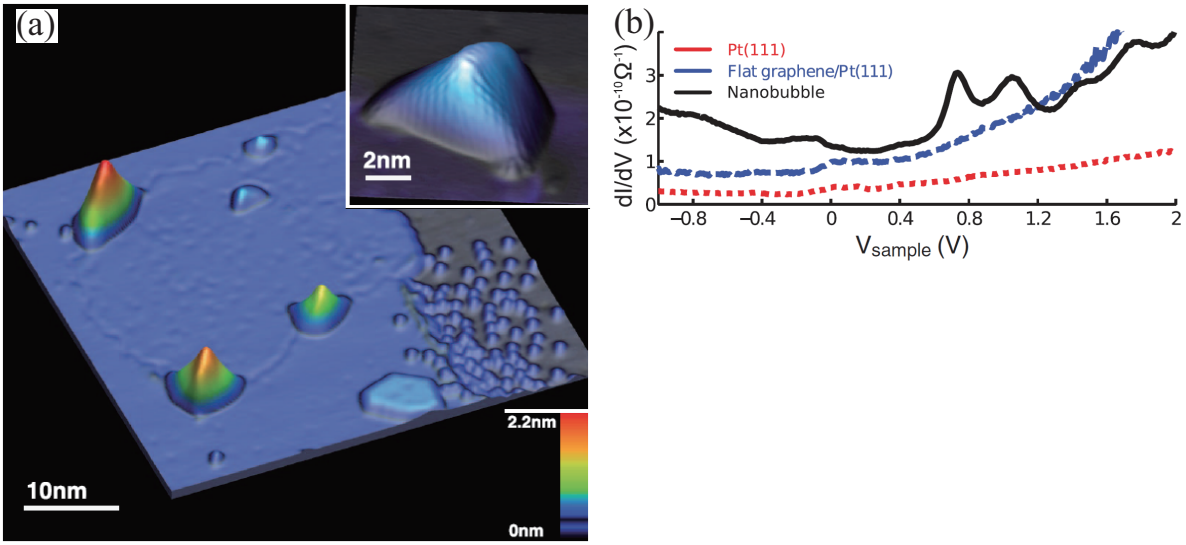

Figure 1.25: (a) STM image of graphene monolayer patch on Pt(111) with four nanobubbles. (Inset) High-resolution image of a graphene nanobubble. (b) STS spectra of bare Pt(111), flat graphene on Pt(111) and the center of graphene nanobubble. After Ref. [36].

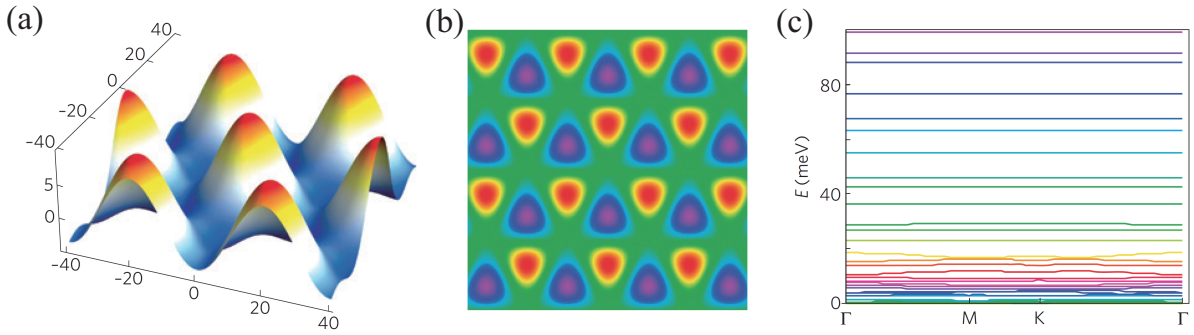

Figure 1.26: (a) Strain with triangular symmetry can be created by placed a graphene film on a corrugated substrate. (b) The distribution of pseudomagnetic field. (c) The resulting energy spectrum, showing the multiple gap at higher energy. After Ref. [35].

as shown in Fig. 1.26(a), the resulting pseudomagnetic field forms a superlattice, as shown in Fig. 1.26(b). Figure 1.26(c) shows the resulting energy spectrum, in which continuous bands of electronic states appear close to zero ϵ, while at higher ϵ, multiple gaps are seen. For the lateral periodicity of 40 nm and maximum strain of 0.1%, the pseudomagnetic field reaches $B_s = \pm 0.5$ T, and the gap at high energies are over 10 meV. Smaller period as well as larger strain leads to increase of the gap.

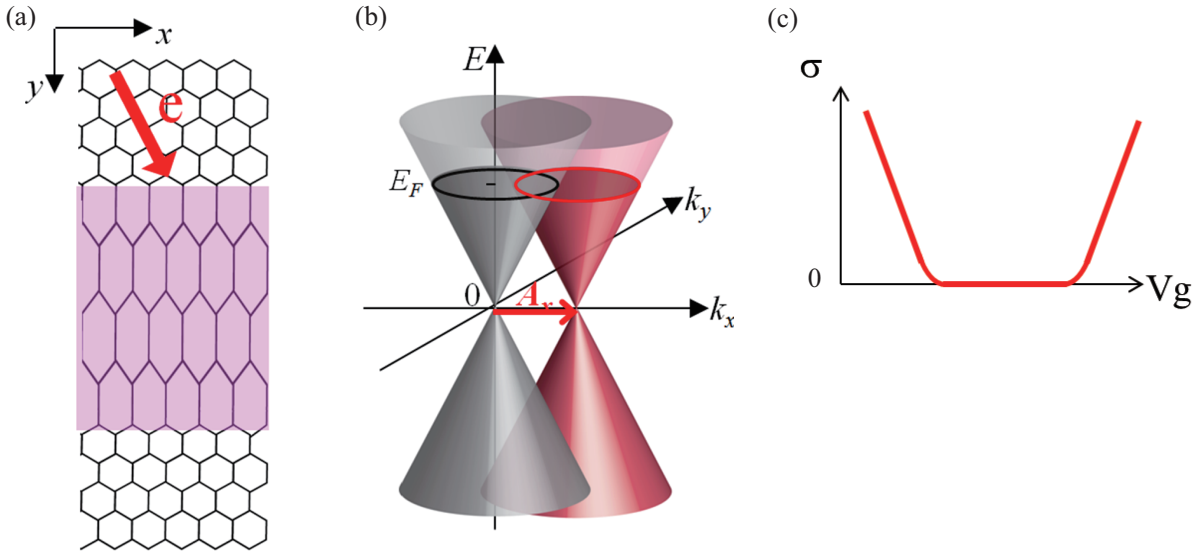

Figure 1.27: (a) Schematic illustration of graphene with one dimensional local strain. Red arrow represents incidence of an electron. (b) Dirac cones of graphene portions with strain (red) and without strain (gray). (c) Gate voltage dependence of conductance in graphene with one dimensional local strain. Conductivity vanishes within a certain gate-voltage range.

Theoretical prediction 2 : One dimensional local strain

In a theory suggested by Pereira and Neto[6], a part of a graphene film is stretched in one direction, as shown in Fig. 1.27(a). In this case, the Dirac cone in a strained region shifts. Figure 1.27(b) depicts Dirac cones at strained (red) and unstrained (gray) regions for a strain parallel to the armchair direction (y-axis).

The authors of Ref. [6] assumed that when an electron is injected to the interface, the momentum component parallel to the interface (p_x) is conserved. As a result, only electrons which have momentum p_x at the overlap region of two Dirac circles (solid circles in Fig. 1.27(b)) can penetrate into the strained region. In particular, for the small Fermi energies in which there is no overlap of the Dirac circles, the electron is perfectly reflected. As a result, electrical transport shows a behavior different from the case of unstrained graphene. Figure 1.27(c) shows the resulting gate voltage dependence of conductance, which exhibits a transport gap. According to the theory, for a strain in the armchair direction, the transport gap corresponds to the change of the nearest-neighbor hopping integral, written by,

$$\delta t = t_0 \left(1 - e^{-3.37\lambda}\right),$$

where $t_0 = 2.7$ eV is the nearest neighbor transfer integral of unstrained graphene and λ is an amount of strain. For 10% strain, the gap reaches 0.8 eV.

Experimentally, nobody has confirmed the modulation of electron transport by strain. This is

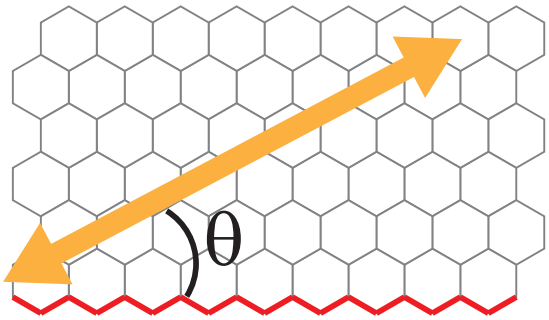

Figure 1.28: Schematic illustration of graphene with the one dimentional local strain.

because a method for controlling local lattice strain has not been developed for graphene. So far, in experimental studies of graphene's lattice strain, either incidentally formed strain or uniform strain has been used. However, these strains are not suitable for the gap formation. A reliable method for producing designed local strain is required.

Orientation dependence

When a one dimensional local strain is applied in an arbitrary direction, as shown in Fig. 1.28, the resulting vector potential is given by

$$\boldsymbol{A} \propto \gamma \begin{pmatrix} \cos(-2\theta) \\ \sin(-2\theta) \end{pmatrix},$$

where γ is the amount of strain and θ is the angle between the strain direction and the zigzag direction. This means that the direction of the vector potential, *i.e.*, the direction of the shift of the Dirac cone in the strained region is -2θ, indicating that the transmission of an electron through the interface strongly depends on the direction of the interface and the angle, ζ, between the interface and the strain direction.

Now, as an example, we consider two cases where the interface between the strained region and unstrained region is parallel to the zigzag direction or to the armchair direction (Fig. 1.29):

- In the case of an interface parallel to the zigzag direction (Fig. 1.29(a)), when the strain is parallel to or perpendicular to the interface ($\zeta = 0°$ or $90°$) , the resulting shift of the Dirac cone is parallel to the interface, while for $\zeta = 45°$, the shift of the Dirac cone is perpendicular to the interface. Thus, perfect transmission occurs for $\zeta = 45°$.

- In the case of an interface parallel to the armchair direction (Fig. 1.29(b)), the result is opposite to the above case. Perfect transmission occurs for $\zeta = 0°$ and $90°$.

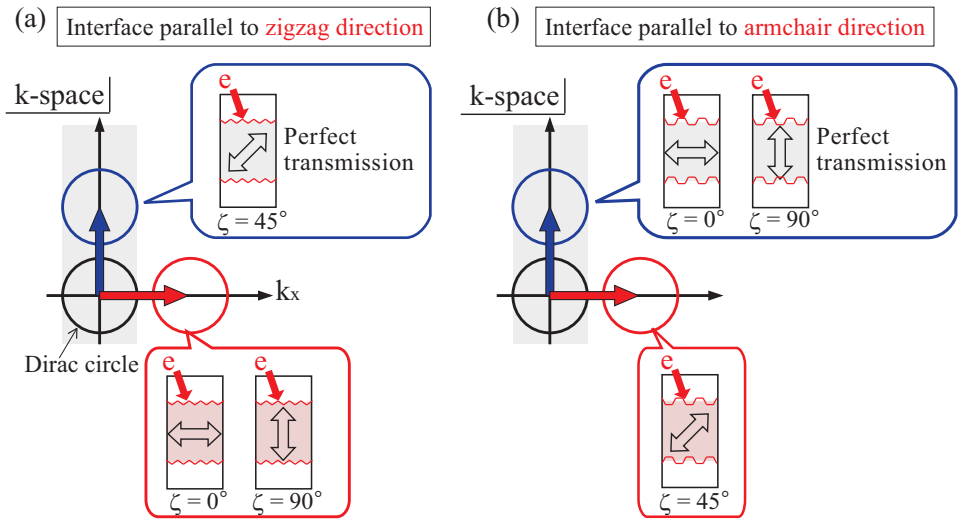

Figure 1.29: The direction of the Dirac cone shift for interfaces parallel to the zigzag direction (a) and to the armchair direction (b).

1.4 Purpose of this thesis

In this thesis, we first focus on the effect of local lattice strain on the graphene electron transport. As explained above, this field is important from the viewpoint of both fundamental science and applications, but is completely unexploited. For this purpose, we need to develop methods for inducing local lattice strain in graphene in a controlled manner.

In the second part of this thesis, we deal with the effect of electron beam irradiation on graphene transport properties. Electron beam irradiation is commonly used in graphene nanofabrication processes, and this is the case in our study on local lattice strain. So we need to know the influence of electron beam irradiation on graphene transport properties and minimize it. We combine Raman spectroscopy with transport measurement, and derived a relationship between the Raman $I_{\mathrm{D}}/I_{\mathrm{G}}$ ratio and the carrier mean free path.

Reference

[1] A. Kanda, Experimental approaches to graphene electron transport for device applications, in "Physics and Chemistry of Graphene: Nanographene to Graphene" (edited by T. Enoki and T. Ando), pp. 89–205, Pan Stanford Publishing (2013)

[2] K. S. Novoselov, A. K. Geim, S. V. Morozov, D. Jiang, M. I. Katsnelson, I. V. Grigorieva, S. V. Dubonos, and A. A. Firsov, Two-dimensional gas of massless Dirac fermions in graphene, Nature, 438, 197–200 (2005)

[3] Y.-W. Tan , Y. Zhang,. K. Bolotin, Y. Zhao, S. Adam, E. H. Hwang, S. Das Sarma, H. L. Stormer, and P. Kim, Measurement of Scattering Rate and Minimum Conductivity in Graphene, Phys. Rev. Lett., 99, 246803 (2007)

[4] N. H. Shon and T. Ando, Quantum Transport in Two-Dimensional Graphite System, J. Phys. Soc. Jpn, 67, 2421–2429 (1998)

[5] K. Ziegler, Robust Transport Properties in Graphene, Phys. Rev. Lett., 97, 266802 (2006)

[6] K. Nomura and A. H. MacDonald, Quantum Transport of Massless Dirac Fermions, *Phys. Rev. Lett.*, **98**, 076602 (2007)

[7] J. Martin, N. Akerman, G. Ulbricht, T. Lohmann, J. H. Smet, K. von Klitzing and A. Yacoby, Observation of electron-hole puddles in graphene using a scanning single-electron transistor, Nat. Phys. 4, 144 – 148 (2008)

[8] S. Adam, E. H. Hwang, V. M. Galitski, and S. Das Sarma, A self-consistent theory for graphene transport, Proc. Nat. Acad. Sci. USA, 104, 18392–18397 (2007)

[9] J. H. Chen, C. Jang, S. Adam, M. S. Fuhrer, E. D. Williams, and M. Ishigami, Charged-impurity scattering in graphene, Nat. Phys. 4, 377–381 (2008)

[10] A. Das, S. Pisana, B. Chakraborty, S. Piscanec, S. K. Saha, U. V. Waghmare, K. S. Novoselov, H. R. Krishnamurthy, A. K. Geim, A. C. Ferrari and A. K. Sood, Monitoring dopants by Raman scattering in an electrochemically top-gated graphene transistor, nature nanotechnology 3, 210–215 (2008)

[11] T. M. G. Mohiuddin, A. Lombardo, R. R. Nair, A. Bonetti, G. Savini, R. Jalil, N. Bonini, D. M. Basko, C. Galiotis, N. Marzari, K. S. Novoselov, A. K. Geim, and A. C. Ferrari, Uniaxial strain in graphene by Raman spectroscopy: G peak splitting, Gruneisen parameters, and sample orientation, Phys. Rev. B 79, 205433 (2009)

[12] G. Tsoukleri, J. Parthenios, K. Papagelis, R. Jalil, A. C. Ferrari, A. K. Geim, K. S. Novoselov, C. Galiotis, Subjecting a graphene monolayer to tension and compression. Small 5, 2397–2402 (2009)

[13] D. Graf, F. Molitor, K. Ensslin, C. Stampfer, A. Jungen, C. Hierold, and L. Wirtz, Spatially Resolved Raman Spectroscopy of Single- and Few-Layer Graphene, Nano Lett., 7, 238–242 (2007)

[14] A. C. Ferrari and J. Robertson, Interpretation of Raman spectra of disordered and amorphous carbon, Phys. Rev. B 61 14095–14107 (2000)

[15] A. C. Ferrari and J. Robertson, Resonant Raman spectroscopy of disordered, amorphous, and diamondlike carbon, Phys. Rev. B 64 075414 (2001)

[16] F. Tuinstra and J. L. Koenig, Raman Spectrum of Graphite, Chem. Phys. 53 1126–1130 (1970)

[17] L. G. Cancado,a, K. Takai, T. Enoki, M. Endo, Y. A. Kim, H. Mizusaki, A. Jorio, L. N. Coelho, R. Magalhaes-Paniago, and M. A. Pimenta, General equation for the determination of the crystallite size La of nanographite by Raman spectroscopy, Appl. Phys. Lett. 88, 163106 (2006)

[18] M. M. Lucchese, F. Stavale, E. H. Martins Ferreira, C. Vilani, M. V. O. Moutinho, Rodrigo B. Capaz, C. A. Achete, A. Jorio, Quantifying ion-induced defects and Raman relaxation length in graphene, Carbon 48, 1592–1597 (2010)

[19] I. Childres, L. A. Jauregui, J. Tian and Y. P. Chen, Effect of oxygen plasma etching on graphene studied using Raman spectroscopy and electronic transport measurements, New J. Phys. 13 025008 (2011)

[20] Y. Kobayashi, K. Fukui, T. Enoki, K. Kusakabe, and Y. Kaburagi, Observation of zigzag and armchair edges of graphite using scanning tunneling microscopy and spectroscopy, Phys. Rev. B 71, 193406 (2005)

[21] M. Y. Han, B. Ozyilmaz, Y. Zhang, and P. Kim, Energy Band-Gap Engineering of Graphene Nanoribbons, Phys. Rev. Lett., 98, 206805 (2007)

[22] F. Sols, F. Guinea, and A. H. Castro Neto, Coulomb Blockade in Graphene Nanoribbons, Phys. Rev. Lett. 99, 166803 (2007)

[23] K. Todd, H. T. Chou, S. Amasha and D. Goldhaber-Gordon, Quantum Dot Behavior in Graphene Nanoconstrictions, Nano Lett. 9, 1 416–421 (2009)

[24] H. Miyazaki, S. Odaka, T. Sato, S. Tanaka, H. Goto, A. Kanda, K. Tsukagoshi, Y. Ootuka, and Y. Aoyagi, Coulomb Blockade Oscillations in Narrow Corrugated Graphite Ribbons, App. Phys. Express., 1, 024001 (2008)

[25] M. Y. Han, J. C. Brant, and P. Kim, Electron Transport in Disordered Graphene Nanoribbons, Phys. Rev. Lett., 104, 056801 (2010)

[26] H. Min, B. Sahu, S. K. Banerjee, and A. H. MacDonald, Ab initio theory of gate induced gaps in graphene bilayers, Phys. Rev. B 75, 155115 (2007)

[27] E. V. Castro, K. S. Novoselov, S. V. Norozov, N. M. R. Peres, J. M. B. Lopes dos Santos, J. Nilsson, F. Guinea, A. K. Geim, and A. H. Castro Neto, Biased Bilayer Graphene: Semiconductor with a Gap Tunable by the Electric Field Effect, Phys. Rev. Lett., 99, 216802 (2007)

[28] T. Ohta, A. Bostwick, T. Seyller, K. Horn, and E. Rotenberg, Controlling the Electronic Structure of Bilayer Graphene, Science, 313, 951–954 (2006)

[29] J. B. Oostinga, H. B. Heersche, L. Liu, A. F. Morpurgo, and L. M. K. Vandersypen, Gate-induced insulating state in bilayer graphene devices, Nat. Mater., 7, 151–157 (2008)

[30] Y. Zhang, T. Tang, C. Girit, Z. Hao, M. C. Martin, A. Zettl, M. F. Crommie, Y. R. Shen, and F. Wang, Direct observation of a widely tunable bandgap in bilayer graphene, Nature, 459, 820–823 (2009)

[31] K. F. Mak, C. H. Lui, J. Shan, and T. F. Heinz, Observation of an Electric-Field-Induced Band Gap in Bilayer Graphene by Infrared Spectroscopy, Phys. Rev. Lett., 102, 256405 (2009)

[32] F. Xia, D. B. Farmer, Y.-M. Lin, and Ph. Avouris, Graphene Field-Effect Transistors with High On/Off Current Ratio and Large Transport Band Gap at Room Temperature, Nano Lett., 10, 715–718 (2010)

[33] H. Miyazaki, K. Tsukagoshi, A. Kanda, M. Otani, and S. Okada, Influence of Disorder on Conductance in Bilayer Graphene under Perpendicular Electric Field, Nano Lett., 10, 3888–3892 (2010)

[34] H. Suzuura and T. Ando, Phonons and electron-phonon scattering in carbon nanotubes, Phys. Rev. B 65, 235412 (2002)

[35] F. Guinea, M. I. Katsnelson and A. K. Geim, Energy gaps and a zero-field quantum Hall effect in graphene by strain engineering, Nat. Phys. 6, 30–33 (2010)

[36] N. Levy, S. A. Burke, K. L. Meaker, M. Panlasigui, A. Zettl, F. Guinea, A. H. Castro Neto, M. F. Crommie, Strain-Induced Pseudo Magnetic Fields Greater Than 300 Tesla in Graphene Nanobubbles, Science 329, 544 (2010)

[37] Vitor M. Pereira and A. H. Castro Neto, Strain Engineering of Graphene's Electronic Structure, Phys. Rev. Lett., 103, 046801 (2009)

Chapter 2

Experimental technique

2.1 Sample fabrication

Here we describe a general method of graphene sample fabrication. Special procedures which depend on each experiment will be describes in later chapters.

2.1.1 Preparation of Si substrate with address markers

Scotch tape method (described later) allows one to obtain high quality graphene films on a Si substrate, but one cannot control the position of graphene. So, we should determine the position of graphene placed on the Si substrate. For this purpose, we use a Si substrate with address makers which indicate the graphene's position. In the following, fabrication of address markers is described.

(1) Spin-coat of photoresist

First, we heat a Si substrate to remove water on the surface at 180 degrees. Then, two kinds of resists are spin-coated on the substrate. The first is HMDS (Hexamethyle-Disilazane) and the second is Microposit S1808. Here, HMDS is used as an adhesive layer. Coating conditions are 500 rpm (5 sec) for HMDS, and 500 rpm (5 sec) followed by 3000 rpm (60 sec) for S1808. After the spin-coat, Si substrate is annealed at 180 degrees on a hot plate.

(2) Exposure

Si substrate is exposed to ultraviolet light for 7 seconds. The pattern of address markers is shown in Fig. 2.1. Address markers are placed with 500 μm interval and their shape represents its coordinate on the substrate.

(3) Development

First, the exposed substrate is soaked in monochlorobenzene for 1 minute. Then it is dried by nitrogen blow. Next, we soak the substrate in MF319 developer for 3 minutes and dry it with

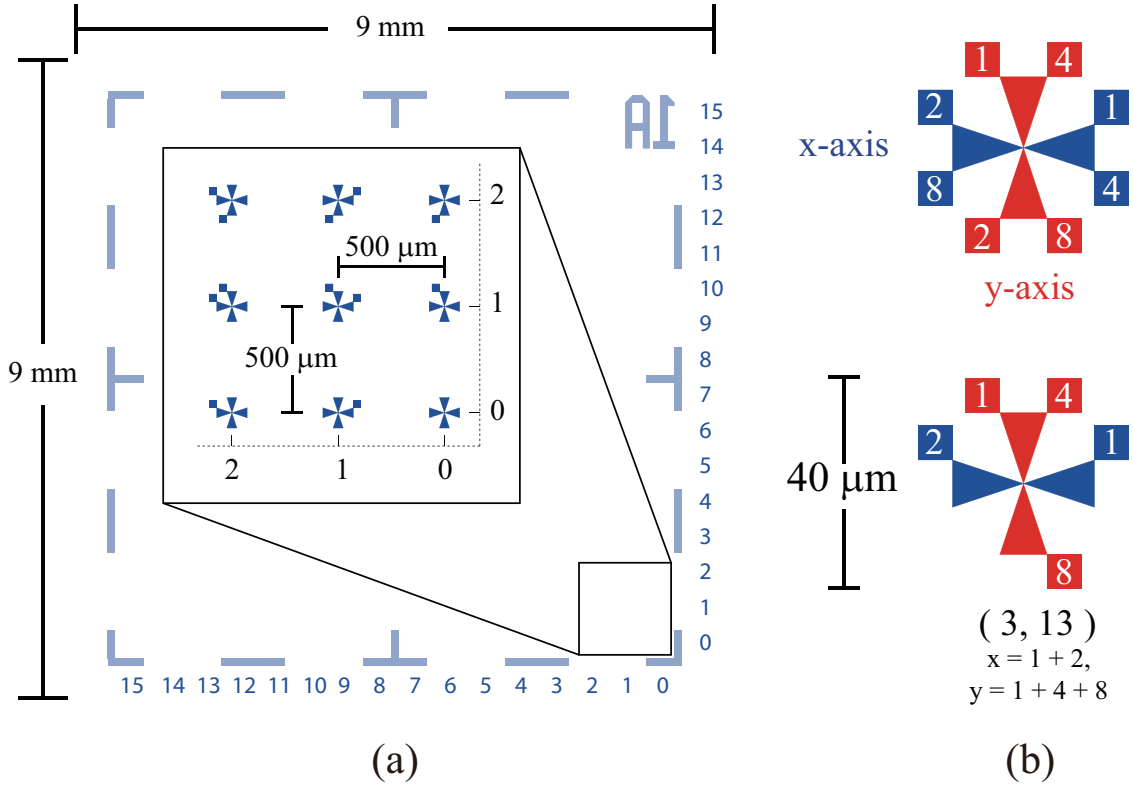

Figure 2.1: (a) Location of address markers in a substrate (9 mm × 9 mm). Separation of adjacent address markers is 500 μm and each address marker has different shape so that one can know its position from the shape. (b) In each address marker, the horizontal (x) and vertical (y) coordinates of its position are known from the position of dots. Each dot indicates 1, 2, 4, or 8 in the x or y axis, depending on its position. The sum of the numbers corresponds to the coordinate. An example is shown in (c). This address marker indicates the position (3,13).

nitrogen blow.

(4) Metal deposition and lift-off

Address markers are made from Al (5 nm) / Au (100 nm), which is thermally deposited in vacuum ($\sim 10^{-6}$ Torr). After metal deposition, we remove the photo resist and excess metal by lift-off.

(5) Hydrogen annealing

To remove residual photo resist, we perform the hydrogen annealing at 300 degrees for 1 hour in argon-hydrogen mixed gas.

2.1.2 Scotch tape method

For production of the high quality graphene, Scotch tape method is commonly used. This method take advantage of a graphene's property that the interlayer coupling is weaker than the in-plane coupling. By using this method, we obtain single layer graphene with lateral sizes < 0.1 mm on a Si substrate. The following is the procedure of the Scotch tape method:

(1) Place a few graphite flakes on the adhesive side of a plastic sticky tape. We use Kish graphite (Toshiba ceramics Co. AP70 PV KISH GRAPHITE TYPE B).

(2) Sandwich the graphite flakes between adhesive sides, and slowly peel the tape. Exfoliated graphite flakes are attached on both adhesive sides.


(3) Repeat this process until exfoliated graphite flakes are spread over adhesive sides.

(4) Attach the adhesive side with graphite flakes on a Si substrate with address markers, and gently rub the surface of the tape.

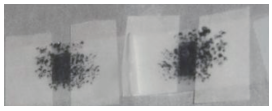
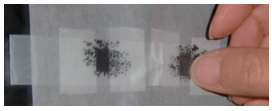

(5) Slowly peel the tape off the substrate.

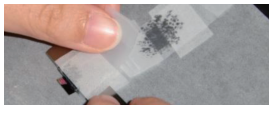
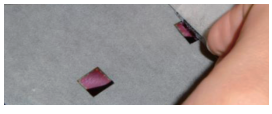

(6) After peeling, not only graphite flakes but also adhesive remain on the substrate. The adhesive can be removed by putting the Si substrate into acetone for an hour.

2.1.3 Estimation of the number of graphene layers

We use optical images to estimate the number of graphene layers. It is known that difference of the number of graphene layers can be detectable in optical images when graphene is placed on a Si substrate with SiO_2 layer of $\sim 300\mu$m. Figure 2.2(a) is an optical image of graphene flakes placed on a Si substrate. Graphite flake looks darker with increasing the number of graphene layers. In the case of substrate coated with LOR resist, by using this technique, we also canfind single layer graphene as shown in Fig 2.2(b).

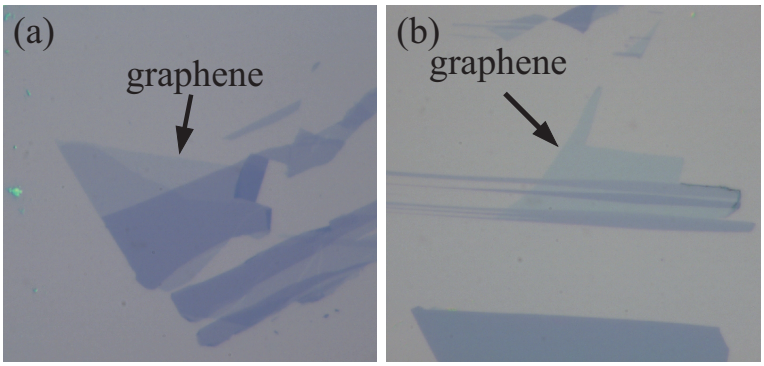

Figure 2.2: Optical images of graphene on a SiO_2 (300 nm)/Si substrate (a) and on a SiO_2 (300 nm)/Si substrate coated with LOR 1A resist (b).

2.1.4 Fabrication of small address markers

To determine the position of a graphene film more accurately, we fabricate small address markers which allows one to identify the position of graphene with ∼100 nm accuracy.

(1) Pattern design

First, we take a picture of a region which includes graphene films and two adjacent markers (Fig. 2.3(a)). Then, by using graphic software, we design a pattern for small address markers as shown in Fig. 2.3(b). Figure 2.3(c) shows the shape of a small address marker.

(2) Spin-coat of e-beam resists

We use two kinds of e-beam resists, NANO MMA(8.5)MAA EL9 and NANO 950 PMMA A5. First, we spin-coat the former resist at 500 rpm (5 sec.) followed by 3000 rpm (60 sec). Then the substrate is heated on a hotplate at 180 degrees for 10 minutes. Next, we spin-coat the latter resist with the same condition. Finally, the substrate is heated at 180 degrees for 20 minutes.

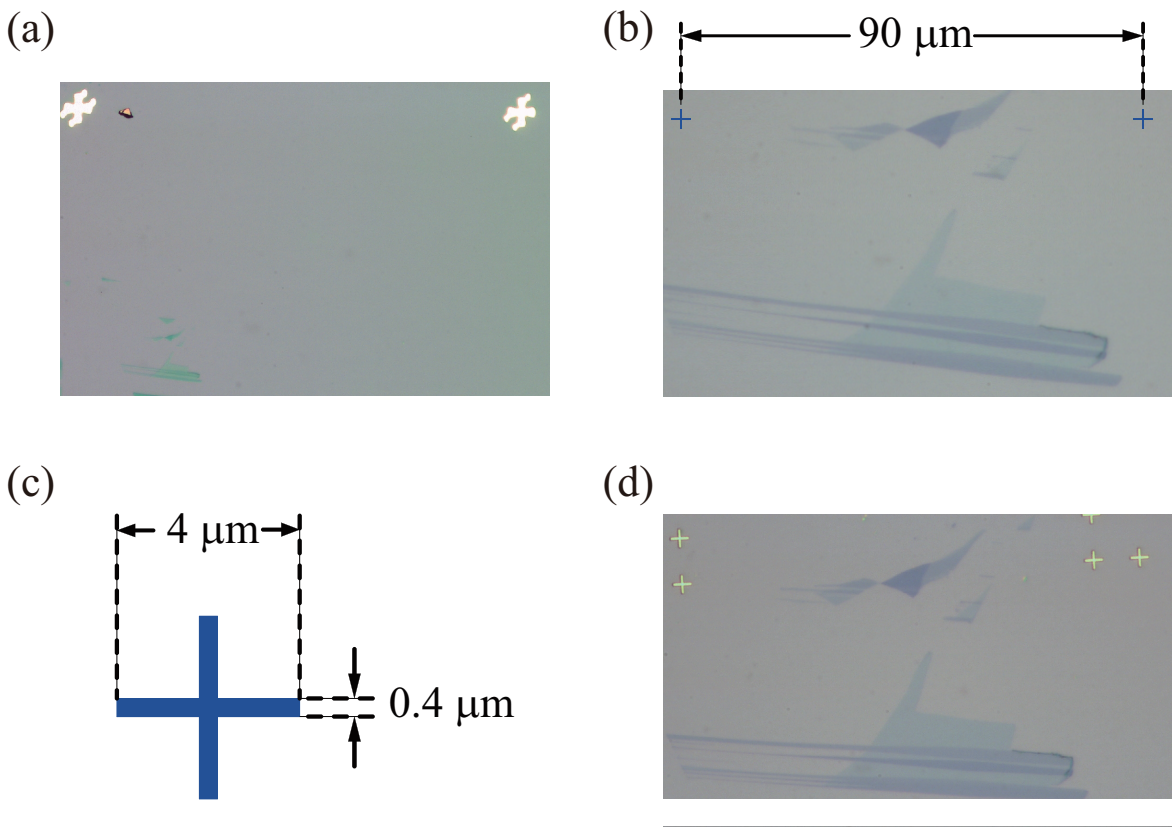

Figure 2.3: Optical images of markers: (a) adjacent markers with graphene, (b) small address markers placed near graphene, (c) size of a small address maker, (d) whole view of small markers around graphene.

(3) E-beam exposure and development

The pattern of the small address markers is transferred to the substrate with e-beam exposure of $250-300\ \mu C/cm^2$. The e-beam lithography machine is ELIONIX ELS 7700 with the acceleration voltage of 50 kV. After the exposure, the substrate is dipped in OEBR1000 developer (Tokyo Ohka Co.) (20 sec.), IPA (30 sec.), mixture of IPA and ethanol (1:1) (60 sec.) and IPA (30 sec.), in this order. Finally, the substrate is dried with nitrogen blow.

(4) Metal deposition and lift-off

Small address markers are made from Al (5 nm) / Au (100 nm), which is thermally deposited in vacuum ($\sim 10^{-6}$ Torr). After metal deposition, we remove the photo resist and excess metal by liftoff technique.

2.1.5 Oxygen plasma etching

Oxygen plasma etching is commonly used for trimming graphene in a desired shape. First, a substrate with graphene is coated with e-beam resist ZEP-520 at 500 rpm (5 sec) followed by 3000 rpm (60 sec). Then, the substrate is heated on a hotplate at 180 degrees for 2 hours. Next, a pattern of the area to be removed (Fig. 2.4 (a)) is transferred with e-beam exposure with $\sim 150\mu C/cm^2$. Development is performed in ZEP-N50 for 10 sec, followed by rinse in IPA for 10 sec and nitrogen blow. Oxygen plasma etching is performed at power of 50 W in 200 mPa of O_2 for 30 sec. Then, the substrate is put in n-methylpyrrolidone for 4 hours for the removal of the resist. Figure 2.4 (a) and (b) shows a graphene film before and after oxygen plasma etching, respectively.

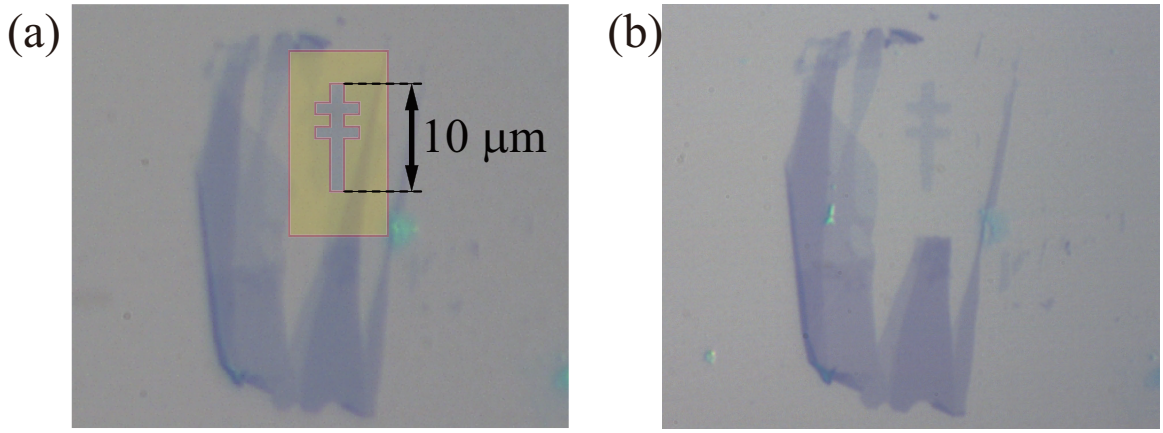

Figure 2.4: A graphene film before (a) and after (b) oxygen plasma etching. In (a), yellow region indicates the resist pattern.

2.1.6 Fabrication of electrodes for transport measurement

Electrodes for transport measurement are fabricated by using the same technique for fabrication of small address markers.

2.2 Raman spectroscopy

We perform Micro Raman spectroscopy (mapping) to estimate the graphene thickness, the amount of strain, and the defect density. The Raman system is Nanophoton RAMANplus. The excitation laser wavelength is 532 nm, the excitation power is 0.1 mW for the linear illumination mode, and the spot size is ~ 0.5 μm.

We obtain the wave number, intensity and width of a peak in Raman spectra by fitting the

peak with a Lorenzian curve,

$$f(x) = \frac{I}{1 + \left(\frac{x - x_0}{\gamma}\right)^2},$$

where I is the intensity, x_0 is the peak wave number, and 2γ is the full width at half maximum.

2.3 Transport measurement

We perform transport measurement at room temperature in vacuum or in the air using a probing station. For four-terminal measurements, a sample is connected to instruments shown in Fig. 2.5. For the gate voltage dependence measurements, the highly doped Si substrate is used as a back gate, which is connected to a voltage source (Keithley 230). Instruments are controlled by Labview (NATIONAL INSTRUMENTS).

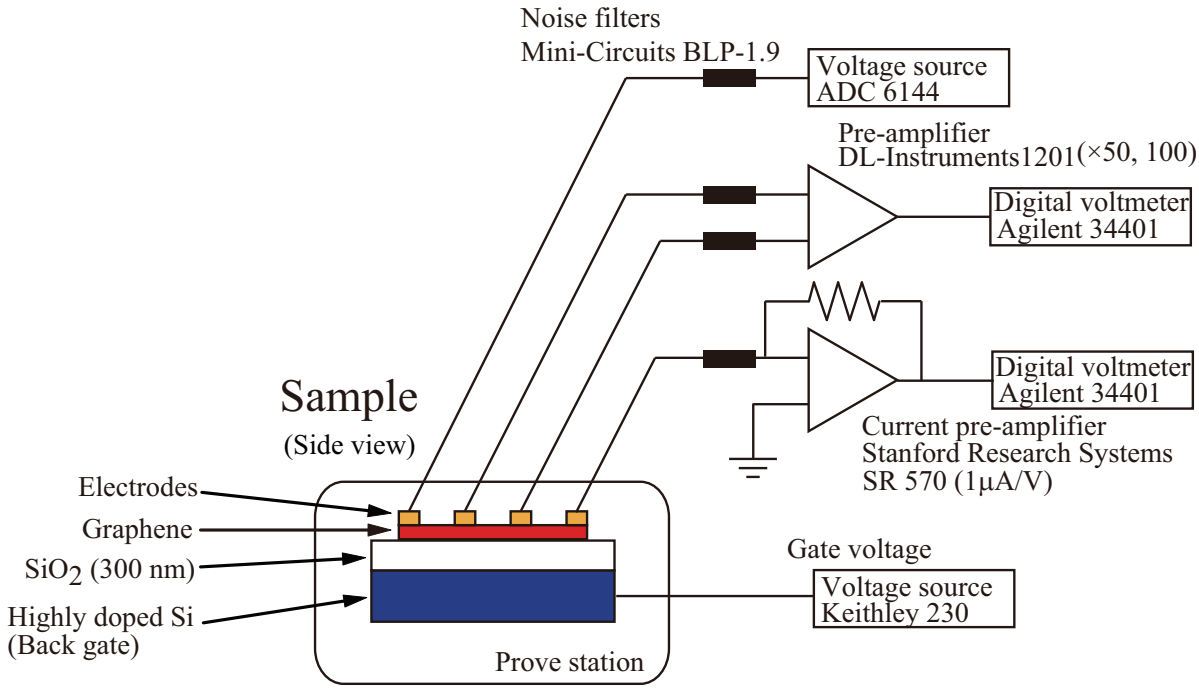

Figure 2.5: Experimental setup for the four-terminal transport measurement.

Chapter 3

Effect of local lattice strain on electron transport in graphene

Due to the two-dimensional hexagonal lattice structure, lattice strain in graphene produces an effective vector potential for charge carriers. While it is expected that one can control the electron transport in graphene by tailoring the local lattice strain, the absence of the technique to induce designed local lattice strain hampers development of strain science and engineering of graphene.

Here, we develop, for the first time, a method of introducing designed local lattice strain to graphene, and study experimentally the effect of local lattice strain on the graphene electron transport.

3.1 Inducing designed local strain in graphene

To induce designed local strain in graphene, we use nanostructures made of a dielectric material (electron beam resist) placed between a graphene film and the Si substrate. For the fabrication of nanostructures on the surface of a Si substrate, we take advantage of an uncommon property of e-beam resists: excess exposure to e-beam makes resists such as lift-off resist (LOR) and polymethyl methacrylate (PMMA) insoluble even in their developers and removers.[1]

3.1.1 Procedure of inducing designed local strain in graphene

(1) Preparing a graphene film on a Si substrate covered with e-beam resist LOR

First, we spin-coat a Si substrate with LOR -1A resist (Micro Chem) with 500 rpm (5 sec) followed by 2500 rpm (60 sec). The thickness of LOR resist is $100 - 150$ nm. Then, graphene films are mechanically extracted from kish graphite by Scotch tape method and are placed on the substrate (Fig. 3.1(a)). The graphene thickness is estimated by optical microscopy. After this process, if necessary, we fabricate electrodes by e-beam lithography with the PMMA resist, metal deposition and lift-off. We note that the bottom LOR resist is not damaged by developers and removers of the top PMMA resist.

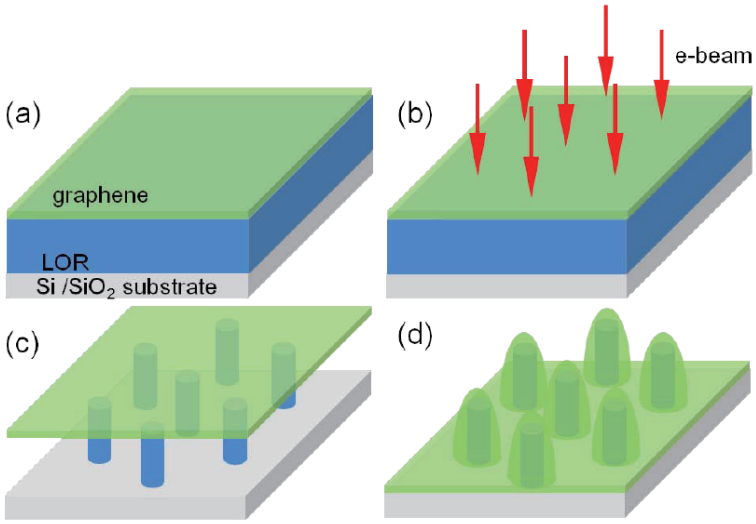

Figure 3.1: Sample fabrication procedures. (a) Graphene is placed on Si substrate coated with e-beam resist LOR. (b) Pattern for resist nanostructures is transferred with excess e-beam exposure. (c) Resist without excess e-beam exposure is removed. (d) After dipping the substrate into water, graphene is attached the Si substrate.

(2) Excess e-beam exposure

The pattern for the resist nanostructures is transferred to the LOR resist with an e-beam dose of 60,000 μC/cm^2, which is more than 100 times larger than that of the normal exposure (Fig. 3.1(b)).

(3) Removal of the LOR resist

Next, we remove the LOR resist without the excess e-beam exposure by dipping the substrate in the remover, N-methyl-2-pyrrolidone, for 5 min, rinse it with 2-propanol for 30 sec, and then put the substrate into distilled water for 30 sec. Finally, we dry the substrate with nitrogen blow (Fig. 3.1(c,d)).

If we skip the dip into distilled water, the graphene film is suspended over the LOR nanostructures as shown in Fig. 3.2. On the other hand, a graphene film after dipped into distilled water is attached to the substrate, as shown in Fig. 3.3, indicating that the graphene film is nonuniformly strained.

3.1.2 Estimation of the amount of strain in graphene

Scanning electron micrographs

We develop a method of estimating the amount of strain from scanning electron microscopy (SEM) images. For this purpose, we place additional PMMA disks on top of the LOR nanostructures. We

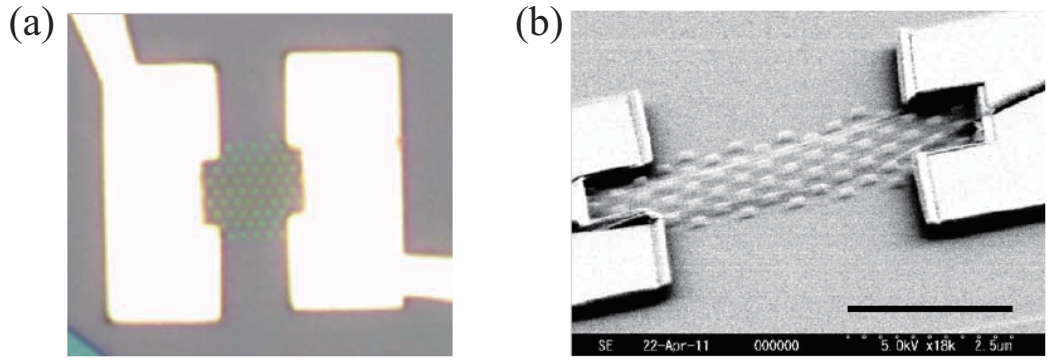

Figure 3.2: SEM images of suspended graphene: (a) top view, (b) oblique view.

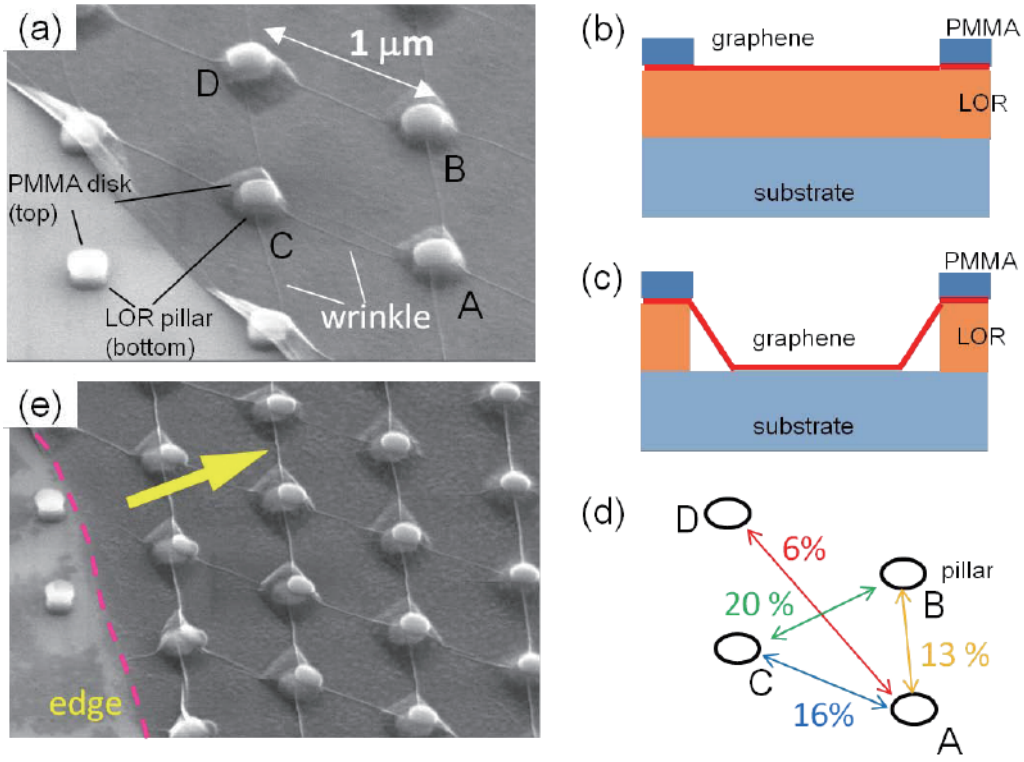

Figure 3.3: (a)SEM image of a graphene without lateral shift. (b)(c) Schematic side view of the sample before (b) and after (c) the LOR removal without the lateral shift of graphene. The graphene section between pillars stretches to attach to the substrate. From this model, one can estimate the average stretch between pillars. The result for image (a) is shown in (d). (e) SEM image of graphene with noticeable lateral shift. Dashed line and arrow indicate an edge of graphene and the shift direction, respectively.

make them by coating the substrate with thin PMMA after the deposition of graphene, followed by exposure of it to excess e-beam. Figure 3.3 shows SEM images of such samples, in which

nanopillars with triangular symmetry are formed. In Fig, 3.3(a), each PMMA disk is exactly on top of the corresponding LOR pillar, indicating that the graphene did not shift laterally when stretching, as illustrated in Fig, 3.3(b) and 3.3(c). The average stretch is defined as the increase of the length of a graphene section between a pair of pillars after the stretch divided by the original graphene length (separation of the pillars). From Fig. 3.3(a), one can estimate the average stretch of graphene between pillars, which ranges from 6 to 20%, depending on the direction, as shown in Fig. 3.3(d), in which pillars A to D correspond to those in Fig. 3.3(a). The absence of the triangular symmetry in the average stretch is presumably because of a minimal lateral shift of graphene, which is undetectable by the present method. This shift also causes wrinkles in Fig. 3.3(a). Figure 3.3(e) shows another example, in which the top PMMA disks are shifted in the direction perpendicular to the graphene edge (indicated by a dashed line). The amount of the shift becomes larger as pillars approach the graphene edge. Even in this case, though, the graphene film stretches along the shift direction with an average stretch of 7%, as estimated from the SEM image.

Micro-Raman spectroscopy

To confirm the strain in graphene, we also performed spatially resolved micro-Raman spectroscopy. The Raman spectra were acquired using a laser excitation of 532 nm (2.33 eV) with an incident power of 100 μW and a spot size of ~ 0.5 μm. The result is shown in Fig. 3.4. Figure 3.4(a) is an SEM image of the sample, in which a triangular lattice of LOR pillars 130 nm high and 200 nm wide is placed underneath graphene. The separation of pillars is 1.5 μm. The average stretch of graphene between adjacent pillars is estimated to be $\sim 6-9\%$ from SEM images, depending on the direction. Figure 3.4(b) shows the spatial distribution of the Raman signal in the area indicated by a yellow square in Fig. 3.4(a). Here, the average signal intensity between 2665 and 2675 cm^{-1} is plotted in a gray scale. White (black) regions mean high (low) Raman intensity. It is clear that the spatial variation of the Raman signal corresponds to the triangular lattice of pillars, indicated by red circles in Fig. 3.4(b).

To see this in more detail, we look at the Raman spectrum at several points, A_1, A_2, B_1,$\cdots$, E_2, indicated in Fig. 3.4(c). Here, A_i ($i = 1, 2$) is on a pillar and B_i to D_i are located near the midpoint of adjacent pillars. Points X_1 and X_2 ($X = A$,$\cdots$, D) are equivalent in the triangular lattice. E_1 and E_2 are near the graphene edge. The Raman spectra of these points around the 2D band are shown in Figs. 3.4(d) - 3.4(f). On the pillars (Fig. 3.4(d)), the 2D peak is located at (2663 ± 1) cm^{-1}, which downshifts in comparison with the value of ~ 2680 cm^{-1} for graphene placed on a Si substrate (without pillars),[2, 3] as shown in Fig. 3.4(g). Note that the LOR pillars (without graphene) do not show any Raman peak around the 2D band. On the other hand, near the midpoint of adjacent pillars (Fig. 3.4(e)), the spectrum is almost independent of the direction within the accuracy of the measurement, and exhibits a maximum at (2670 ± 2) cm^{-1}. The difference of the 2D peak positions in Figs. 3.4(d), 3.4(e), and 3.4(g) presumably originates from the variation of

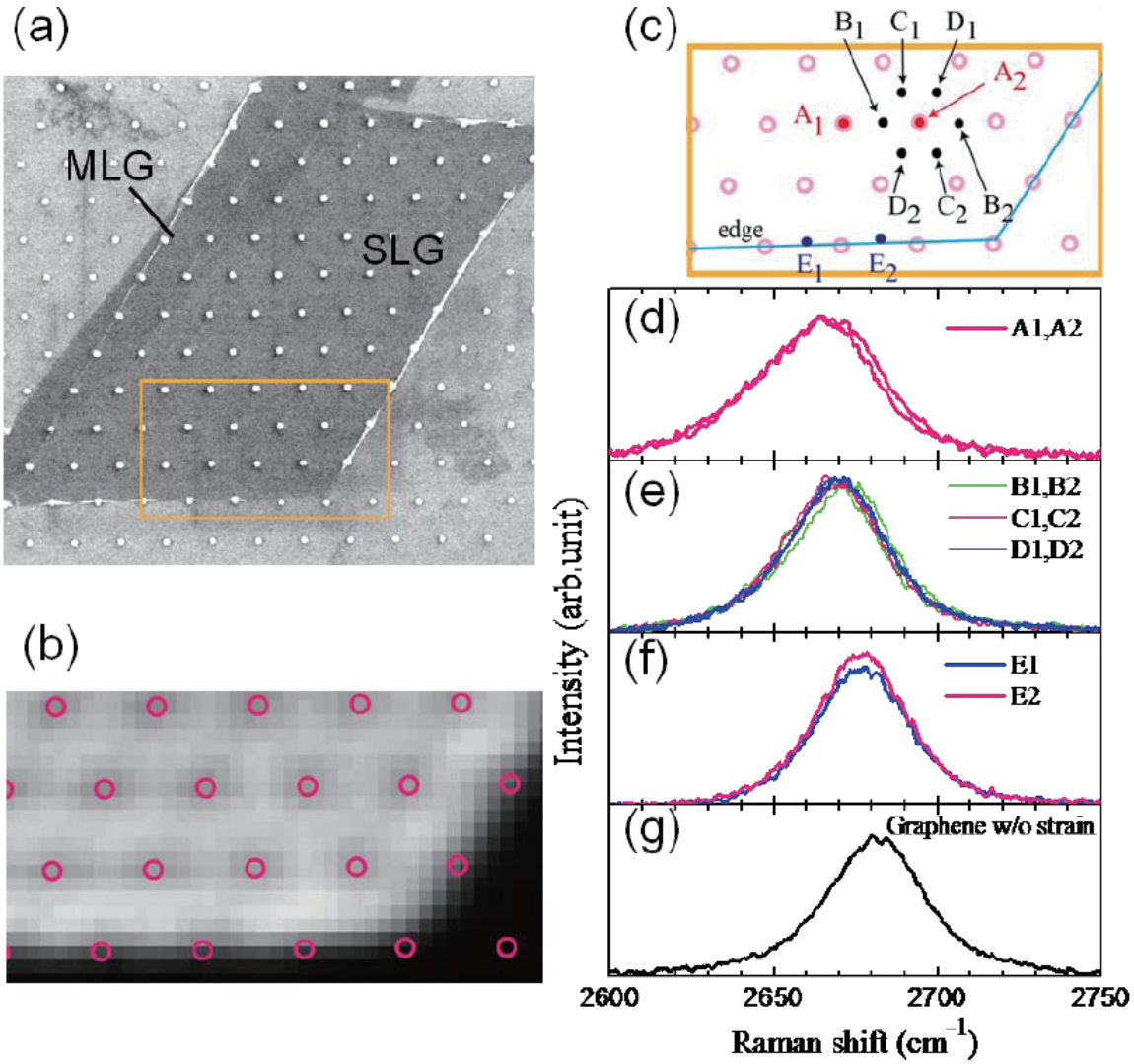

Figure 3.4: (a) SEM image of a graphene with LOR pillars. (b) The spatial distribution of the Raman signal in the area indicated by a yellow square in (a). (c) Schematic of the sample. (d-g) Raman spectra around 2D band are shown (d) for graphene on pillars, (e) for graphene near the midpoint of adjacent pillars, and (f) for graphene near an edge. Positions for each spectrum are indicated in (c). (g) Typical Raman spectrum for graphene without strain.

strain. Actually, near a graphene edge, where one can expect a relaxation of strain due to the existence of the edge, a smaller downshift is observed as shown in Fig. 3.4(f), in which the 2D peak is situated at (2667 ± 1) cm^{-1}.

In Ref. [4], the 2D band is reported to downshift linearly with uniaxial strain in graphene. The amount of downshift is ~ 20 cm^{-1} for 1% strain, which seems to be much larger than our results for nonuniaxial strain. One of possible origins of the discrepancy is an influence of excess e-beam exposure. More experiments as well as theoretical investigations are needed for quantitative

understanding of our results.

We also note that the shift of the 2D band is also caused by the spatial variation of the gate-induced carrier density due to the change of the gate capacitance, but the amount of the downshift is too large to be explained solely by the carrier density variation. Actually, according to Fig. 1.10,[5] the shift of 2D band seen in Fig. 3.4 corresponds to the carrier density variation of more than 4×10^{16} m^{-2}, which can be produced by the gate voltage larger than 150 V. It is not likely that such a large voltage is applied spontaneously to the substrate.

These results show that one can control the local lattice strain by designing the positions and sizes of resist nanostructures.

3.1.3 Graphene device with one-dimensional local strain with electrodes for transport measurement

In the following, we deal with one-dimensional local strain for the study of strain effect on electron transport properties of graphene. The reason why we do not use two-dimensionally distributed strain such as the triangular symmetrical strain is that in a triangular symmetric strain, for example, the lattice strain does not keep the triangular symmetry at graphene edges, as shown in Fig. 3.4, which might lead to extrinsic effect on electron transport, such as nonuniform current distribution. In contrast, we expect that the one-dimensional character is not extremely broken near the edges for one-dimensional local strain.

Based on this consideration, we fabricate graphene FETs with one dimensional local strain. One dimensional local strain is realized by inserting a resist nanostructure (nanorod) between graphene and the Si substrate.

The following is the procedure of sample fabrication: First, we place a graphene film on a substrate covered with e-beam resist LOR (Fig. 3.5(a)). Then, we fabricate electrodes Cr/Au (5 nm/150 nm) for transport measurement using e-beam lithography with PMMA and lift-off (Fig. 3.5(b)). Next, the pattern for the resist nanostructure is transferred with excess e-beam exposure of 60 mC/cm^2 (Fig. 3.5(c)). After the development, the resist without excess e-beam exposure is removed, so that the graphene is attached to the substrate (Fig. 3.5(d,e)). In this process, a smallest misalignment of first and second e-beam lithography patterns causes different spatial variation of strain depending on samples, as exemplified below.[1]

Figure 3.6 is an SEM image of a sample with a resist nanorod. The height and width of the resist nanorod is ∼130 nm and ∼100 nm, respectively.

For the estimation of the amount of strain in graphene, we use Raman spectroscopy. The Raman 2D band downshifts as the strain increases, as explained above. Figure 3.7 shows a gray scale mapping of Raman 2D peak position in graphene with resist nanorods. Darker region corresponds to a 2D peak with a smaller wave number. The downshift of the 2D band around resist nanorods is

[1] Accuracy of the pattern alignment in our e-beam lithography system (ELIONIX ELS-7500) is ∼ 100 nm.

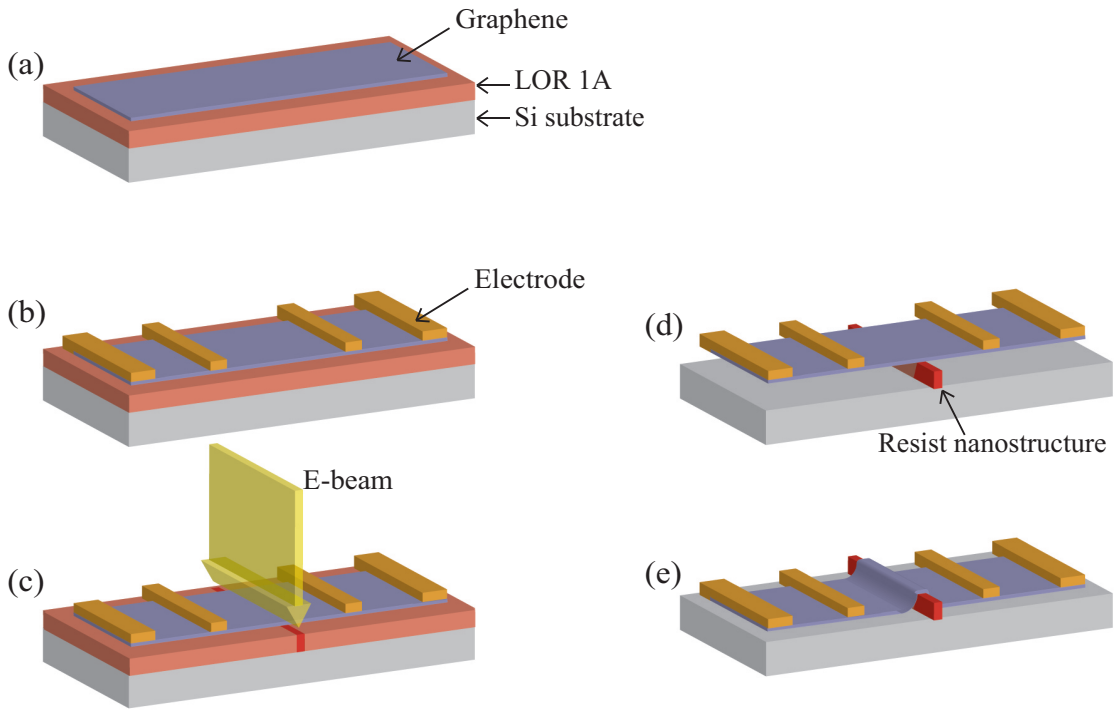

Figure 3.5: Procedure of sample fabrication. (a) Graphene is placed on a Si substrate coated with e-beam resist LOR. (b) Electrodes are fabricated by electron beam lithography and lift-off. (c) Pattern for the resist nanostructure is transferred with excess e-beam exposure. (d) After the development, resist without excess e-beam exposure is removed. (e) The graphene film is attached to the substrate.

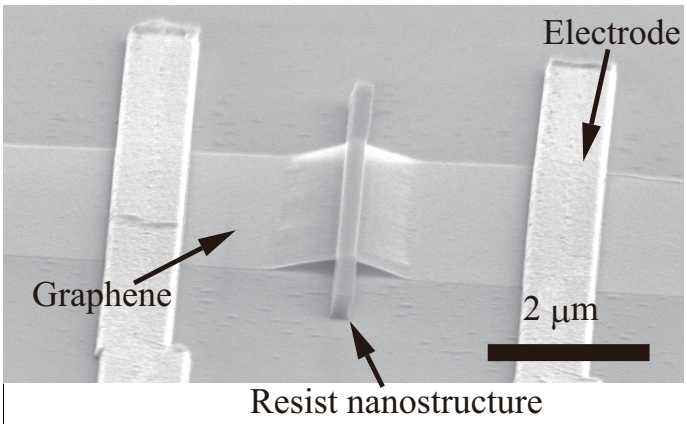

Figure 3.6: SEM image of a sample. Resist nanostructure is inserted between a graphene film and the Si substrate.

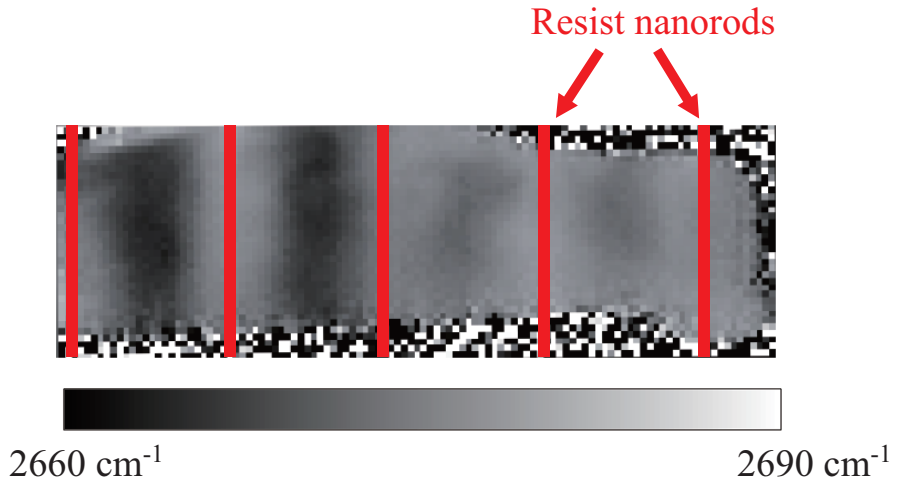

Figure 3.7: Gray scale mapping of 2D band peak position in graphene with one-dimensional resist nanostructures (nanorods). Darker region corresponds to a 2D peak with smaller wave number.

smaller than that at the midpoint of adjacent resist nanorods. This result indicates that the strain is maximum around the midpoint of adjacent resist nanorods, and becomes smaller as approaching a resist nanorod.

This result is in sharp contrast to the strain distribution in graphene on top of resist nanopillars with triangular symmetry (Fig. 3.4). In Fig. 3.4, the strain is maximum on top of a resist nanopillar, while in Fig. 3.7, the strain takes a minimum value on top of a resist nanorod. The origin of the difference of strain distribution is not clear at this moment, and further theoretical and experimental investigations are needed on this issue.

3.2 Electron transport in graphene with one-dimensional local strain

A typical gate voltage ($V_{\rm g}$) dependence of conductivity (σ) of graphene FET devices with a resist nanorod is shown in Fig. 3.8. While the $\sigma - V_{\rm g}$ curve of conventional graphene FETs placed on a SiO_2/Si substrate (without a resist nanorod) exhibits a V-shaped characteristic, as shown in Fig. 1.4, the $\sigma - V_{\rm g}$ curve of graphene FETs with a resist nanorod has the following characteristics:

1. The gate voltage, $V_{\rm D}$, corresponding to the minimum conductivity takes a large positive value, typically $\sim$ 50 V. This is presumably due to the use of LOR resist. We speculate that the residue of the LOR resist positively charges up the graphene film.

2. The $\sigma - V_{\rm g}$ curve becomes asymmetric; the field effect mobility of electrons, $\mu^{\rm e}_{\rm FE}$, is largely suppressed.

As an example of the latter characteristic, in Fig. 3.8(a), the field effect mobility of holes, $\mu_{\rm FE}^{\rm h}$, is 0.17 $\rm m^2/Vs$, while $\mu_{\rm FE}^{\rm e} = 0.063$ $\rm m^2/Vs$, and the ratio $\mu_{\rm FE}^{\rm e}/\mu_{\rm FE}^{\rm h} = 0.37$. Note that some devices exhibit a flat region at low conductivity area, as shown in Fig. 3.8(b), which indicates $\mu_{\rm FE}^{\rm e}/\mu_{\rm FE}^{\rm h} \approx 0$. Figure 3.9 shows the ratio $\mu_{\rm FE}^{\rm e}/\mu_{\rm FE}^{\rm h}$ as a function of $\mu_{\rm FE}^{\rm h}$ for all of the measured samples. Red circles, black squares and blue triangles correspond to devices with a resist nanorod, devices which do not include a resist nanorod in the current path but have nanorods in the other part of the graphene film, and devices which have no nanorod in the graphene film, respectively. Clear decrease of the $\mu_{\rm FE}^{\rm e}/\mu_{\rm FE}^{\rm h}$ ratio as well as the mobility ($\mu_{\rm FE}^{\rm h}$) degradation is seen in devices with nanorods, indicating that the asymmetry of the $\sigma - V_{\rm g}$ curve is caused by the insertion of resist nanorods. We note that the devices which do not include a resist nanorod in the current path but have nanorods in the other part of the graphene film also exhibit asymmetry. As discussed later, we believe that this is caused by the spatial distribution of strain apart from the nanorods (see Fig. 3.4).

There are three possible origins of the distorted $\sigma - V_{\rm g}$ characteristic:

- spatial variation of gate capacitance,
- excess e-beam exposure,
- local lattice strain.

To investigate in more detail the origin of the distortion, we perform the following three experiments:

1. We compare electron transport in a graphene portion with a resist nanorod and that in a graphene portion without a resist nanorod in a single graphene film.
2. We compare electron transport in a graphene portion with excess e-beam exposure and that in a graphene portion without excess e-beam exposure in a single graphene film.
3. We compare electron transport in two graphene deviecs with similar resist nanorods but with different distribution of strain.

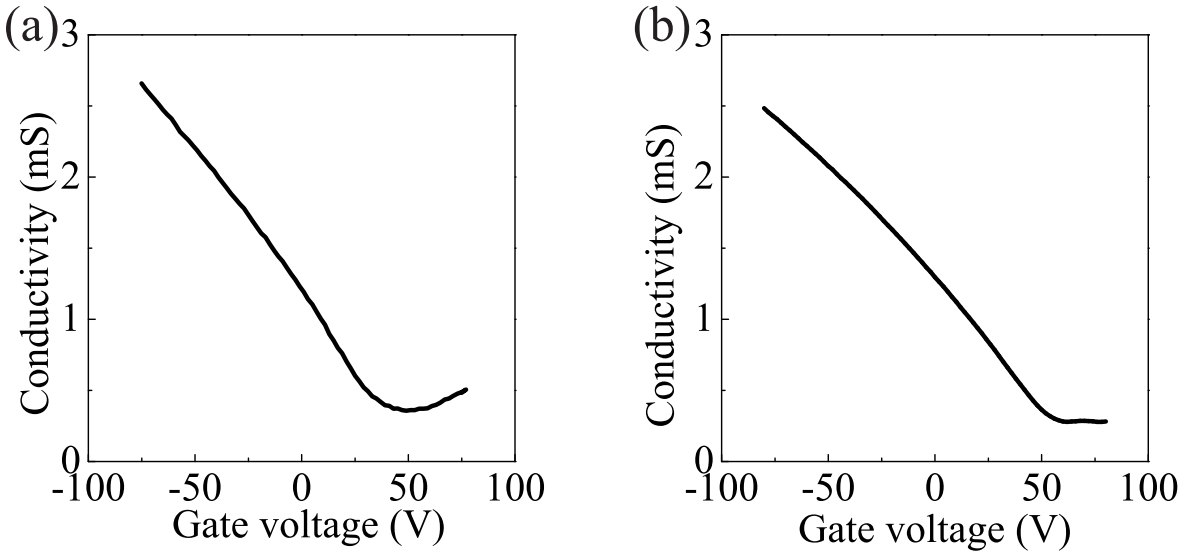

Figure 3.8: (a)(b) Conductivity as a function of the gate voltage in two graphene FETs with a resist nanorod.

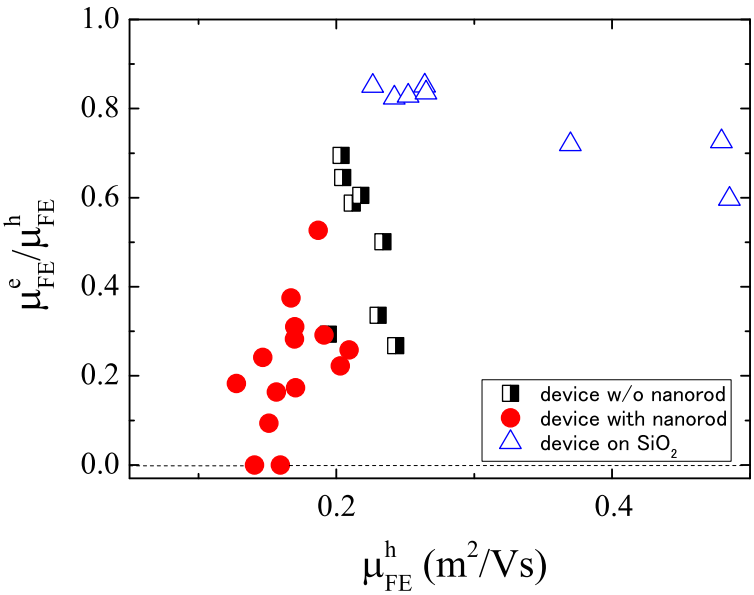

Figure 3.9: The ratio $\mu^{e}_{FE}/\mu^{h}_{FE}$ as a function of μ^{h}_{FE} for all of the measured devices. Red circles, black squares and blue triangles correspond to devices with a resist nanorod, devices which do not include a resist nanorod in the current path but have nanorods in the other part of the graphene film, and devices which have no nanorod in the graphene film, respectively.

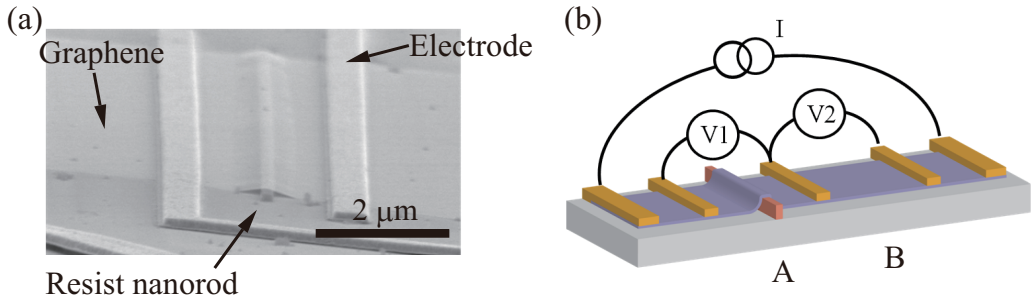

Figure 3.10: SEM image (a) and schematic (b) of the sample.

3.2.1 Experiment 1: comparison of electron transport in a device with a resist nanorod and that in a device without a resist nanorod

Sample structure

For investigation of the influence of spatial variation of gate capacitance by the resist nanorod, we compare electron transport in a device with a resist nanorod and that in a device without a resist nanorod. Both devices are made from the same graphene film. The sample structure is shown in Fig. 3.10, which includes a graphene device A with a resist nanorod (connected to a voltage lead pair V1) and a graphene device B without a resist nanorod (connected to a voltage lead pair V2) in the same graphene film. Electrodes is Cr/Au (5 nm/150 nm), and separation of voltage leads is 2 μm. From an SEM image, the average stretch of graphene portion in device A is estimated to be $\sim 2\%$.

Experimental results

We carry out four terminal transport measurement at room temperature before and after the development of the LOR resist for the formation of the resist nanorod. Figure 3.11 shows the gate voltage dependence of conductivity of device A (blue curve) and device B (red curve) before the development. Highly doped substrate is used as a back gate. We note that the excess e-beam exposure causes slight shrinkage of the LOR resist and produces a small dip with depth of 20 nm on graphene even before the development, so that the graphene portion in device A is expected to be slightly strained even before the development. As seen in Fig. 3.11, conductivity of either device A or B decreases with increasing the gate voltage. The charge neutrally point, where the conductivity takes a minimum value, is situated at a gate voltage of more than 30 V. The conductivity of device B, which is placed on a resist layer with uniform thickness, linearly decreases with increasing the gate voltage, while that of device A, which is placed on a resist layer with a small valley, exhibits a small bend.

Figure 3.12 shows the gate voltage dependence of conductivity of device A (blue curve) and

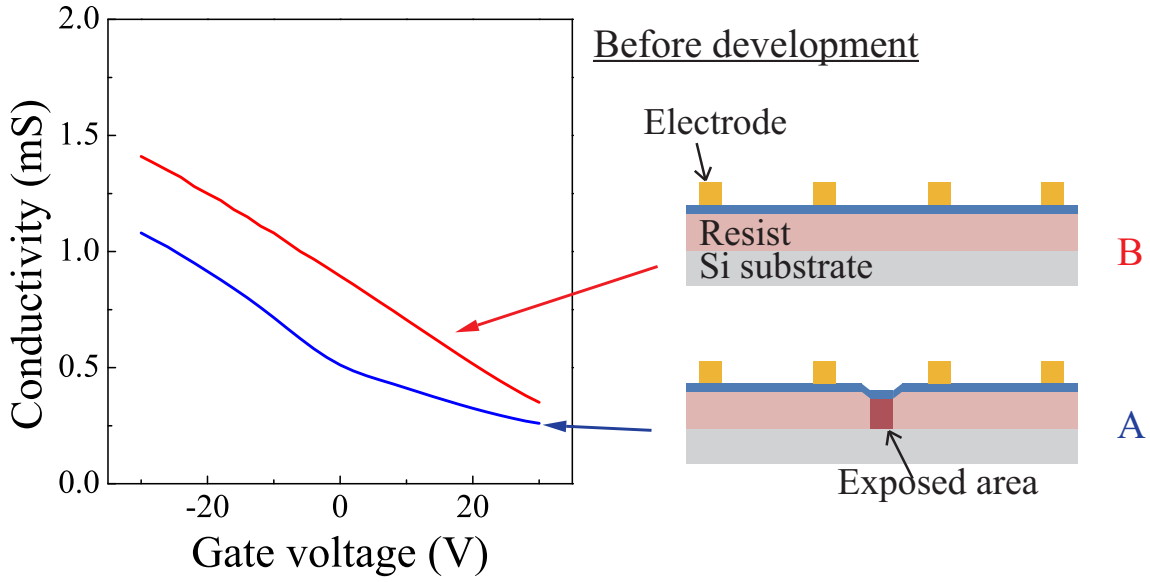

Figure 3.11: Gate voltage dependence of conductivity of device A (blue curve) and device B (red curve) before the development.

device B (red curve) after the development of the LOR resist. The conductivity of device B monotonically decreases with increasing the gate voltage. This is common to the result of device B before development, as shown in Fig. 3.11. The conductivity minimum is situated at a gate voltage larger than 30 V. On the other hand, in the conductivity of device A, a large bend (or, an nearly flat region) appears in low conductivity area. A similar behavior is seen in Fig. 3.8.

Numerical study

Here, we consider the influence of the spatial variation in gate capacitance $C_{\rm g}$ by using a numerical model, which is based on the following assumptions.

1. Local conductivity-gate voltage ($\sigma(V_{\rm g}, z) - V_{\rm g}$) curve of each part of graphene is V-shaped, which is common to graphene placed on a SiO_2 substrate (Fig. 3.13(a)).

2. Local charge neutrality point $V_{\rm g}^{\rm NP}(z)$ is determined by the surface charge density, Q_0, induced by charged impurities: $V_{\rm g}^{\rm NP}(z) = Q_0/C_{\rm g} \propto d$ where d is the thickness of the gate dielectric. The surface charge density Q_0 is assumed to be uniform over the graphene surface.

From these assumptions, we determine local conductivity $\sigma(V_{\rm g}, z)$, and calculate the whole conductivity by using the expression,

$$\sigma^{-1}(V_{\rm g}) = \frac{1}{L}\int_0^L dz \sigma^{-1}(V_{\rm g}, z)$$

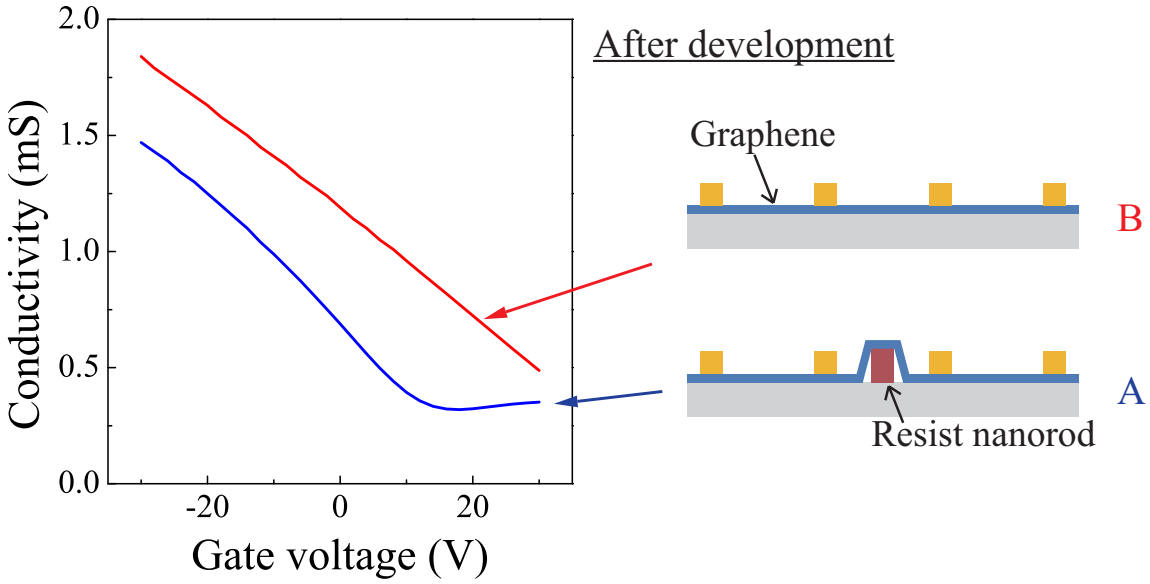

Figure 3.12: Gate voltage dependence of conductivity of device A (blue curve) and device B (red curve) after the development.

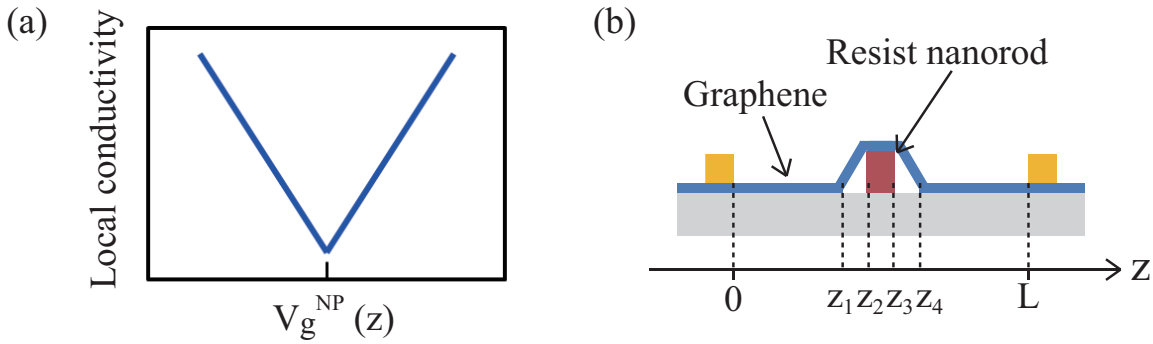

Figure 3.13: (a) Assumed gate voltage dependence of local conductivity. (b) Schematic of the sample geometry. The used lateral dimensions are $L = 2$ μm, $z_1 = 0.64$ μm, $z_2 = 0.96$ μm, $z_3 = 1.16$ μm and $z_4 = 1.49$ μm. The height of the LOR resist before and after the excess e-beam exposure are 100 nm and 81 nm, respectively.

where z is a coordinate along the current path (Fig. 3.13(b)). In the calculation, the exact lateral dimensions and height of the resist nanostructure, which are obtained from an SEM image, are taken into account (see the caption of Fig. 3.13).

(1) Before the development of LOR

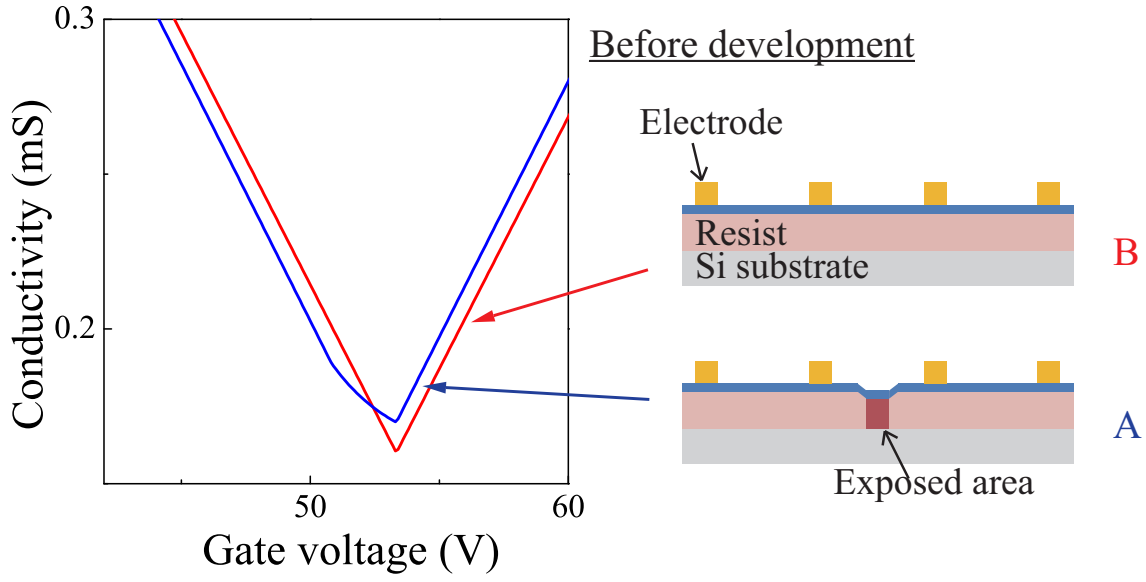

Figure 3.14: The calculated $\sigma - V_{\rm g}$ curves for device A (blue curve) and device B (red curve) before the development.

The calculated $\sigma - V_g$ curves for devices A and B before the development are shown in Fig. 3.14. Blue and red curves correspond to devices A and B, respectively. Conductivity minimum appears at the same gate voltage in two curves. In the case of graphene on a resist layer with uniform thickness (device B), the conductivity exhibits V-shaped characteristic. On the other hand, in the case of a resist layer with a valley (device A), a small kink appears at smaller gate voltage than charge neutrally point of device B. Similar behavior is observed in experimental results as shown Fig. 3.11. So, the behavior is qualitatively understandable by the change in the gate capacitance.

(2) After the development of LOR

The calculated $\sigma - V_{\rm g}$ curves for devices A and B after the development are shown in Fig. 3.15. Blue and red curves correspond to devices A and B, respectively. Again in Fig. 3.15, the conductivity minimum appears at the same gate voltage, because the most part of graphene is attached to SiO_2 in both devices. Device B exhibits a V-shaped characteristic. On the other hand, in the case of graphene placed on a substrate with a resist nanostructure (device A), the $\sigma - V_{\rm g}$ curve bends at a gate voltage larger than that of the conductivity minimum. Note that the position of the kink (bend) with respect to the conductivity minimum is different in Figs. 3.14 and 3.15, because the sign of the curvature of graphene around the exposed area is different, namely, the graphene around the exposed area is concave (convex) before (after) the development of LOR. In the experimental result, on the other hand, a kink (bend) appears at a gate voltage which is smaller

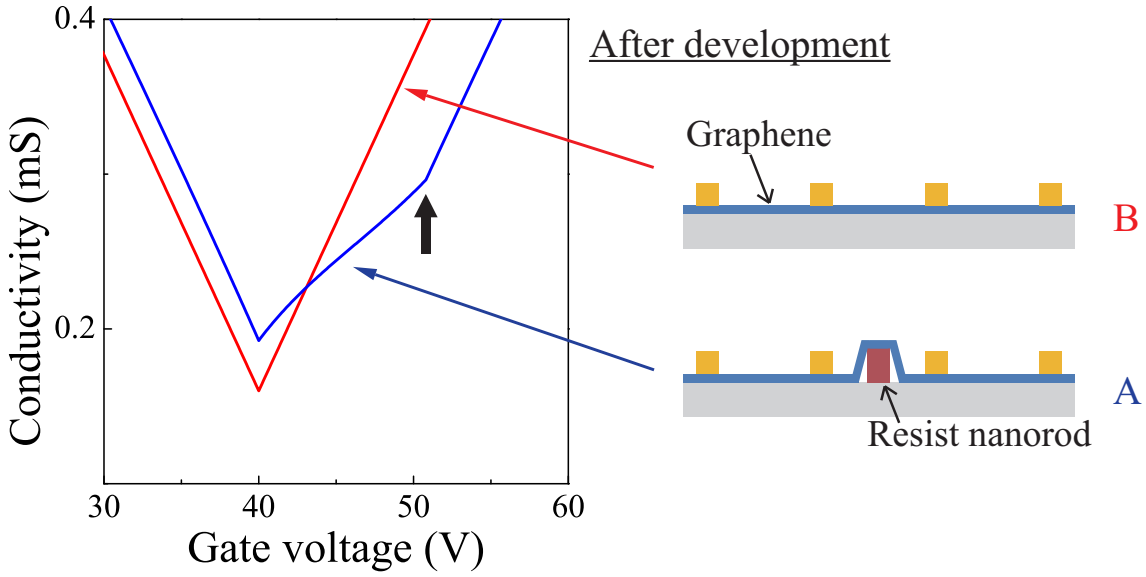

Figure 3.15: The calculated $\sigma - V_g$ curves for device A (blue curve) and device B (red curve) after the development of LOR. In device A, a kink (bend) appears at a gate voltage which is larger than that of the conductivity minimum.

than that of the conductivity minimum of device B both before and after the development. This result indicates that the difference in devices A and B cannot be explained solely as an effect of the change in the gate capacitance.

3.2.2 Experiment 2: comparison of electron transport in a device with excess e-beam exposure and that in a device without excess e-beam exposure

Sample structure

For investigation of the influence of excess e-beam exposure on graphene electron transport, we use a sample shown in Fig. 3.16(a), in which five four-terminal devices (device α – device ε) are connected in series. The graphene is placed on a highly-doped Si substrate covered with 300 nm SiO_2, which is used as a back gate. The graphene portion in devices α and β (red area in Fig. 3.16(a)) is exposed to e-beam of 50 kV several times.

Experimental results

We carry out four-terminal transport measurement at room temperature. Fig. 3.16(b) shows the gate voltage dependence of conductivity for each device after the e-beam exposure of 60 mC/cm^2. All curves exhibit V-shaped characteristic, and the minimum conductivity of each curve appears at a similar gate voltage of $\sim$ 10 V (Fig. 3.16(d)), although the e-beam exposure significantly

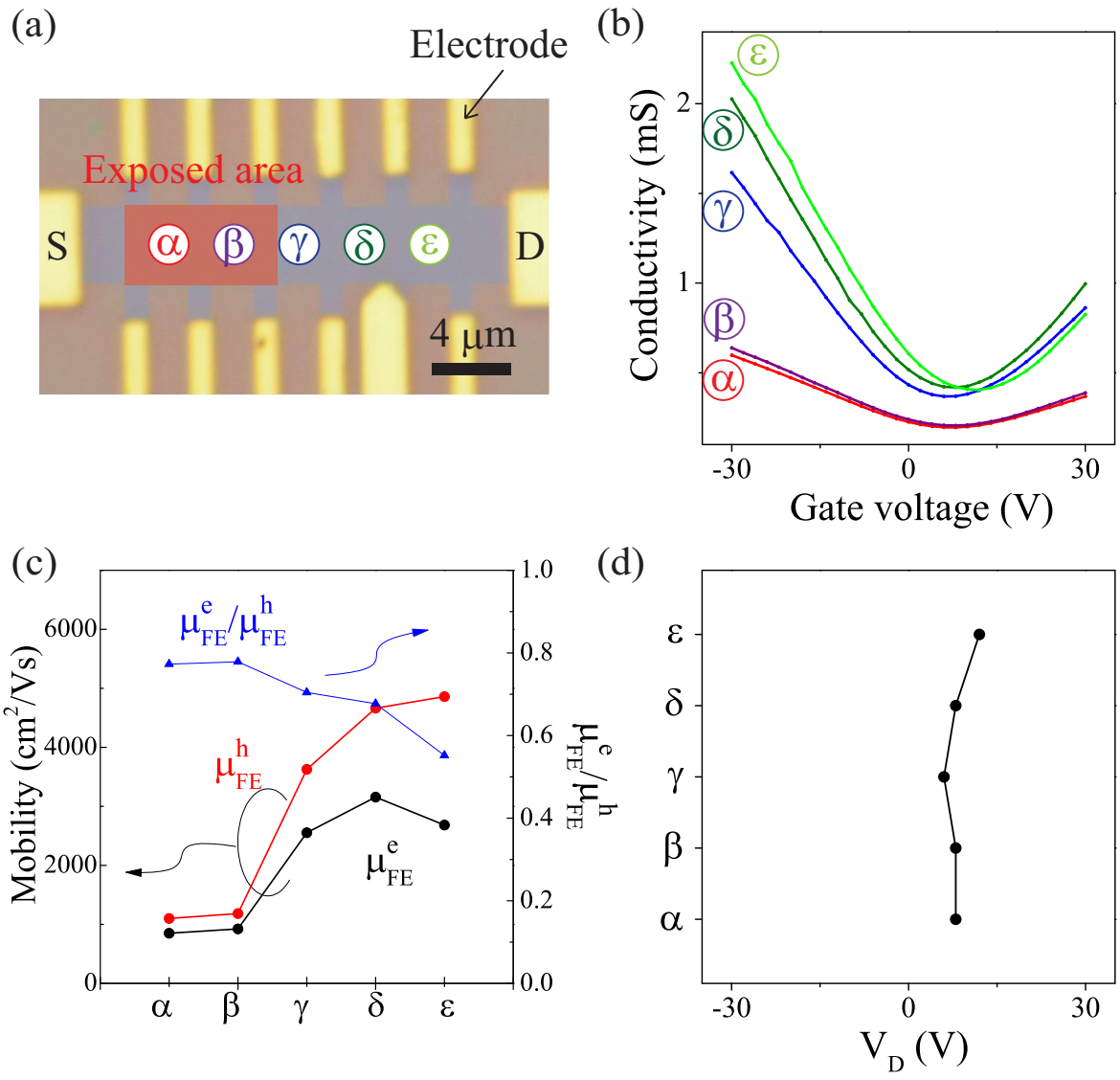

Figure 3.16: (a) Optical image of the sample. Five four-terminal devices (device α – device ε) are connected in series. Red region indicates the e-beam exposed area. (b) Gate voltage dependence of conductivity for devices $\alpha - \varepsilon$. (c) The field effect mobility $\mu^{\mathrm{e}}_{\mathrm{FE}}$, $\mu^{\mathrm{h}}_{\mathrm{FE}}$, and their ratio $\mu^{\mathrm{e}}_{\mathrm{FE}}/\mu^{\mathrm{h}}_{\mathrm{FE}}$ for devices $\alpha - \varepsilon$. (d) The charge neutrality point (Dirac point) for devices $\alpha - \varepsilon$.

degrades the mobility of devices α and β, as shown in Fig. 3.16(c). We note that these results exclude the possibility that the excess e-beam exposure locally charges up the graphene film and shifts the local Dirac point, leading to largely asymmetric $\sigma - V_{\mathrm{g}}$ characteristic, as shown in Fig. 3.8.

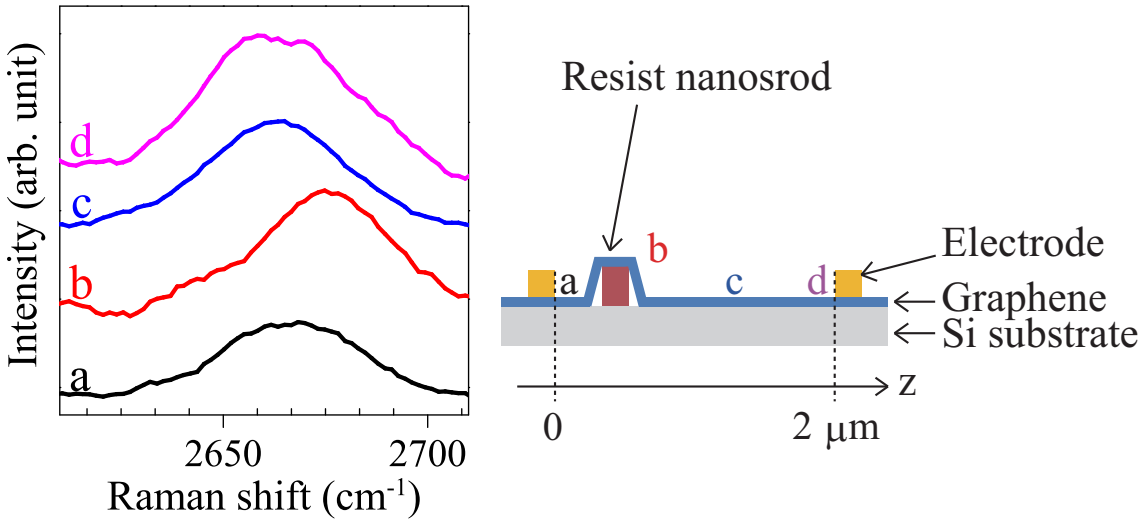

Figure 3.17: Raman spectra around the 2D band at several positions in sample 1. The curves are shifted vertically for clarity. The distances from the left electrode are a: $z = 0.1$ μm, b: $z = 0.7$ μm, c: $z = 1.5$ μm, d: $z = 1.9$ μm. The resist nanorod is situated at $z = 0.2$ μm.

3.2.3 Experiment 3: comparison of electron transport in two devices with different spatial distribution of strain

Sample structure and Raman spectra

For investigation of effect of local lattice strain on electron transport, we compare two devices, samples 1 and 2, with similar structure, as shown in Fig. 3.6, but with different distribution of strain. The different spatial distribution of strain is probably mainly caused by misalignment of the e-beam lithography pattern for the resist nanorod, the distance between the nanorod and the left electrode is 0.2 μm and 0.89 μm for samples 1 and 2, respectively.

Figures 3.17 and 3.18 show the Raman 2D band at several positions in samples 1 and 2, respectively. Each curve is obtained by averaging the local Raman spectra of the graphene portions with the same z value. (The z axis is along the current flow and perpendicular to the resist nanorod.) We note that the 2D peak wave numbers of both samples are smaller than that of unstrained graphene (~ 2680 cm^{-1}). In sample 1, the downshift of 2D band at points a, c, and d is larger than that at point b. On the other hand, in sample 2, the difference in the 2D band position is not remarkable.

Figure 3.19 summarizes the spatial variation of the 2D peak wave number of sample 1 (red dots) and sample 2 (blue dots). In sample 1, the 2D peak wave number ranges from 2662 to 2675 cm^{-1} and the maximum spatial variation is 24 cm$^{-1}/\mu$m, while in sample 2, the 2D peak wave number ranges from 2656 to 2658 cm^{-1} and the maximum spatial variation of strain is 2.5 cm$^{-1}/\mu$m. Thus, the magnitude of the strain is larger in sample 2, while the spatial variation of strain is larger in sample 1.

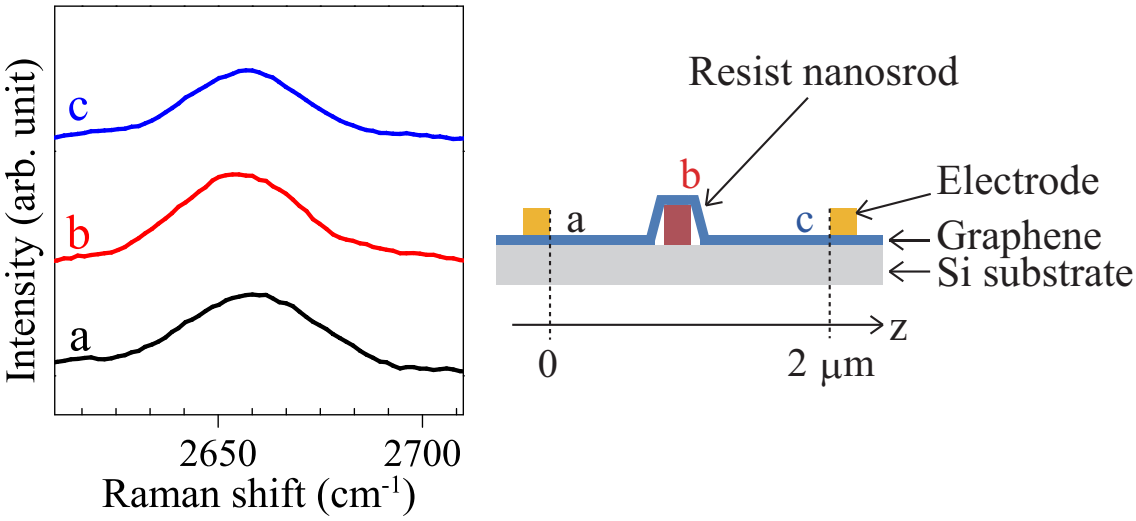

Figure 3.18: Raman spectra around the 2D band at several positions in sample 2. The curves are shifted vertically for clarity. The distances from the left electrode are a: $z = 0.14$ μm, b: $z = 1.0$ μm, c: $z = 1.86$ μm. The resist nanorod is situated at $z = 0.89$ μm.

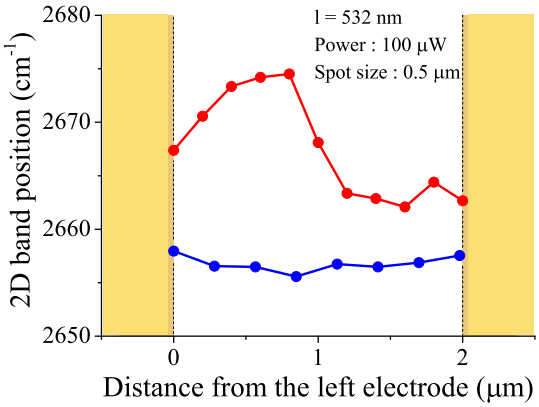

Figure 3.19: 2D peak wavenumber is plotted as a function of the distance from the left electrode in samples 1 (red) and 2 (blue).

Electrical transport

Four-terminal transport measurements are carried out for samples 1 and 2 at room temperature in vacuum. The highly-doped Si substrate is used as a back-gate, which controls the carrier density over the whole area of the graphene channel. Figures 3.20(a) and 3.20(b) show the gate voltage dependence of conductivity in samples 1 and 2, respectively. In sample 1, $\mu^{\rm h}_{\rm FE}$ is 0.16 m^2/Vs, while a flat region appears at low conductivity area at positively large gate voltage, giving $\mu^{\rm e}_{\rm FE}/\mu^{\rm h}_{\rm FE} \approx 0$. On the other hand, in sample 2, $\mu^{\rm h}_{\rm FE} = 0.19$ m^2/Vs and $\mu^{\rm e}_{\rm FE} = 0.056$ m^2/Vs, giving $\mu^{\rm e}_{\rm FE}/\mu^{\rm h}_{\rm FE} =$

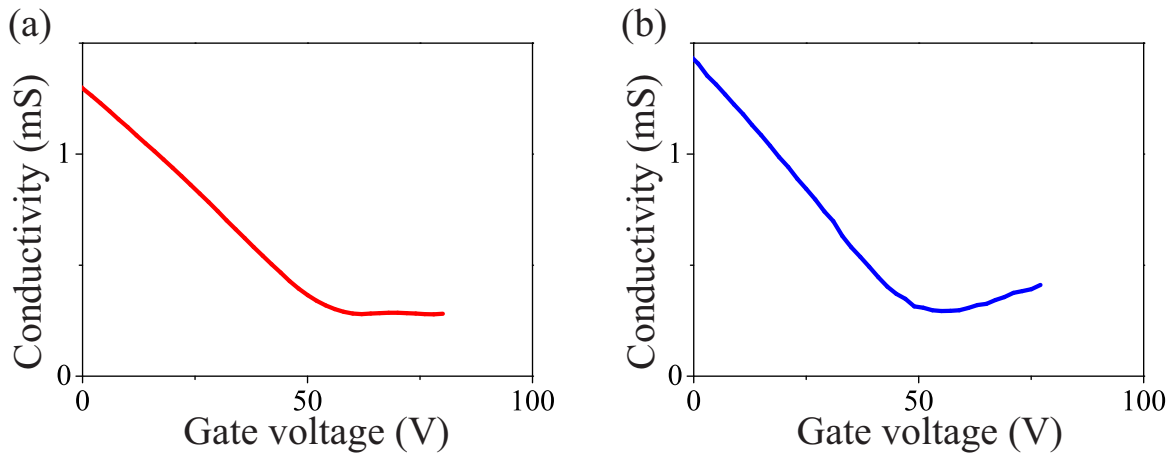

Figure 3.20: Conductivity of sample 1 (a) and sample 2 (b) as a function of gate voltage.

0.29. We speculate that larger spatial variation of strain leads to stronger asymmetry and smaller $\mu_{\mathrm{FE}}^{\mathrm{e}}/\mu_{\mathrm{FE}}^{\mathrm{h}}$.

3.2.4 Discussion

The results of experiments 1 and 2 suggest that the origin of the asymmetric $\sigma - V_{\mathrm{g}}$ curves in graphene FETs with a resist nanorod is local lattice strain, and experiment 3 indicates that the asymmetry is stronger in graphene with larger spatial variation of strain. These results strongly suggest that the one-dimensional local strain is the origin of the distortion of the $\sigma - V_{\mathrm{g}}$ curve.

In this section, we try to compare our experimental results with the theoretical prediction on the transport gap formation in one-dimensionally strained graphene.[6] Here we assume that the flat region in the $\sigma - V_{\mathrm{g}}$ curve seen in some samples (for example, in Fig. 3.8(b) and Fig. 3.20(a)) stems from the transport gap due to one-dimensional local strain with large leakage current.

First, we compare the size of the flat region with the theoretical transport gap. Both in Figs. 3.8(b) and 3.20(a), the width of the flat region is more than 20 V. From the energy dispersion relation of graphene, $\varepsilon = \hbar v_F k$, with $k = \sqrt{\pi n}$, and $v_F = 1 \times 10^6$ m/s the gate voltage width of 20 V corresponds to the energy of 0.2 eV. According to the theoretical result for the transport gap,[6] $\delta t = t_0(1 - e^{-3.37\lambda})$ with $t_0 = 2.7$ eV, the transport gap of 0.2 eV is produced by a one-dimensional strain $\lambda = 2\%$. This amount of strain is consistent with the average strain of 1% obtained from SEM images.

Next, we consider the reason for the absence of zero conductivity on the basis of the theory of one-dimensional local strain.[6] It is known that in real graphene samples, there are spatial fluctuations of the electric potential, which are induced mainly by charged impurities. Under the potential fluctuations, zero conductivity is achievable only when the transport gap is larger than

the amplitude of the potential fluctuations. Otherwise, a leakage current will be expected.

The amplitude of the potential fluctuations can be estimated from the shape of the $\sigma - V_{\mathrm{g}}$ curves. (See Section 1.1.3.) In the observed $\sigma - V_{\mathrm{g}}$ curves (for example, in Fig. 3.8(a) and Fig. 3.20(b)), the top of the curve, corresponding to the charge neutrality point V_{D}, is rounded within the gate voltage range of 20 V. From this, the amplitude of the potential fluctuations is estimated to be about 0.2 eV. This means that zero conductivity is achieved only when the transport gap is larger than 0.2 eV.

In addition, we need to take into account the spatial variation of the strain. As explained in Section 1.3.3, the theory proposed by Pereira and Neto[6] assumes abrupt change of the strain at the interface and conservation of the carrier momentum component parallel to the interface. In real graphene samples, however, strain varies slowly in space, and the elastic scattering occurs with a characteristic length of the mean free path, which is, at best, around 0.1 μm in graphene placed on SiO_2/Si. This indicates that for the observation of the perfect reflection, strain needs to change, at least, by the amount corresponding to the transport gap of 0.2 eV with the mean free path. This requires the strain change larger than 2%/0.1 μm. On the other hand, the largest spatial variation of strain of sample 1 in Fig. 3.19 is estimated to be around 0.24 %/0.1 μm,[2] which is about 8 times smaller than the theoretical requirement. Thus, we can conclude that the spatial variation is not sufficient in our samples. For the observation of the zero conductivity, increase of the mean free path, reduction of potential fluctuations and increase of the spatial variation of strain are necessary.

[2]From the lateral shift of the resist dots placed on a grapheme film, we obtained the following relationship between the strain and the Raman 2D peak position: Strain [%] = 0.093(2690− 2D peak wave number [cm^{-1}]).[7]

3.3 Effect of e-beam exposure

As explained above, the electron transport in graphene with one-dimensional local strain induced by a resist nanorod indicates that we need to increase the mean free path to observe the zero conductivity. One of the possible origins of the short mean free path is the excess e-beam exposure; our method includes an e-beam exposure as large as 60 mC/cm^2 on the current path for forming resist nanostructures. This process may induce defects in the graphene sheet, which should have a great influence on the transport property. Here, we investigate the effect of e-beam exposure on electron transport.

Sample

The sample is the same as that for experiment 2 in Section 3.2.2, which is fabricated by micromechanical exfoliation of kish graphite onto a highly-doped Si substrate covered with 300 nm SiO_2. An optical image of the sample is shown in Fig. 3.16(a). The device was exposed to electron beam of 50 keV several times. The exposed area is a part of graphene sheet, shown in Fig. 3.16(a). After each exposure, Raman and transport measurement are carried out. The Si substrate is used as a back gate. The dosage of e-beam varies from 0 to 60 mC/cm^2. From the conductivity, we derived the mobility and electron mean free path as a function of the gate-induced carrier density, n.

Experimental results

Figure 3.21(a) shows Raman spectra of a graphene portion exposed to e-beam(device α in Fig. 3.16(a)). With the increase of e-beam dose, the Raman D band situated at ~ 1350 cm^{-1} develops, and the intensity ratio of Raman D to G peaks ($I_{\rm D}/I_{\rm G}$) increases, as shown in Fig. 3.21(b), indicating the increase in the defect density.

Figure 3.22(a) is the gate-induced carrier density dependence of conductivity of device α for several e-beam doses. The gate-induced carrier density is defined as $n = C_{\rm g}(V_{\rm g} - V_{\rm D})/e$, where $C_{\rm g}$ is the gate capacitance per unit area, $V_{\rm g}$ is the gate voltage, and $V_{\rm D}$ is the gate voltage corresponding to the minimum conductivity. From the data, we calculate the carrier mean free path, $l_{\rm mfp}$ (Fig. 3.22(b)), for particular values of the gate-induced carrier density $n = -2.0 \times 10^{16}$ m^{-2} and $n = -1.0 \times 10^{16}$ m^{-2}, and the field effect mobility of hole conduction, $\mu_{\rm FE}^{\rm h}$ (Fig. 3.22(c)). Either $l_{\rm mfp}$ or $\mu_{\rm FE}^{\rm h}$ decreases with increasing the e-beam dose, reflecting larger density of defects.

Figure 3.23 shows the spatial variation of the $I_{\rm D}/I_{\rm G}$ ratio. Here, the horizontal axis indicates the distance x from the left edge of the sample, and the area of 2.3 μm $\leq x \leq$ 8.3 μm is exposed to e-beam of 60 mC/cm^2. We note that the $I_{\rm D}/I_{\rm G}$ ratio steeply changes within the ranges of 1.4 μm $\leq x \leq$ 2.3 μm and 8.3 μm $\leq x \leq$ 9.2 μm (shaded area in Fig. 3.23). Taking into account the spot size of the Raman laser (~ 0.5 μm), we speculate that the influence of the e-beam dose reaches less than 1 μm from the exposed area. This means that to eliminate the influence of e-beam dose on

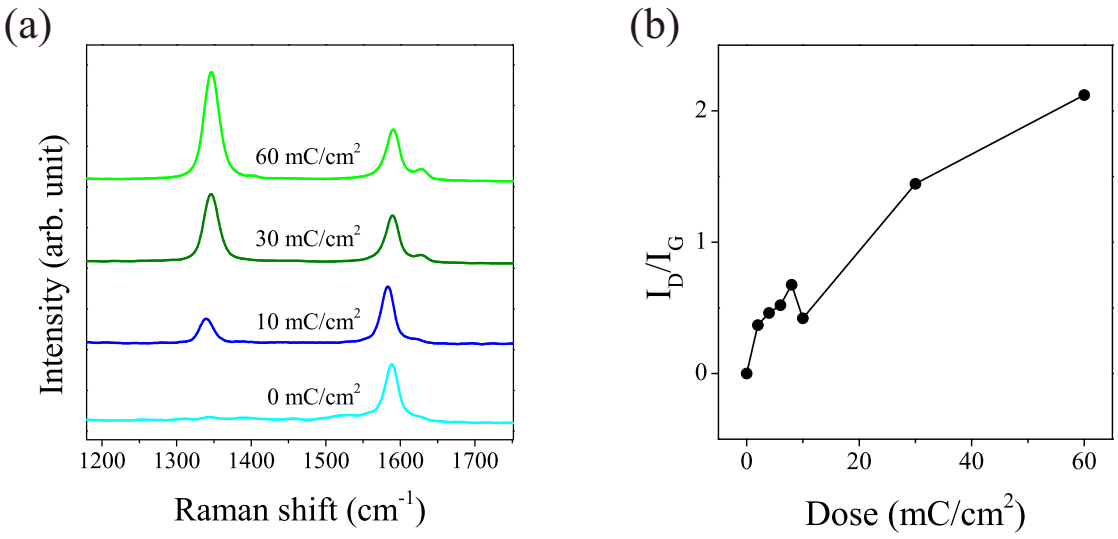

Figure 3.21: (a) Raman spectra of a graphene portion exposed to e-beam. The doses are 60 mC/cm^2, 30 mC/cm^2, 10 mC/cm^2, and 0 mC/cm^2 from the top to the bottom. The curves are shifted vertically for clarity. (b) The $I_{\mathrm{D}}/I_{\mathrm{G}}$ ratio as a function of the e-beam dose.

the electron transport, one needs to separate the current path from the exposed area by more than 1 μm.

3.4 Improvement of the method of inducing local lattice strain

Taking into account the above experimental results, we develop two methods for inducing strain which can eliminate the influence of the e-beam irradiation on the electron transport.

3.4.1 Method 1: introduction of strain by side arms

In the first method, we prepare a graphene device with side arms, and place the resist nanostructures underneath the side arms, which are more than 1 micron apart from the current path. Several side arms are connected to the same area of the current path, as shown in Fig. 3.24. Here, four side arms are stretched and as a result, strain accumulates at the crossing area in the current path.

Procedure of sample fabrication

First, we place a graphene film on a substrate covered with e-beam resist LOR. Then, we fabricate electrodes for transport measurement using e-beam lithography and lift-off. Next, oxygen plasma etching is performed for formation of side arms, and then, the patterns for the resist nanostructures are transferred with excess e-beam exposure of 60 mC/cm^2, as shown in Fig. 3.24.

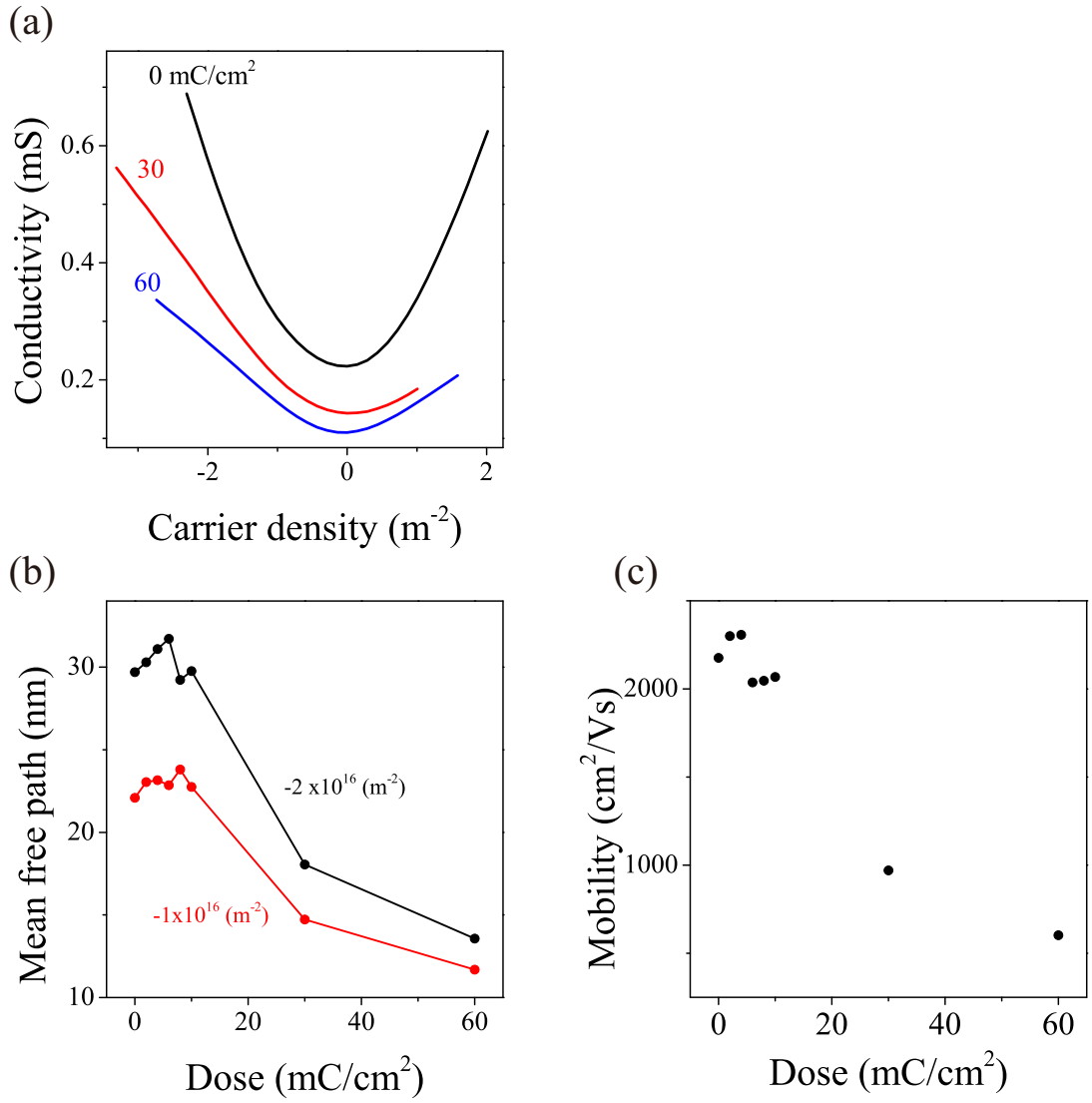

Figure 3.22: (a) Conductivity as a function of the gate-induced carrier density, n, for several values of e-beam dose. (b) E-beam dose dependence of the carrier mean free path, l_{mfp}, for particular values of the gate-induced carrier density $n = -2.0 \times 10^{16}$ m^{-2} and $n = -1.0 \times 10^{16}$ m^{-2}. (c) E-beam dose dependence of the field effect mobility, $\mu_{\mathrm{FE}}^{\mathrm{h}}$.

After the development, the LOR resist without excess e-beam exposure is removed, so that the graphene sheet is attached to the substrate. Figure 3.25(a) shows an SEM image of a sample.

Raman and transport measurements of a graphene device with side arms

Figure 3.25(b) shows the Raman spectra of two areas on graphene indicated in Fig. 3.25(a). The black curve corresponds to the area in the current path close to the side arms, and the red curve

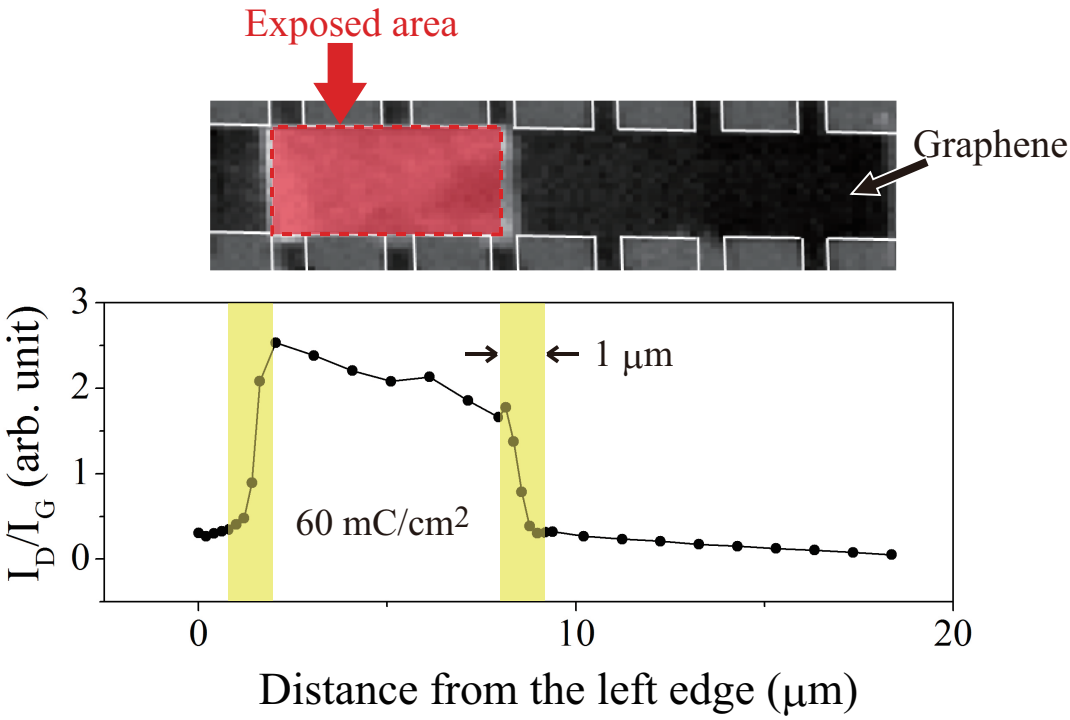

Figure 3.23: Spatial variation of the I_D/I_G ratio.

to the area in the current path which is apart from the side arms. The 2D peak wave number of the former is smaller than that of the latter, indicating that the strain is accumulated to the area close to the side arms. Such trend of 2D band position is also seen in Fig. 3.26, which shows the spatial variation of the 2D band position. These results confirm the controllability of the local strain. Besides, from Fig. 3.26, we find that the spatial variation of strain is ~ 22 cm$^{-1}/\mu m$, which is comparable to that of our previous method (~ 24 cm$^{-1}/\mu m$) (Fig. 3.19).

Figure 3.27 shows the gate voltage dependence of conductivity of this device. The zero conductivity or a flat minimum conductivity is not seen, but the V-shaped curve is clearly deformed. The slope of the $\sigma - V_{\rm g}$ curve in hole conduction regime is -13.5 mS/V, while that in electron conduction regime is 2.8 mS/V, showing that $\mu^{\rm h}_{\rm FE} = 1143$ cm^2/Vs, $\mu^{\rm e}_{\rm FE} = 237$ cm^2/Vs and the mobility ratio $\mu^{\rm e}_{\rm FE}/\mu^{\rm h}_{\rm FE} = 0.21$.

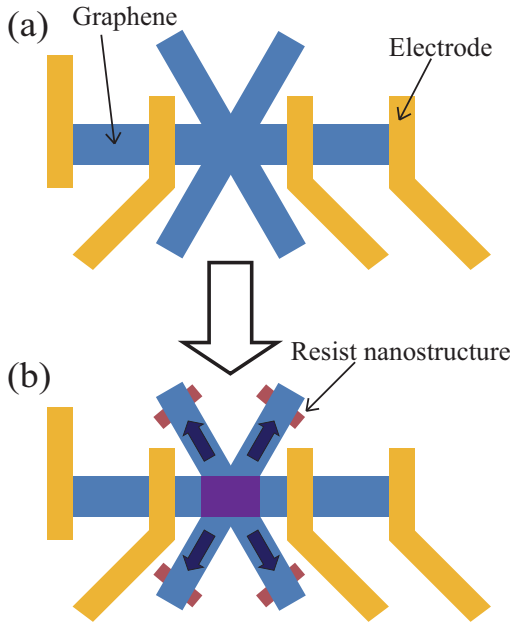

Figure 3.24: Schematics of sample fabrication. A graphene device with side arms is prepared (a), and resist nanostructures are placed underneath the side arms (b).

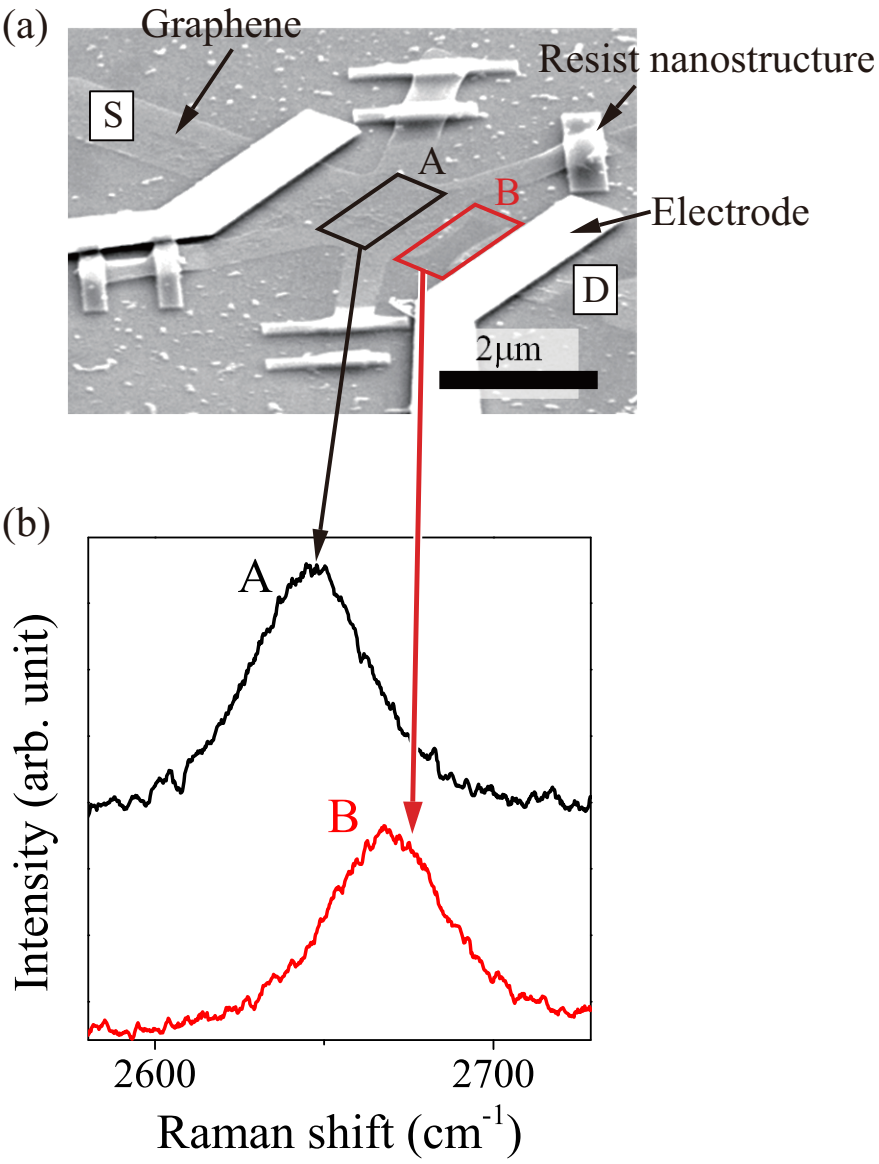

Figure 3.25: (a) SEM image of a graphene sample with side arms. (b) Raman spectra around the 2D band for two areas indicated by black and red squares.

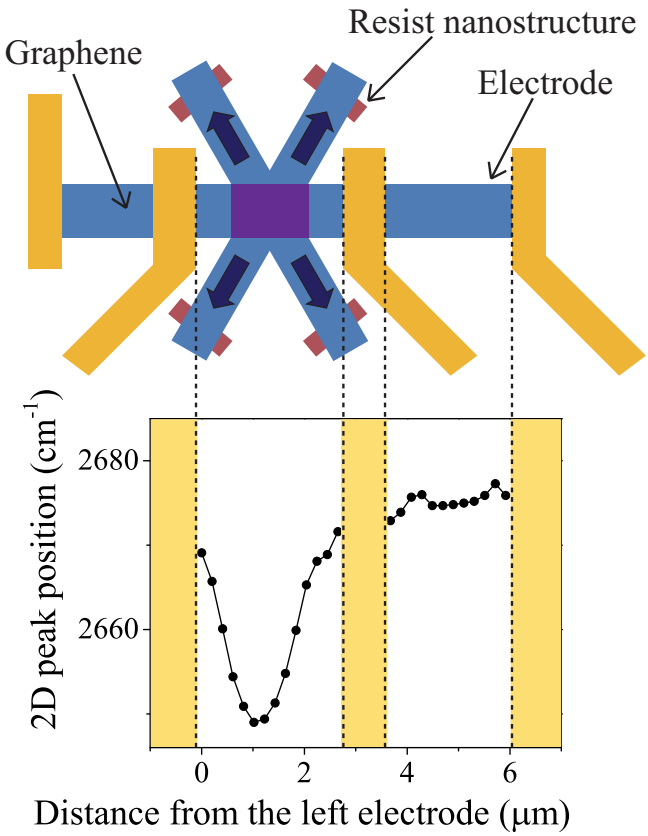

Figure 3.26: The spatial variation of the 2D band position.

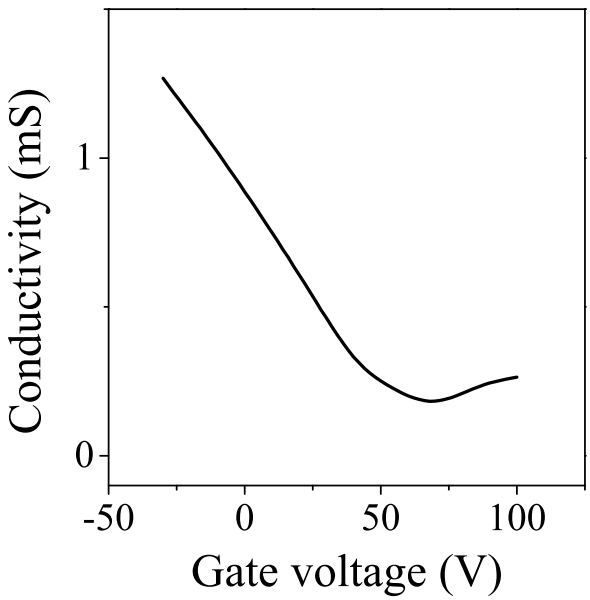

Figure 3.27: Gate voltage dependence of the conductivity of a device with side arms.

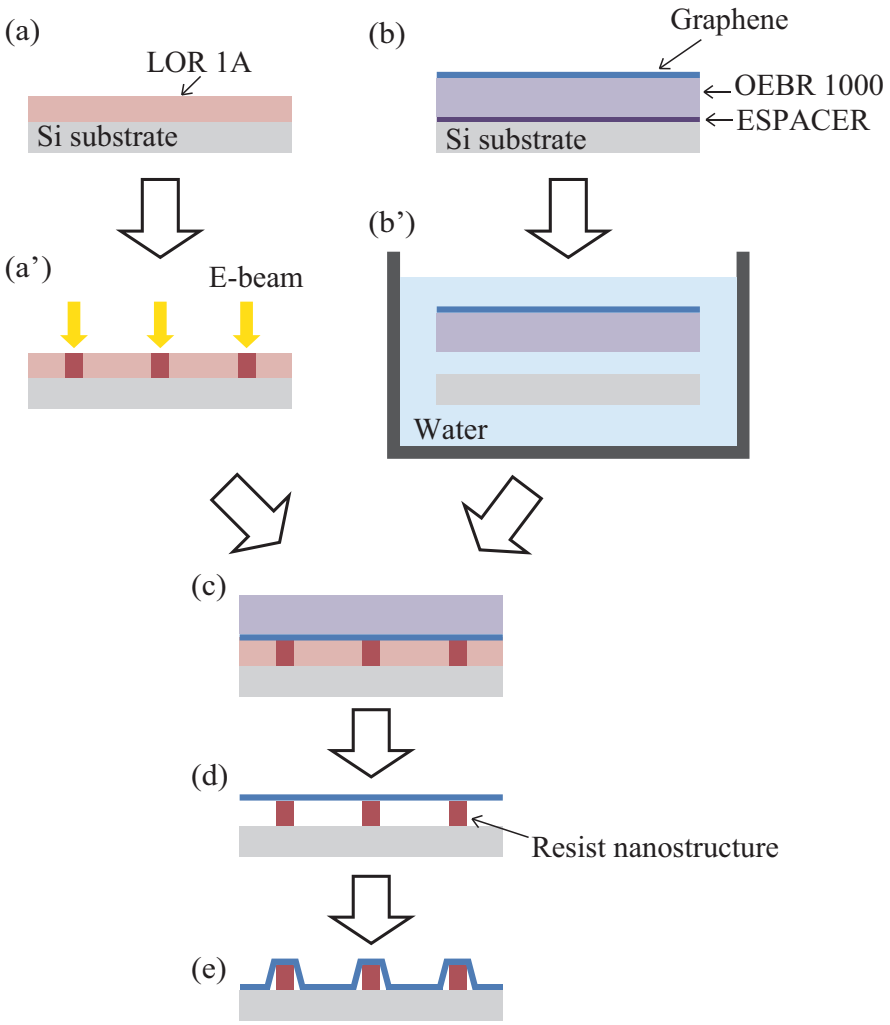

Figure 3.28: Procedure of sample fabrication of method 2.

3.4.2 Method 2: introduction of strain using graphene transfer technique

In the second method for inducing strain in graphene without e-beam damage, we prepare a substrate with resist nanostructures in advance, and then, a graphene film is transferred on it. In this case, graphene is not influenced by the excess e-beam exposure.

Fabrication procedure

First, we spin-coat a Si substrate with the LOR resist, and then expose it to excess e-beam dose for the formation of resist nanostructures (Fig. 3.28(a, a')). We prepare another Si substrate coated with ESPACER (Showa Denko Co.) and OEBR1000 (Tokyo Ohka Co.). ESPACER forms a thin water-soluble layer between the substrate and the OEBR-1000 layer. Graphene is placed on it

using the mechanical exfoliation of kish graphite (Fig. 3.28(b)). When the second substrate with graphene is put into water, the ESPACER layer solves and graphene with supporting OEBR-1000 layer is separated from the Si substrate (Fig. 3.28(b')). This graphene sheet is transferred to the first substrate (Fig. 3.28(c)). During the development, the resist without excess e-beam exposure and the supporting OEBR-1000 layer are removed, so that the graphene is attached to the substrate and strain is introduced to the graphene film (Fig. 3.28(d,e)). Figure 3.29(b) is an SEM image of the sample.

Raman and transport measurements

Raman spectra of the sample is shown in Figs. 3.29(b) and 3.30. Figure 3.29(b) shows the Raman 2D band of two areas on graphene, one close to a resist nanostructure (red curve, B) and the other at the midpoint of adjacent resist nanostructures (black curve, A). Figure 3.30 shows the spatial variation of the Raman 2D band position. The maximum spatial variation of the 2D band position is 8 $\mathrm{cm}^{-1}/\mu\mathrm{m}$, which is about three times smaller than that of our previous method (about 24 $\mathrm{cm}^{-1}/\mu\mathrm{m}$).

Figure 3.31 shows the conductivity as a function of the gate voltage. The $\sigma - V_{\mathrm{g}}$ curve exhibits symmetric V-shaped characteristic ($\mu_{\mathrm{FE}}^{\mathrm{h}} = 140\ \mathrm{cm}^2/\mathrm{Vs}$, $\mu_{\mathrm{FE}}^{\mathrm{e}} = 142\ \mathrm{cm}^2/\mathrm{Vs}$ and the mobility ratio $\mu_{\mathrm{FE}}^{\mathrm{e}}/\mu_{\mathrm{FE}}^{\mathrm{h}} = 1.01$), which is common to unstrained graphene placed on silicon dioxide. Thus, the effect of strain is not clear. We believe that this is because the spatial variation of strain is too small.

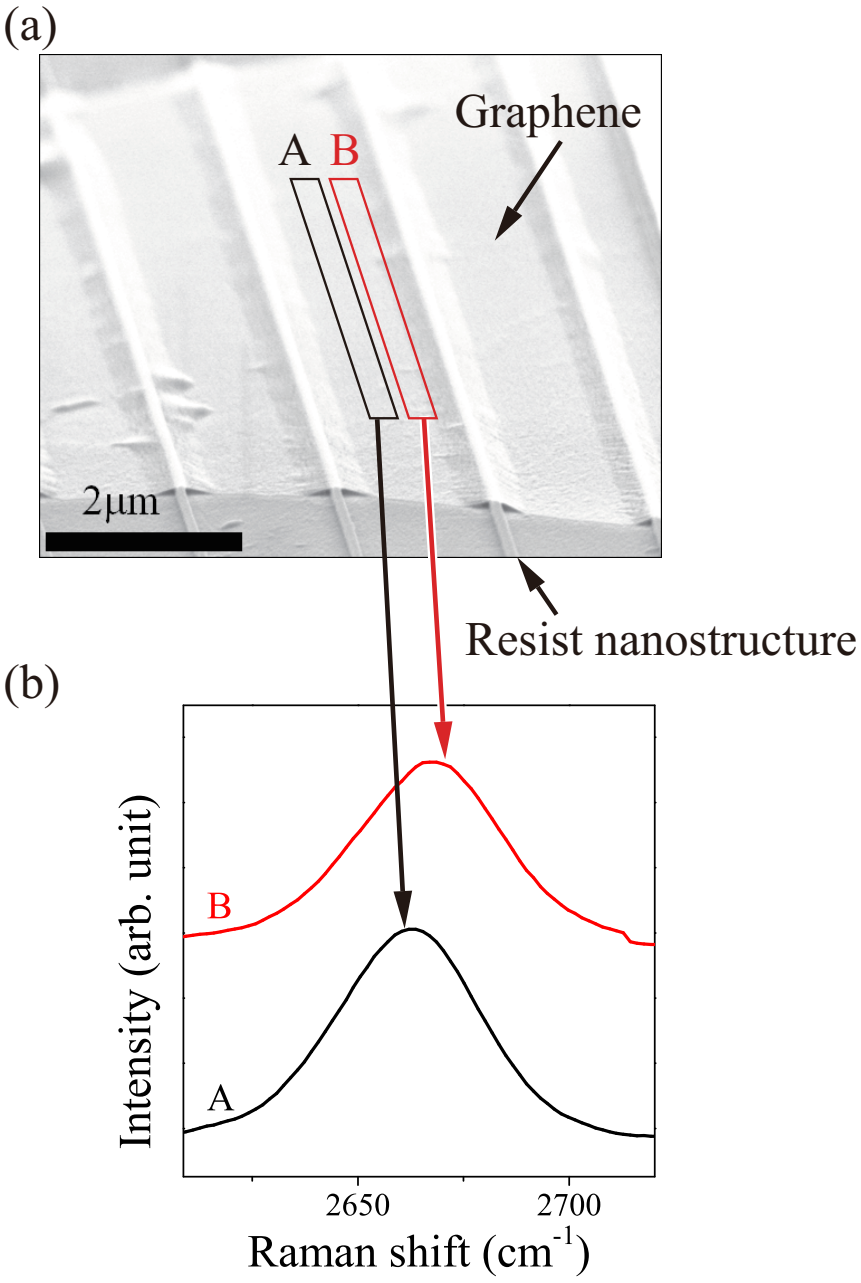

Figure 3.29: Raman spectra (b) for two areas indicated in an SEM image of the sample (a).

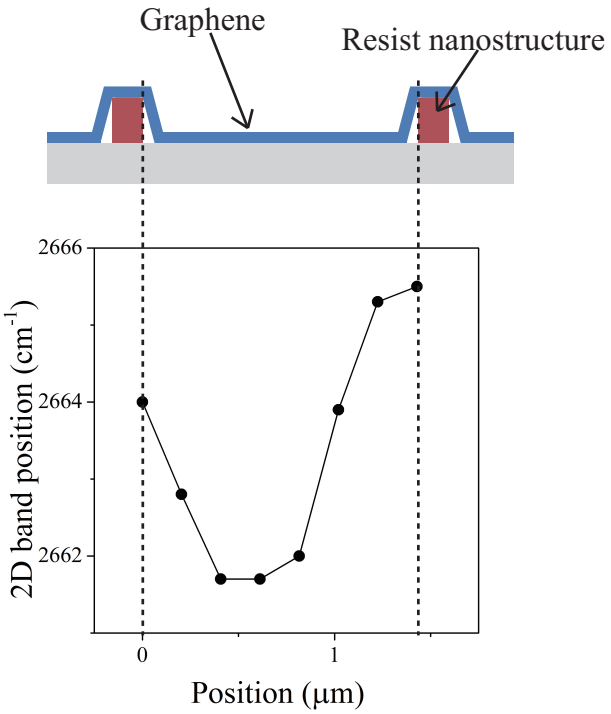

Figure 3.30: The spatial variation of the 2D band position.

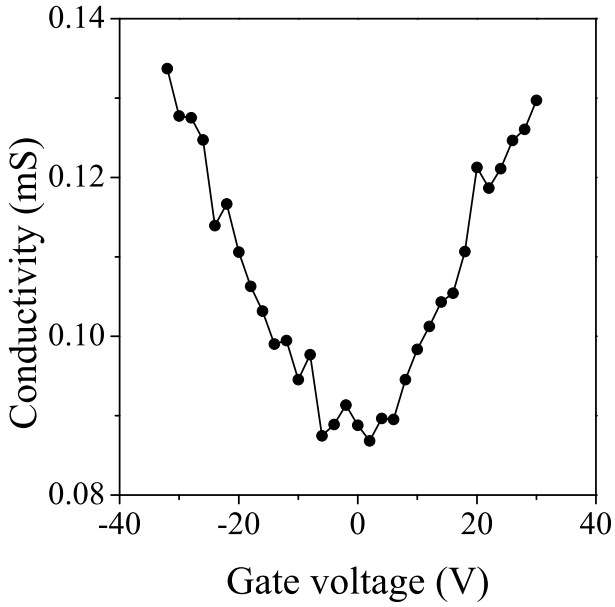

Figure 3.31: Gate voltage dependence of conductivity.

3.5 Summary

Due to the Dirac fermionic properties of electrons in graphene, strain in graphene lattice produces a gauge field. By tailoring the gauge field produced by lattice strain, one can control electronic and transport properties of graphene. In particular, theories tell that by connecting unstrained and strained graphene (one-dimensional local strain), one can induce a transport gap, which is quite important for the application of graphene to electronic devices. In this study, we focused on the one-dimensional local strain. We developed methods to induce local lattice strain in graphene in a controlled manner, and examined electron transport in graphene with one-dimensional local strain.

- To induce designed lattice strain in graphene, we developed a method to insert nanostructures made of dielectric material (electron beam resist) between a graphene film and the Si substrate. The resist nanostructures were made by excess e-beam exposure of 60 $\mathrm{mC/cm^2}$. Controllability of strain was confirmed by the 2D band shift in Raman spectra.

- We used a bar-shaped resist nanostructure (nanorod) to induce one-dimensional local strain in graphene. In graphene FETs with a resist nanorod, the conductivity (σ) − gate voltage (V_g) curve became asymmetric; the field effect mobility of electrons was largely suppressed. This was quite different from the $\sigma - V_\mathrm{g}$ curve of a conventional graphene FET placed on a $\mathrm{SiO_2/Si}$ substrate. To investigate the origin of the distorted $\sigma - V_\mathrm{g}$ curve, we performed the following three experiments:

  1. We compared electron transport in a graphene portion with a resist nanorod and that in a graphene portion without a resist nanorod in a single graphene film, before and after the formation of resist nanorods. The numerical results which took into account the spatial variation of the gate capacitance were not able to explain the experimental observation.
  2. We compared electron transport in a graphene portion with excess e-beam exposure and that in a graphene portion without excess e-beam exposure in a single graphene film. We found that the gate voltage corresponding to the minimum conductivity was not sensitive to the e-beam exposure, indicating that the excess e-beam exposure was not the origin of the distorted $\sigma - V_\mathrm{g}$ curve.
  3. We compared electron transport in two graphene devices with similar resist nanorods but with different spatial distribution of strain. The result indicated that the $\sigma - V_\mathrm{g}$ curve was more distorted in graphene with larger spatial variation of strain.

  These results strongly suggested that the origin of the distorted $\sigma - V_\mathrm{g}$ curve was the local lattice strain. The absence of the theoretically predicted transport gap was attributed to small spatial variation of strain within the electron mean free path.

- We examined the influence of the excess e-beam exposure on the mean free path. We found that the mean free path was strongly degraded by the e-beam of 60 $\mathrm{mC/cm^2}$, and the influence of the e-beam dose reached less than 1 micron from the exposed area.

- To increase the mean free path of a locally strained graphene film, we developed two methods of inducing local strain in graphene.

    1. In the first method, resist nanostructures were placed at arms of graphene sheet, which were apart from the current path by more than 1 μm. The obtained spatial variation of strain was comparable to that of our previous method. In transport measurement, a clear distortion of the $\sigma - V_{\mathrm{g}}$ curve was observed.
    2. In the second method, graphene sheet was transferred on the resist nanorods which were fabricated in advance. The observed spatial variation of strain was three times smaller than that of our previous method. The $\sigma - V_{\mathrm{g}}$ curve exhibited symmetric V-shaped characteristic, which was common to unstrained graphene placed on silicon dioxide.

Reference

[1] H. Tomori, A. Kanda, H. Goto, Y. Ootuka, K. Tsukagoshi, S. Moriyama, E. Watanabe, D. Tsuya, Introducing Nonuniform Strain to Graphene Using Dielectric Nanopillars, Appl. Phys. Express, 4, 075102 (2011)

[2] A. C. Ferrari, J. C. Meyer, V. Scardaci, C. Casiraghi, M. Lazzeri, F. Mauri, S. Piscanec, D. Jiang, K. S. Novoselov, S. Roth, and A. K. Geim, Raman Spectrum of Graphene and Graphene Layers, Phys. Rev. Lett., 97, 187401 (2006)

[3] D. Graf, F. Molitor, K. Ensslin, C. Stampfer, A. Jungen, C. Hierold, and L. Wirtz, Spatially Resolved Raman Spectroscopy of Single- and Few-Layer Graphene, Nano Lett., 7, 238 (2007)

[4] Z. H. Ni, T. Yu, Y. H. Lu, Y. Y. Wang, Y. P. Feng, and Z. X. Shen, Uniaxial Strain on Graphene: Raman Spectroscopy Study and Band-Gap Opening, ACS Nano 2 2301 (2008)

[5] T. M. G. Mohiuddin, A. Lombardo, R. R. Nair, A. Bonetti, G. Savini, R. Jalil, N. Bonini, D. M. Basko, C. Galiotis, N. Marzari, K. S. Novoselov, A. K. Geim, and A. C. Ferrari, Uniaxial strain in graphene by Raman spectroscopy: G peak splitting, Gruneisen parameters, and sample orientation, Phys. Rev. B 79, 205433 (2009)

[6] Vitor M. Pereira and A. H. Castro Neto, Strain Engineering of Graphene's Electronic Structure, Phys. Rev. Lett., 103, 046801 (2009)

[7] H. Karube, H. Tomori, A. Kanda, unpublished.

Chapter 4

Effect of electron beam irradiation on Raman spectra and transport properties of graphene

As exemplified in the previous chapter, irradiation of beams such as electrons, ions (He, Ga, and so on), plasmas strongly influences transport properties of graphene, while it is indispensable for graphene device fabrication. For understanding the physics of beam irradiation and producing electronic devices effectively, it is preferable to evaluate the influence of beam irradiation systematically and nondestructively. Here, we use Raman spectroscopy for the evaluation of the effect of e-beam irradiation. We relate Raman spectra of e-beam irradiated graphene to its transport properties.

4.1 Sample and measurement

Our graphene sample was fabricated by micromechanical exfoliation of kish graphite onto a highly-doped Si substrate covered with 300-nm SiO_2. A four-terminal field effect device was defined using electron beam lithography followed by oxygen plasma etching. A schematic of an typical sample structure is shown in Fig. 4.1.

The device was exposed to electron beam of 50 kV several times. After each exposure, Raman and transport measurements were carried out. The Si substrate was used as a back gate. The e-beam dosage varied from 0 to 64 mC/cm^2. From the Raman spectra, we calculated the intensity ratio of the D band to the G band. From the conductivity, we derived the mobility and electron mean free path as a function of the gate-induced carrier density, n.

In experiment, we repeated the electron beam exposure, Raman mapping and transport measurement in this order. The experimental conditions are described below:

1. E-beam exposure: Accelerating voltage was 50 kV. Total dose varied from 0 to 64 mC/cm^2.
2. Raman mapping: Laser wavelength was 532 nm, laser power was 0.1 mW, and the spot size was about 0.5 μm.

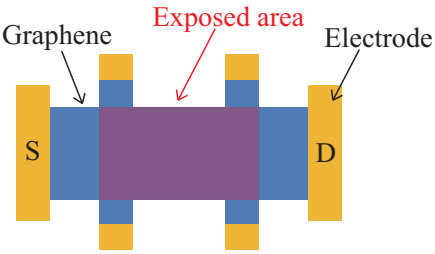

Figure 4.1: Schematic of sample

3. Transport measurement: Four-terminal measurement was performed at room temperature in the air. The highly doped Si substrate was used as a back gate.

Here, Raman mapping and transport measurement were done within one hour after the corresponding e-beam exposure.

4.2 Results and discussion

4.2.1 Electron-beam dose dependence

Figure 4.2(a) shows Raman spectra for several values of e-beam dose. With the increase of e-beam dose, the Raman D band situated ~ 1350 cm^{-1} develops, and the $I_{\mathrm{D}}/I_{\mathrm{G}}$ ratio increases, as shown in the Fig. 4.2(b), indicating that this evolution corresponds to the stage 1 of the amorphization trajectory, in which the crystalline graphene evolves into nanocrystalline graphene.

Figure 4.3(a) shows the gate-voltage dependence of conductivity for several e-beam doses, in which the V-shaped curve shifts to the left and the slope becomes smaller as the dose increases. Here we note that the right part of the V-shaped curve exhibits saturation. Although its origin is not clear at this moment, this kind of asymmetry is sometimes observed in graphene devices. So, hereafter we focus on the left part of the V-shaped curve with hole conduction.

Figure 4.4 shows the e-beam dose dependence of the gate voltage, V_{D}, corresponding to the minimum conductivity, in which V_{D} strongly depends on the e-beam dose. The result is quite different from the result shown in Fig. 3.15, in which V_{D} of an exposed area is almost the same as that of an unexposed area in a single graphene film. It is known that the conductivity and V_{D} strongly depends on molecule adsorption, and is changed by the vacuum pumping and annealing. Conductivity of a graphene FET device is changed even by an adsorption of a single molecule.[1] Here, we attribute the considerable change in V_{D} to the vacuum pumping in a chamber of e-beam lithography machine, and the heating by the Raman laser irradiation.

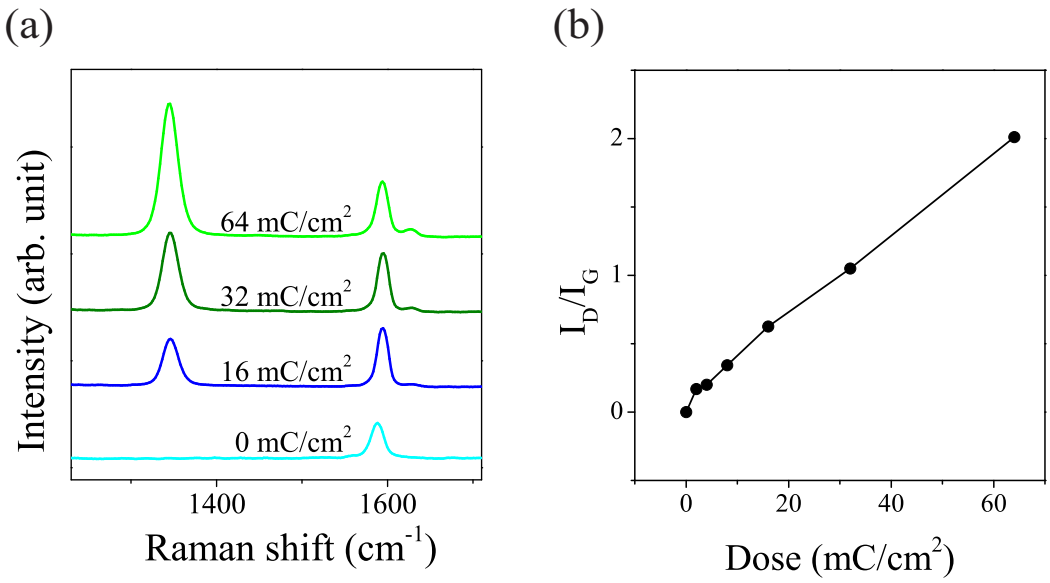

Figure 4.2: (a) Raman spectra for several values of e-beam dose. (b) E-beam dose dependence of the $I_{\mathrm{D}}/I_{\mathrm{G}}$ ratio.

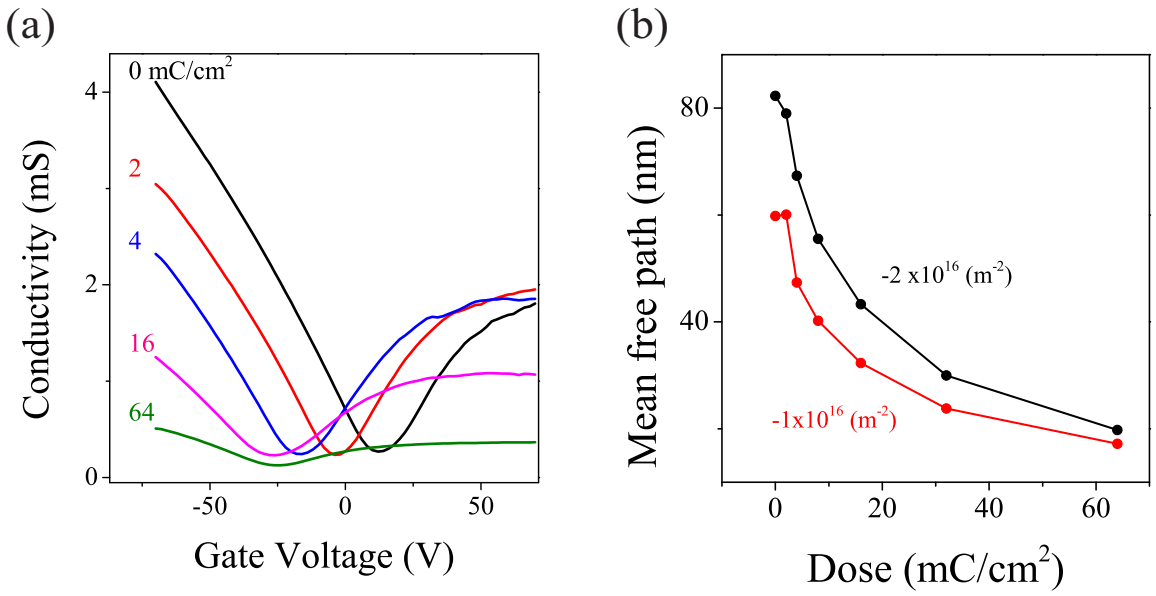

Figure 4.3: (a) Gate-voltage dependence of conductivity for several e-beam doses. (b) E-beam dose dependence of the carrier mean free path.

From the conductivity, we calculate the mean free path using the expression,

$$l_{\mathrm{mfp}} = \frac{h}{2e}\frac{\sigma}{\sqrt{n\pi}},$$

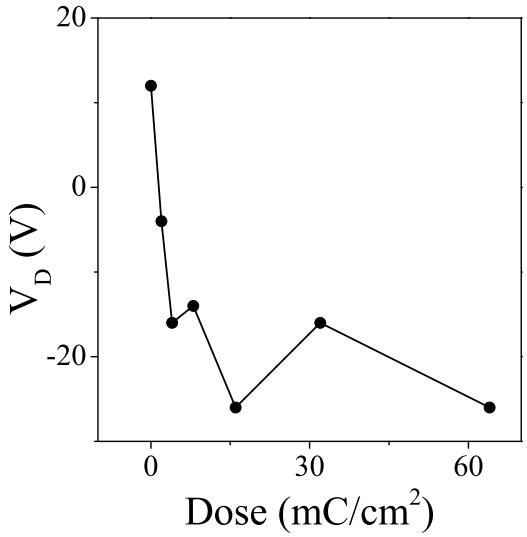

Figure 4.4: E-beam dose dependence of the gate voltage, $V_{\rm D}$, corresponding to the minimum conductivity .

where σ is conductivity and n is the total carrier density. In the following discussion, the gate-induced carrier density is regarded as the total carrier density. The gate-induced carrier density is defined as $n = C_{\rm g}(V_{\rm g} - V_{\rm D})/e$, where $C_{\rm g}$ is the gate capacitance per unit area, $V_{\rm g}$ is the gate voltage, and $V_{\rm D}$ is the gate voltage corresponding to the minimum conductivity. This approximation is valid only for large $|V_{\rm g} - V_{\rm D}|$, where the number of carriers induced, e.g., by charged impurities is negligible in comparison with the number of the gate-induced carriers. Figure 4.3(b) shows the change of the mean free path as a function of the e-beam dose for two values of hole carrier density, $n = -2 \times 10^{16}$ m^{-2} and $n = -1\times 10^{16}$ m^{-2}.[1]

From these results, we obtain a relationship between the $I_{\rm D}/I_{\rm G}$ ratio and the mean free path. Figure 4.5(a) shows $I_{\rm D}/I_{\rm G}$ as a function of the mean free path in a liner plot for two n values, $n = -2 \times 10^{16}$ m^{-2} and -1×10^{16} m^{-2}.[2] The $I_{\rm D}/I_{\rm G}$ ratio decreases with increasing the mean free path. When we plot this result on a log-log scale, we notice that the data points are on a single straight line for each n value, and the slope is -1.84 for $n = -2 \times 10^{16}$ m^{-2} and -2.09 for $n = -1\times 10^{16}$ m^{-2}. Similar results are obtained for other n values, and the slope is about -2. This indicates that the $I_{\rm D}/I_{\rm G}$ ratio is inversely proportional to the square of the mean free path. Thus, the relationship between the $I_{\rm D}/I_{\rm G}$ and the mean free path is given by

$$\frac{I_D}{I_G} = \frac{f(n)}{l_{\rm mfp}^2}$$

[1] In this thesis, a negative (positive) value of the carrier density means that the carrier type is hole (electron).

[2] In the following discussion, we assume that the $I_{\rm D}/I_{\rm G}$ ratio does not depend on the gate voltage. The detailed discussion on the gate voltage dependence of $I_{\rm D}/I_{\rm G}$ will be given later in this chapter.

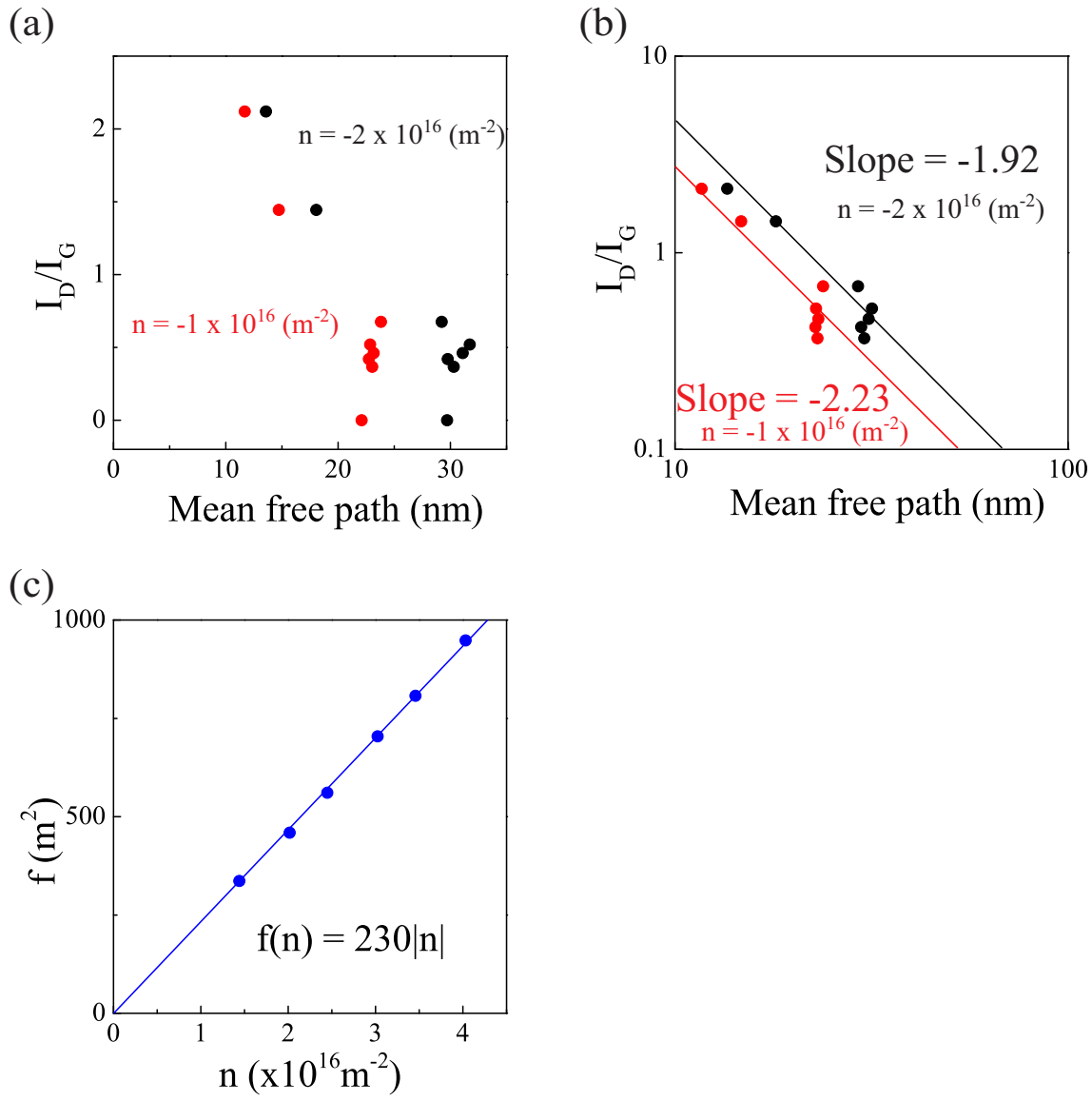

Figure 4.5: (a) The $I_{\mathrm{D}}/I_{\mathrm{G}}$ ratio as a function of the mean free path in a liner plot, for carrier (hole) densities, $n = -2 \times 10^{16}$ m^{-2} and $n = -1 \times 10^{16}$ m^{-2}. (b) The same result but in a log-log plot. The lines indicate a slope of -2. (c) The carrier density dependence of the proportionality constant $f(n)$.

where $f(n)$ is a proportionality constant.

Figure 4.5(c) shows the carrier density dependence of the proportionality constant $f(n)$, in which $f(n)$ is proportional to the carrier density: $f[\mathrm{m}^2] = 230n[\times 10^{16}\ \mathrm{m}^{-2}]$. By using this result,

the relationship between $I_{\rm D}/I_{\rm G}$ and the mean free path is given by

$$\frac{I_D}{I_G} = (1.2 \times 10^{-8}[\mathrm{m}])^4 \frac{|n|}{l_{\rm mfp}^2}.$$

Figure 4.6 shows the experimental results for another sample. Again for this sample, the $I_{\rm D}/I_{\rm G}$ ratio decreases with increasing the mean free path, as shown in Fig. 4.7(a). In a log-log plot (Fig. 4.7(b)), the data points are on a single straight line for each n value, and the slope is -1.92 for $n = -2\times10^{16}$ m^{-2} and -2.23 for $n = -1\times 10^{16}$ m^{-2}. Similar results are obtained for other n values, and the slope is about -2. Thus, again for this sample, the $I_{\rm D}/I_{\rm G}$ ratio is inversely proportional to the square of the mean free path. The proportionality constant is given by $f[\mathrm{m}^2] = 460n[\times10^{16}$ m$^{-2}]$ (Fig. 4.7(c)), and the following relationship is obtained:

$$\frac{I_D}{I_G} = (1.5 \times 10^{-8}[\mathrm{m}])^4 \frac{|n|}{l_{\rm mfp}^2}.$$

Thus, for two samples, we find that the $I_{\rm D}/I_{\rm G}$ ratio is inversely proportional to the square of the mean free path and the proportionality constant is around (10 nm)^4.

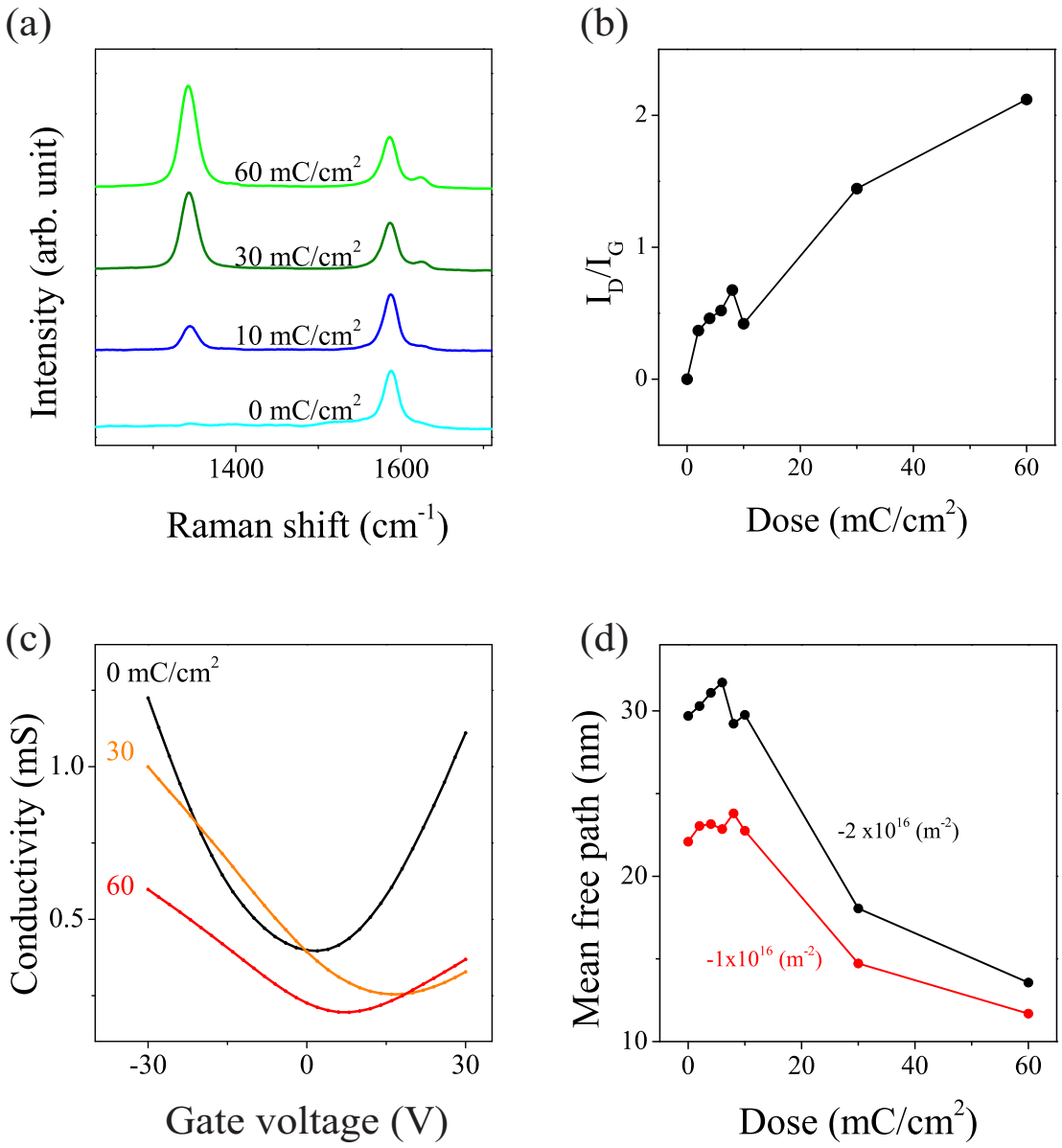

Figure 4.6: Results for another sample. (a) Raman spectra for several values of e-beam dose. (b)E-beam dose dependence of the I_D/I_G ratio. (c) The gate-voltage dependence of conductivity for several e-beam doses. (d) E-beam dose dependence of the carrier mean free path.

4.2.2 Change in I_D/I_G ratio

Next, we discuss the gate voltage dependence of the I_D/I_G ratio. For this purpose, we repeated the micro Raman spectroscopy (mapping) for the whole graphene area successively for a particular e-beam dose. The results are shown in Figs. 4.8 and 4.9 for e-beam dose of 10mC/cm^2 and 20mC/cm^2, respectively, for the same graphene film. In Figs. 4.8(a) and 4.9(a), the I_D/I_G ratio is

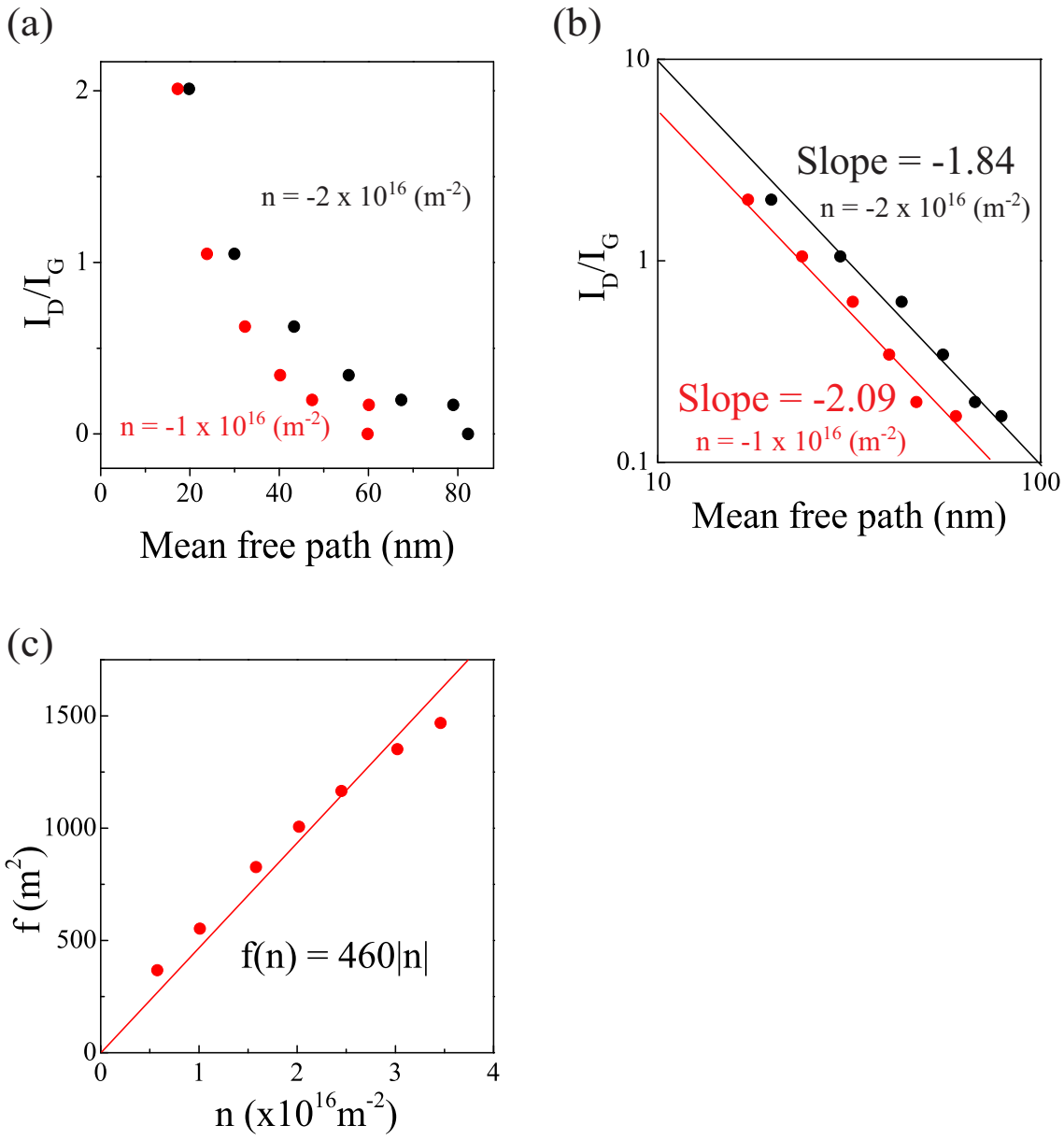

Figure 4.7: (a) The $I_{\mathrm{D}}/I_{\mathrm{G}}$ ratio as a function of the mean free path in a liner plot for carrier densities, $n = -2 \times 10^{16}$ m^{-2} and $n = -1 \times 10^{16}$ m^{-2}. (b) The same data but in a log-log plot. The lines indicate a slope of -2. (c) The carrier density dependence of the proportionality constant $f(n)$.

plotted as a function of the number of the Raman mapping repetition, in which the shaded area indicates the Raman mapping with gate-voltage variation. The gate-voltage dependence of the $I_{\mathrm{D}}/I_{\mathrm{G}}$ ratio taken from the data in the shaded areas in Figs. 4.8(a) and 4.9(a) is shown in Figs.

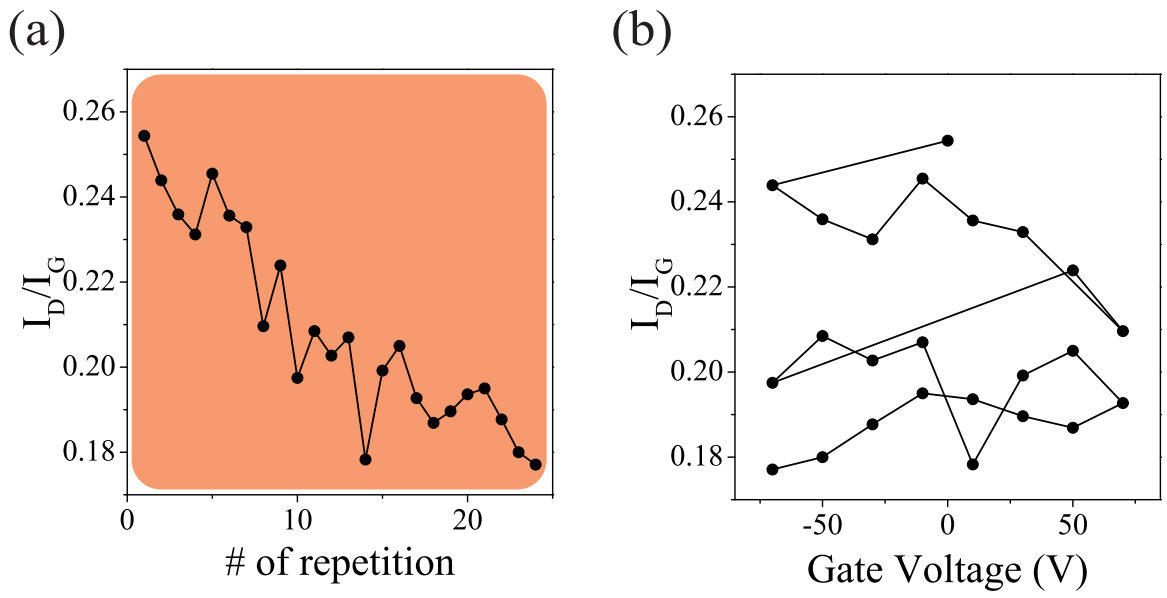

Figure 4.8: (a) The I_D/I_G ratio as a function of the number of Raman mapping repetition for e-beam dose of 10 mC/cm^2. (b) Gate voltage dependence of I_D/I_G for the shaded region in (a).

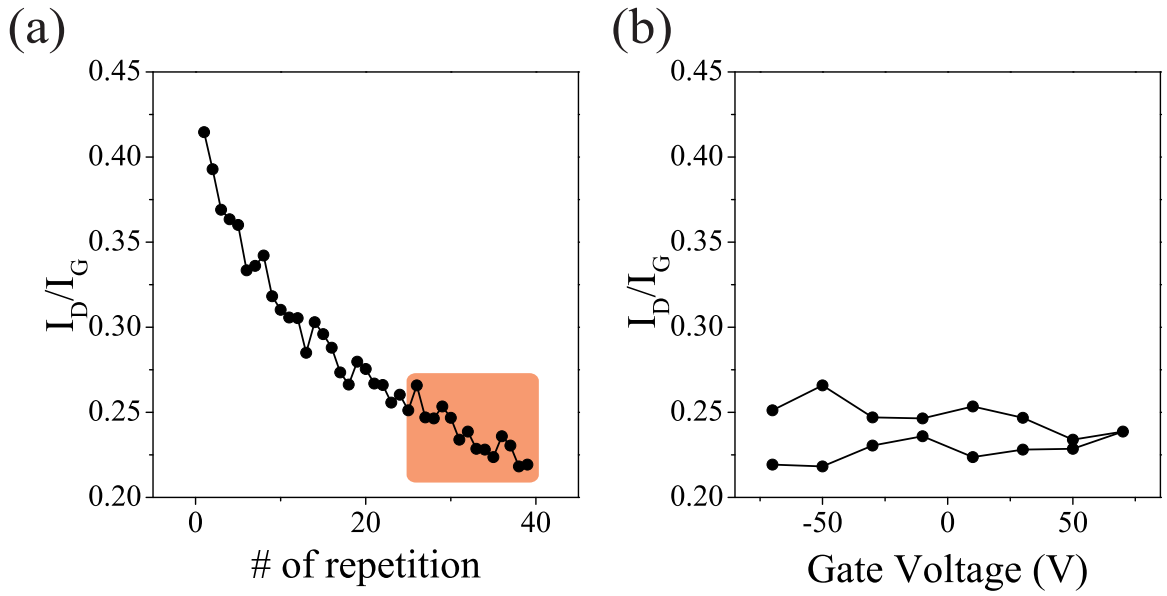

Figure 4.9: (a) The I_D/I_G ratio as a function of the number of Raman mapping repetition for e-beam dose of 20 mC/cm^2. (b) Gate voltage dependence of I_D/I_G for the shaded region in (a).

4.8(b) and 4.9(b), respectively. As shown in Figs. 4.8(a) and 4.9(a), I_D/I_G dramatically decreases

as the Raman mapping is repeated, and systematic variation of $I_{\rm D}/I_{\rm G}$ as a function of the gate voltage is not seen in Figs. 4.8(b) and 4.9(b). (Even if there is a systematic variation of $I_{\rm D}/I_{\rm G}$ as a function of the gate voltage, its magnitude is below the experimental error of 0.02/100 V.) This is the reason why we disregard the gate voltage dependence of the $I_{\rm D}/I_{\rm G}$ ratio in the discussion of section 4.2.1.

The decrease of the $I_{\rm D}/I_{\rm G}$ ratio has not been reported so far. One might think that this indicates restoration of structural defects in graphene with heating by Raman laser. However, one needs to take into account the following experimental facts:

- A structural defect (or, knock-on damage) is reported to appear by e-beam with an energy larger than 144 keV.[2]
- Charged impurities on a graphene surface usually do not contribute to the Raman D band.[3]

We speculate that a special mechanism for the appearance of the D band by e-beam irradiation exists for graphene placed on a SiO_2 layer. The details should be clarified in a future study.

4.3 Summary

We studied the relationship between the Raman $I_{\rm D}/I_{\rm G}$ ratio and the electron mean free path in e-beam irradiated graphene. We found that the $I_{\rm D}/I_{\rm G}$ ratio is inversely proportional to the square of the mean free path and the following expression is satisfied,

$$\frac{I_D}{I_G} = a^4 \frac{|n|}{l_{\rm mfp}^2}.$$

The proportionality constant is $a = 12$ nm and 15 nm for two samples. Also, we found that in e-beam irradiated graphene, the D band intensity decreases by the Raman mapping.

Reference

[1] F. Schedin, A. K. Geim, S. V. Morozov, E. W. Hill, P. Blake, M. I. Katsnelson, and K.S. Novoselov, Detection of Individual Gas Molecules Adsorbed on Graphene, Nat. Mater., **6**, 652–655 (2007)

[2] L. W. Hobbs, in "Quantitative Electron Microscopy", edited by J. N. Chapman, A. J. Craven, Plenum Press, New York, 399 – 445 (1989)

[3] B. Krauss, T. Lohmann, D.-H. Chae, M. Haluska, K. von Klitzing, and J. H. Smet, Laser-induced disassembly of a graphene single crystal into a nanocrystalline network, Phys. Rev. B 79, 165428 (2009)

Chapter 5

Summary

This thesis deals with experimental studies on electron transport in graphene under the influence of local lattice strain and electron beam exposure. We obtained graphene films from the micromechanical exfoliation of kish graphite, and fabricated FET-type devices using electron beam lithography, metal deposition, lift-off, and oxygen plasma etching. Micro Raman spectroscopy was used for identification of graphene and characterization of the defect density as well as local lattice strain. Electron transport measurement was performed at room temperature in vacuum or in the air using a probe station.

Effect of lattice strain

Due to the Dirac fermionic properties of electrons in graphene, strain in graphene lattice produces a gauge field. By tailoring the gauge field produced by lattice strain, one can control electronic and transport properties of graphene. In particular, theories tell that by connecting unstrained and strained graphene (one-dimensional local strain), one can induce a transport gap, which is quite important for the application of graphene to electronic devices. In this study, we focused on the one-dimensional local strain. We developed methods to induce local lattice strain in graphene in a controlled manner, and examined electron transport in graphene with one-dimensional local strain.

- To induce designed lattice strain in graphene, we developed a method to insert nanostructures made of dielectric material (electron beam resist) between a graphene film and the Si substrate. The resist nanostructures were made by excess e-beam exposure of 60 $\mathrm{mC/cm^2}$. Controllability of strain was confirmed by the 2D band shift in Raman spectra.

- We used a bar-shaped resist nanostructure (nanorod) to induce one-dimensional local strain in graphene. In graphene FETs with a resist nanorod, the conductivity (σ) − gate voltage (V_g) curve became asymmetric; the field effect mobility of electrons was largely suppressed. This was quite different from the $\sigma - V_\mathrm{g}$ curve of a conventional graphene FET placed on a SiO_2/Si substrate. To investigate the origin of the distorted $\sigma - V_\mathrm{g}$ curve, we performed the following three experiments:

1. We compared electron transport in a graphene portion with a resist nanorod and that in a graphene portion without a resist nanorod in a single graphene film, before and after the formation of resist nanorods. The numerical results which took into account the spatial variation of the gate capacitance were not able to explain the experimental observation.
2. We compared electron transport in a graphene portion with excess e-beam exposure and that in a graphene portion without excess e-beam exposure in a single graphene film. We found that the gate voltage corresponding to the minimum conductivity was not sensitive to the e-beam exposure, indicating that the excess e-beam exposure was not the origin of the distorted $\sigma - V_{\rm g}$ curve.
3. We compared electron transport in two graphene devices with similar resist nanorods but with different spatial distribution of strain. The result indicated that the $\sigma - V_{\rm g}$ curve was more distorted in graphene with larger spatial variation of strain.

These results strongly suggested that the origin of the distorted $\sigma - V_{\rm g}$ curve was the local lattice strain. The absence of the theoretically predicted transport gap was attributed to small spatial variation of strain within the electron mean free path.

- We examined the influence of the excess e-beam exposure on the mean free path. We found that the mean free path was strongly degraded by the e-beam of 60 mC/cm^2, and the influence of the e-beam dose reached less than 1 micron from the exposed area.

- To increase the mean free path of a locally strained graphene film, we developed two methods of inducing local strain in graphene.

  1. In the first method, resist nanostructures were placed at arms of graphene sheet, which were apart from the current path by more than 1 μm. The obtained spatial variation of strain was comparable to that of our previous method. In transport measurement, a clear distortion of the $\sigma - V_{\rm g}$ curve was observed.
  2. In the second method, graphene sheet was transferred on the resist nanorods which were fabricated in advance. The observed spatial variation of strain was three times smaller than that of our previous method. The $\sigma - V_{\rm g}$ curve exhibited symmetric V-shaped characteristic, which was common to unstrained graphene placed on silicon dioxide.

In the future experiments, we need to improve the design of resist nanostructures to make larger spatial variation of strain within the mean free path, e.g., by using thicker resist and by suspending the graphene sheet.

Effect of e-beam irradiation

Raman spectroscopy is a nondestructive and easy technique to characterize graphene. However, the relationship of Raman spectra with transport-related physical quantities has not been examined yet. Here, we studied the relationship between the Raman $I_{\mathrm{D}}/I_{\mathrm{G}}$ ratio and the electron mean free path in e-beam irradiated graphene. We found that the $I_{\mathrm{D}}/I_{\mathrm{G}}$ is inversely proportional to the square of the mean free path and the following expression is satisfied,

$$\frac{I_D}{I_G} = a^4 \frac{|n|}{l_{\mathrm{mfp}}^2}.$$

The proportionality constant is $a = 12$ nm and 15 nm for two samples. Also, we found that in e-beam irradiated graphene, the D band intensity decreases by the Raman mapping.

Acknowledgment

I would like to express my sincere thank to Professor Y. Ootuka for helping throughout this study and reviewing the manuscripts. I would like to sincerely thank Professor A. Kanda for making long time to have discussions with me, giving much help and reviewing the manuscript of this thesis. I wish to thank Professor M. Hayashi and Professor H. Yoshioka for many informative discussions and warm encouragement. To Professor Y. Hatsugai and Professor S. Nomura I would like to express my deepest thanks for reviewing the manuscripts and giving much helpful advice throughout this study. All the members of Ootuka group and Kanda group are also acknowledged for providing much support and encouragement. Especially, technical help with the operation of the Raman microscope from Dr. D. Tsuya, Dr. E. Watanabe and Dr. S. Moriyama are unforgettable. To Dr. H. Goto I would like to express my deepest thanks for instructing me in the various experimental techniques and giving much helpful advice. To Professor J. Nakamura and Professor T. Kondo I would like to express my thanks for valuable discussions. I would also like to acknowledge the help with the operation of the electron beam lithography system from Dr. Y. Sakurai. Finally, I would like to thank my parents.